

Amylopectin-*graft*-hydrolyzed-poly(methyl acrylate) (AP-*g*-H-PMA)
Flocculants for the Treatment of Oil Sands Tailings

by
Stepheney Davey

A thesis submitted in partial fulfillment of the requirements for the degree of

Master of Science

in

Chemical Engineering

Department of Chemical and Materials Engineering
University of Alberta

© Stepheney Davey, 2020

Abstract

The extraction of bitumen from the Alberta oil sands reserves has long been a major economic contributor to the Canadian society, but the impact this industry has had on the environment has raised concerns worldwide. The main problems are how to reclaim the area and reduce the number of tailings ponds. A major obstacle is how to treat the stable suspensions of fine particles that constitute the mature fine tailings (MFT). Synthetic polymer flocculants commonly used in the industry are limited by their shear degradability and possible environmental impact. Natural polymers are more shear stable and ecofriendly, but they do not perform as well as synthetic polymers.

This thesis explores the flocculation and dewatering performance of a family of natural amylopectin-*graft*-hydrolyzed-poly(methyl acrylate) (AP-g-H-PMA) flocculants on MFT. Free radical graft polymerization was used to chemically graft methyl acrylate chains to amylopectin backbones, followed by alkaline hydrolysis. Several grades of the graft copolymer, with different graft lengths and densities, were produced following a central composite design of experiments and tested on 10 wt.% MFT suspensions. The flocculants were characterized by Fourier-transform infrared spectroscopy (FTIR), nuclear magnetic resonance spectroscopy (^1H and ^{13}C NMR), helium-ion microscopy (HiM), and thermogravimetric analysis (TGA). After hydrolysis, the products were again analyzed by FTIR and field flow fractionation (FFF).

The synthesis parameters influencing graft length, graft density, and flocculant dosage affected the flocculation performance significantly. Generally, AP-g-H-PMA flocculants with longer and fewer grafts led to higher initial settling rates (ISR) and faster capillary suction times (CST), especially at high dosages, but produced supernatants with slightly higher turbidities. When

optimum dosages were used, AP-g-H-PMA outperformed both of its homopolymers (AP and H-PMA), as well as a commercial anionic polyacrylamide (A-PAM).

Preface

The thesis is an original work by Stepheney Davey with some guidance by Behnaz Bazoubandi, Fernanda L. Motta, Vahid Vajihinejad, and João B. P. Soares.

Stepheney Davey was responsible for the experimental testing, data collection and analysis, and manuscript preparation. V. Vajihinejad contributed to the creation of the statistical design of experiments and F. L. Motta provided occasional assistance regarding the statistical analysis. B. Bazoubandi and V. Vajihinejad also gave time to time guidance in some experimental procedures. Professor J. B. P. Soares was the supervisor of this research work. He was involved in revisions of the thesis and provided suggestions and ideas throughout the work.

Acknowledgments

I am incredibly blessed and thankful for the time I have spent at the University of Alberta pursuing this degree. I wish to thank all the people whose assistance, advice, and support, was key in the completion of this project. Firstly, I would like to express my sincere appreciation to my supervisor, Professor João B. P. Soares, who guided and encouraged me throughout my work. I am truly thankful for his expert knowledge, kindness, and unwavering support, at every stage of this project. Furthermore, I would like to thank all the members of our research group for fostering a friendly, helpful, and safe work environment.

Regarding my project, I would like to thank and recognize Dr. Marco da Silva for his help with the molecular weight measurements and Shiraz Merali for his help with the atomic absorption spectrophotometry. As well, I appreciate the help from staff at the nanoFAB Fabrication and Characterization Centre and the Nuclear Magnetic Resonance Facility in the Department of Chemistry for their help in some of the characterization tests. I also wish to thank the Institute for Oil Sands Innovation (IOSI) and COSIA labs for the use of their equipment, and particularly Lisa Brandt and Brittany Mackinnon for their help and time providing equipment training. I further gratefully acknowledge the financial support received from the Natural Sciences and Engineering Research Council of Canada (NSERC).

Finally, I wish to thank all my friends and family, especially those closest to me, including my parents, my sister Kathyne, and Ben. Thank you for your encouragement, patience, and love.

Table of Contents

1. Introduction.....	1
2. Background and Literature Review	3
2.1 Oil Sands and Oil Production in Alberta.....	3
2.1.1 Alberta’s Oil Sands Reserves.....	3
2.1.2 Oil Sands Composition and the Bitumen Extraction Process.....	4
2.1.3 Bitumen Upgrading and Refining.....	6
2.1.4 Water Usage.....	7
2.2 The Tailings Problem and Management Techniques.....	8
2.2.1 Tailings Ponds.....	8
2.2.2 General Treatment Technologies.....	9
2.2.3 Composite/Consolidated Tailings.....	10
2.2.4 Paste Technology/Thickened Tailings.....	10
2.3 The Colloidal Nature of Mature Fine Tailings.....	11
2.3.1 Stability of Mature Fine Tailings.....	11
2.3.2 Flocculation and Coagulation.....	16
2.3.3 Flocculation Mechanisms	17
2.4 Synthetic, Natural, and Graft Copolymer Flocculants	22
2.4.1 Synthetic and Natural Polymers.....	22
2.4.2 Natural Graft Copolymers.....	23
2.5 Amylopectin Based Copolymers.....	25
2.5.1 Starch, Amylose, and Amylopectin	25
2.5.2 Amylopectin Graft Copolymers.....	27
3. Materials and Methods.....	33
3.1 Materials.....	33
3.2 Production of Amylopectin Graft Copolymer Flocculants	33
3.2.1 Synthesis of Amylopectin- <i>graft</i> -poly(methyl acrylate) (AP- <i>g</i> -PMA).....	33
3.2.2 AP- <i>g</i> -PMA Purification	34
3.2.3 Grafting Parameters	35
3.2.4 Alkaline Hydrolysis (AP- <i>g</i> -H-PMA).....	36
3.2.5 Central Composite Design of Experiments.....	39
3.3 Proof of Grafting and Flocculant Characterization	42

3.3.1	Fourier-Transform Infrared Spectroscopy (FTIR).....	42
3.3.2	Nuclear Magnetic Resonance Spectroscopy (NMR).....	43
3.3.3	Helium-ion Microscopy (HiM).....	43
3.3.4	Thermogravimetric Analysis (TGA).....	44
3.3.5	Field Flow Fractionation (FFF)	45
3.4	MFT Characterization	45
3.4.1	Dean-Stark Extraction.....	45
3.4.2	Solids and Moisture Analysis	46
3.4.3	Particle Size Distribution (PSD).....	46
3.4.4	Atomic Absorption Spectrophotometry (AAS)	46
3.5	MFT Flocculation and Dewatering Tests.....	47
3.5.1	Benchtop Mixing	47
3.5.2	Capillary Suction Time (CST).....	48
3.5.3	Initial Settling Rate (ISR)	49
3.5.4	Supernatant Turbidity	50
3.5.5	Solids Content.....	51
3.6	Comparison Testing	52
3.6.1	Benchtop Flocculation Comparison Tests	52
4.	Results and Discussion	53
4.1	Synthesis of Amylopectin Grafted with Poly(methyl acrylate) (AP-g-PMA).....	53
4.1.1	Proposed Graft Copolymerization Mechanism.....	53
4.1.2	Synthesis Results	54
4.1.3	Effects on Monomer Conversion	55
4.1.4	Effects on Grafting Efficiency and Homopolymer Formation	56
4.1.5	Effects on Grafting Ratio	58
4.2	Hydrolysis Discussion.....	59
4.3	Proof of Grafting and Flocculant Characterization	60
4.3.1	FTIR Analysis.....	60
4.3.2	¹ H NMR Analysis	64
4.3.3	¹³ C NMR Analysis	69
4.3.4	HiM Morphological Analysis	73
4.3.5	Thermal Analysis	76
4.3.6	Molecular Weight Analysis	79
4.4	MFT Characterization	80

4.4.1	Dean-Stark Extraction Analysis.....	80
4.4.2	Solids and Moisture Analysis	80
4.4.3	PSD Analysis	81
4.4.4	AAS Analysis.....	81
4.5	Effect of Graft Length, Graft Density, and Flocculant Dosage on MFT Flocculation ..	82
4.5.1	CCD Flocculation and Dewatering Results	82
4.5.2	Initial Settling Rate (ISR)	84
4.5.3	Initial CST.....	87
4.5.4	Sediment CST	90
4.5.5	Supernatant Turbidity	93
4.5.6	Solids Content.....	96
4.6	Comparison Testing	96
4.6.1	Benchtop Flocculation Comparison Tests	96
5.	Conclusions and Future Work	102
	References.....	104
	Appendix A. Purification Study.....	114
	Appendix B. CCD ANOVA and Residual Plots	117
	Appendix C. Comparison Flocculation Results	122

List of Tables

Table 2.1: Summary of published amylopectin graft copolymers used as flocculants.....	31
Table 3.1: Central composite design (CCD) independent variables and their level values.....	40
Table 3.2: Summary of the 3-factor central composite design (CCD).	41
Table 3.3: FTIR analysis summary.	43
Table 3.4: NMR analysis summary.	43
Table 3.5: HiM analysis summary.	44
Table 3.6: TGA analysis summary.	45
Table 4.1: Proposed graft copolymerization reaction scheme.	53
Table 4.2: Grafting parameter results for the amylopectin- <i>graft</i> -poly(methyl acrylate) (AP- <i>g</i> -PMA) grades.	55
Table 4.3: Amylopectin (AP) FTIR absorption peaks and corresponding functional groups.	62
Table 4.4: Poly(methyl acrylate) (PMA) FTIR absorption peaks and corresponding functional groups.....	62
Table 4.5: FFF molecular weight results.	79
Table 4.6: Dean-Stark extraction MFT composition.	80
Table 4.7: Solids and moisture analyses.	80
Table 4.8: Mean PSD volume and number sizes.	81
Table 4.9: Major ion concentrations in an undiluted MFT sample.....	82
Table 4.10: Summary of the CCD flocculation and dewatering results.	83
Table 4.11: Overview of the significant factors for each response.....	84
Table 4.12: ISR model equation.	85
Table 4.13: Initial CST model equation.....	88
Table 4.14: Sediment CST model equation.	91
Table 4.15: Turbidity model equation.	94
Table A1: Percentage of total poly(methyl acrylate) (PMA) homopolymer washed away over time.	115
Table B1: ANOVA for the ISR model.	117
Table B2: ANOVA for the initial CST model.....	118
Table B3: ANOVA for the sediment CST model.....	119

Table B4: ANOVA for the turbidity model.....	120
Table B5: ANOVA for the solids content model.....	121
Table C1: Flocculation results for the comparison tests.....	122

List of Figures

Figure 2.1: Alberta’s oil sands areas (redrawn from [4]).....	3
Figure 2.2: In-situ and surface mining bitumen extraction (redrawn from [11]).....	4
Figure 2.3: Bitumen pathways to market (redrawn from [15]).....	7
Figure 2.4: Oil sands tailings pond diagram (redrawn from [26]).....	9
Figure 2.5: Attractive and repulsive interactions between particles (redrawn from [37]).....	12
Figure 2.6: Keesom forces (A), Debye forces (B), and London dispersion forces (C) (redrawn from [41]).....	13
Figure 2.7: Electric double layer diagram (redrawn from [37]).	14
Figure 2.8: DLVO interaction curve (redrawn from [37], [43]).	15
Figure 2.9: Particle aggregation by coagulation followed by flocculation.	17
Figure 2.10: Segment conformations of an adsorbed polymer on a particle surface (redrawn from [36], [39]).....	18
Figure 2.11: Adsorption and polymer bridging of negatively charged particles with a neutral polymer (redrawn from [51], [57]).	19
Figure 2.12: Adsorption and charge neutralization of negatively charged particles with a cationic polymer (redrawn from [51], [57]).	20
Figure 2.13: Electrostatic patch flocculation of negatively charged particles with a cationic polymer (redrawn from [57]).	21
Figure 2.14: Adsorption of a negatively charged particle with an anionic polymer via a salt linkage (redrawn from [51]).	22
Figure 2.15: Schematic representation of the “grafting from” method (redrawn from [65]).	24
Figure 2.16: Singh’s model for graft (A) and linear (B) polymers (redrawn from [59], [63]).	25
Figure 2.17: Amylose and amylopectin (redrawn from [79]).....	27
Figure 3.1: Chemical reaction scheme for amylopectin- <i>graft</i> -poly(methyl acrylate) (AP-g-PMA).	34
Figure 3.2: Soxhlet extraction apparatus.	35
Figure 3.3: Alkaline hydrolysis reaction scheme of amylopectin- <i>graft</i> -poly(methyl acrylate) (AP-g-PMA) to amylopectin- <i>graft</i> -hydrolyzed-poly(methyl acrylate) (AP-g-H-PMA).....	37

Figure 3.4: Amylopectin- <i>graft</i> -hydrolyzed-poly(methyl acrylate) (AP-g-H-PMA) synthesis overview.....	38
Figure 3.5: Diagram of a typical benchtop flocculation setup.....	48
Figure 3.6: CST apparatus (redrawn from [110]).	49
Figure 3.7: Graphic image of the graduated cylinder initially and after settling.....	50
Figure 3.8: Visual representation of a range of supernatant turbidity.	51
Figure 4.1: Methyl acrylate conversion as a function of methyl acrylate [M] and amylopectin [B] concentration.....	56
Figure 4.2: Grafting efficiency as a function of methyl acrylate [M] and amylopectin [B] concentration.....	57
Figure 4.3: Homopolymer percentage as a function of methyl acrylate [M] and amylopectin [B] concentration.....	58
Figure 4.4: Grafting ratio as a function of methyl acrylate [M] and amylopectin [B] concentration.	59
Figure 4.5: FTIR absorbance spectra of poly(methyl acrylate) (PMA), amylopectin (AP), and amylopectin- <i>graft</i> -poly(methyl acrylate) (AP-g-PMA) (sample GP11).....	61
Figure 4.6: FTIR absorbance spectra of the amylopectin and poly(methyl acrylate) (AP-PMA) blend, amylopectin- <i>graft</i> -poly(methyl acrylate) (AP-g-PMA) (sample GP11), and crude GP11.	63
Figure 4.7: FTIR absorbance spectra of amylopectin- <i>graft</i> -poly(methyl acrylate) (AP-g-PMA) (sample GP3), and amylopectin- <i>graft</i> -hydrolyzed-poly(methyl acrylate) (AP-g-H-PMA) (sample HGP3).	64
Figure 4.8: ¹ H NMR spectrum for amylopectin (AP).....	66
Figure 4.9: ¹ H NMR spectrum for poly(methyl acrylate) (PMA).	67
Figure 4.10: ¹ H NMR spectrum for the amylopectin and poly(methyl acrylate) (AP-PMA) blend.	68
Figure 4.11: ¹ H NMR spectrum for amylopectin- <i>graft</i> -poly(methyl acrylate) (AP-g-PMA) (sample GP10).	68
Figure 4.12: ¹ H NMR spectra of the hydroxyl regions for A) amylopectin (AP), B) amylopectin and poly(methyl acrylate) (AP-PMA) blend, and C) amylopectin- <i>graft</i> -poly(methyl acrylate) (AP-g-PMA) (sample GP10).	69
Figure 4.13: ¹³ C NMR spectrum for amylopectin (AP).....	70

Figure 4.14: ^{13}C NMR spectrum for poly(methyl acrylate) (PMA).	71
Figure 4.15: ^{13}C NMR spectrum for the amylopectin and poly(methyl acrylate) (AP-PMA) blend.	72
Figure 4.16: ^{13}C NMR spectrum for amylopectin- <i>graft</i> -poly(methyl acrylate) (AP-g-PMA) (sample GP10).	72
Figure 4.17: HiM images of commercial amylopectin (AP) powder.	73
Figure 4.18: HiM images of gelatinized amylopectin (AP).	74
Figure 4.19: HiM images of poly(methyl acrylate) (PMA).	74
Figure 4.20: HiM images of the amylopectin and poly(methyl acrylate) (AP-PMA) blend.	75
Figure 4.21: HiM images of amylopectin- <i>graft</i> -poly(methyl acrylate) (AP-g-PMA) (sample GP10).	76
Figure 4.22: Thermal analysis comparison of amylopectin (AP), poly(methyl acrylate) (PMA), amylopectin- <i>graft</i> -poly(methyl acrylate) (AP-g-PMA) (sample GP9), and the amylopectin and poly(methyl acrylate) (AP-PMA) blend.	77
Figure 4.23: Thermal analysis of different grades of amylopectin- <i>graft</i> -poly(methyl acrylate) (AP- g-PMA).	78
Figure 4.24: MFT volume (A) and number (B) particle size distributions.	81
Figure 4.25: A) Normal probability plot, and B) Predicted versus observed values for the ISR model.	85
Figure 4.26: Response surfaces for $\sqrt{\text{ISR}}$	87
Figure 4.27: A) Normal probability plot, and B) Predicted versus observed values for the initial CST model.	88
Figure 4.28: Response surfaces for $(\text{CST } 0\text{h})^{-1}$	90
Figure 4.29: A) Normal probability plot, and B) Predicted versus observed values for the sediment CST model.	91
Figure 4.30: Response surfaces for CST 24h.	93
Figure 4.31: A) Normal probability plot, and B) Predicted versus observed values for the Turbidity model.	94
Figure 4.32: Response surfaces for Turbidity.	95
Figure 4.33: A) ISR comparison, B) Initial CST comparison, C) Sediment CST comparison, D) Turbidity comparison and E) Solids content comparison.	97

Figure A1: FTIR spectra of poly(methyl acrylate) (PMA) in the Soxhlet extraction filtrate at various time intervals.....	114
Figure A2: Precipitated filtrate poly(methyl acrylate) (PMA) at various time intervals (left 24 hours, centre 48 hours, right 72 hours).	115
Figure A3: Amylopectin and poly(methyl acrylate) (AP-PMA) blend (left), and amylopectin-g-poly(methyl acrylate) (AP-g-PMA) (sample GP11) (right), before and after Soxhlet purification (P1) followed by mixing purification (P2).....	116
Figure B1: Residuals versus predicted values for the ISR model (left), Run sequence plot for the ISR model (right).	117
Figure B2: Residuals versus predicted values for the CST 0h model (left), Run sequence plot for the CST 0h model (right).	118
Figure B3: Residuals versus predicted values for the CST 24h model (left), Run sequence plot for the CST 24h model (right).	119
Figure B4: Residuals versus predicted values for the turbidity model (left), Run sequence plot for the turbidity model (right).....	120
Figure C1: A-PAM flocculation series (dosage increases from left to right).	123
Figure C2: AP flocculation series (dosage increases from left to right).	123
Figure C3: H-PMA flocculation series (dosage increases from left to right).	124
Figure C4: Blend flocculation series (dosage increases from left to right).	124
Figure C5: HGP11 flocculation series (dosage increases from left to right).	125
Figure C6: Crude HGP11 flocculation series (dosage increases from left to right).	125
Figure C7: Calcium blank.....	126

Nomenclature

A-PAM	Anionic polyacrylamide
AAS	Atomic absorption spectrophotometry
AER	Alberta Energy Regulator
AGU	Anhydroglucose unit
ANOVA	Analysis of variance
AP	Amylopectin
AP-g-H-PMA	Amylopectin- <i>graft</i> -hydrolyzed-poly(methyl acrylate)
AP-g-PMA	Amylopectin- <i>graft</i> -poly(methyl acrylate)
AP-PMA	Amylopectin and poly(methyl acrylate) blend
ATR	Attenuated total reflectance
bpd	Barrels per day
CCD	Central composite design of experiments
CHWE	Clark hot water extraction
CSS	Cyclic steam stimulation
CST	Capillary suction time
CT	Composite/Consolidated tailings
DI	Deionized water
DLVO	Derjaguin-Landau-Verwey-Overbeek
DMSO	Dimethyl sulfoxide
EDL	Electric double layer
FFT	Fluid fine tailings
FTIR	Fourier-transform infrared spectroscopy
GCOS	Great Canadian Oil Sands Ltd.
GP#	Purified graft copolymer run #
HCl	Hydrochloric acid
HGP#-#k	Hydrolyzed graft copolymer run # & dosage #kppm
HiM	Helium ion microscopy
ISR	Initial settling rate
KPS	Potassium persulfate

MA	Methyl acrylate
MFT	Mature fine tailings
NaOH	Sodium hydroxide
NMR	Nuclear magnetic resonance spectroscopy
NTU	Nephelometric turbidity unit
OSA	Oil sands area
PAM	Polyacrylamide
PMA	Poly(methyl acrylate)
PSD	Particle size distribution
PT	Paste technology
SAGD	Steam assisted gravity drainage
SCO	Synthetic crude oil
TGA	Thermogravimetric analysis
TT	Thickened tailings

1. Introduction

For over half a century, the oil sands industry has been a key contributor to the wealth of Alberta and Canada. Many steps must be taken to make a product that is suitable for consumer use, including extraction of the raw bitumen, upgrading to obtain pipeline-transportable material, and refining to the desired end-use product. Even though this industry has advanced tremendously and provided many jobs over the years, the wastes from the upstream processes are a continuous troublesome environmental matter.

The undesirable materials that are a by-product of these processes, known as oil sands tailings, are a mixture of water, sand, clays, and small amounts of bitumen. These tailings are transported to large temporary settling ponds, but due to their stability, particularly of mature fine tailings (MFT), the suspension does not settle well, which has become one of the largest environmental dilemmas for this industry. Furthermore, despite some advancements in dewatering and consolidation technologies, the continuous accumulation of tailings is occurring faster than its reclamation.

Presently, synthetic polymer flocculants are used to treat tailings, with the industrial standard being high molecular weight anionic polyacrylamides (A-PAM). However, the performance of A-PAM is hindered by its tendency to trap water in the sediments via hydrogen bonding, its shear degradability, and the fact that its properties are not tailored towards the specific composition of MFT. In summary, commercial A-PAM flocculants are ineffective. Other synthetic polymers have been tested to overcome some of these problems, but their lifetime and degradation products may pose environmental risks. Natural polymers are inherently more shear stable but are not favoured by the industry due to their poor ability to flocculate and dewater tailings. Alternatively, natural graft copolymers are easily synthesized, eco-friendly, cost-effective, and modifiable to achieve various responses. Consequently, the objective of this work was to study a natural graft copolymer flocculant for the treatment of MFT.

Amylopectin-*graft*-hydrolyzed-poly(methyl acrylate) (AP-g-H-PMA) flocculants were synthesized and applied to treat MFT in this thesis. Additional objectives included understanding the effects of the microstructure on the graft copolymer performance, and to determine if this new class of materials could become a suitable industrial candidate for tailings treatment. Several

grades of the natural graft copolymer were synthesized and studied. Firstly, amylopectin (AP) was modified by chemically grafting poly(methyl acrylate) (PMA) to its backbone, followed by alkaline hydrolysis. This modification altered the structure, hydrophilicity, and charge density of the graft copolymer, while still maintaining the eco-friendly and shear resistant properties of the AP backbone. Secondly, characterization tests were performed on the polymer flocculants to ensure grafting was successful. Finally, the flocculation performance was evaluated using several metrics to analyze how changing the polymerization variables affected the ability of the polymer to settle and dewater 10 wt.% MFT suspensions. The graft copolymer flocculant was also compared to AP and H-PMA homopolymers, an AP and H-PMA blend, and a commercial anionic polyacrylamide (A-PAM).

This thesis is organized as follows. *Chapter 2* presents background material and a review of the literature encompassing a brief history of the oil sands industry in Alberta, problems with tailings ponds, and current treatment methods. An introduction to natural graft copolymerization is also given and previous publications on amylopectin graft copolymers are reviewed. *Chapter 3* outlines the materials, experimental techniques, and statistical design used for the synthesis, purification, and hydrolysis of the graft copolymers. A description of the characterization methods used for the flocculants and MFT sample is also given. Furthermore, flocculation performance metrics are also introduced in this chapter. *Chapter 4* discusses the results of the research work. In this chapter, the synthesis results regarding the grafting parameters, as well as the flocculant and MFT characterizations are presented and evaluated. The statistical analyses regarding the flocculation metrics and the flocculant comparison results are also discussed in this chapter. *Chapter 5* summarizes the key results of this research and draws conclusions based on the findings. Various routes for future studies are also proposed to fill current knowledge gaps.

2. Background and Literature Review

2.1 Oil Sands and Oil Production in Alberta

2.1.1 Alberta's Oil Sands Reserves

Oil production is a key industry in Canada. It contributes significantly to the national economy and employs more than 400,000 people [1]. Canada holds the third-largest oil reserves in the world, only behind Venezuela and Saudi Arabia, with an estimated total of 171 billion barrels remaining in the established conventional and oil sands reserves [2]. Approximately 97% of this total (about 165 billion barrels) is found in the Alberta oil sands [1]–[3]. These deposits are located in the northeastern part of the province and cover approximately 142,000 km² of land covered by boreal forests, prairies, and muskeg in three oil sands areas (OSA): the Athabasca Basin, the Cold Lake Basin and the Peace River Basin (Figure 2.1) [1], [4]. Currently, Alberta produces and exports an estimated 2.5 million barrels per day (bpd) of crude bitumen, but this number is forecasted to increase to about 4 million bpd by 2025 [3].



Figure 2.1: Alberta's oil sands areas (redrawn from [4]).

2.1.2 Oil Sands Composition and the Bitumen Extraction Process

Alberta's oil sands ore is a form of sandstone containing a heavy crude oil known as bitumen. This ore is a mixture of 3-5% water, 8-12% bitumen, 10% sand and various clays, and 75% inorganic materials [5]–[8]. These amounts, however, vary depending on the location and depth of the deposit.

The production of Canada's oil sands began in 1967 and over the last 50 years has expanded due to developments in the extraction and upgrading sectors. Figure 2.2 illustrates the two main methods used in Alberta to extract bitumen. *Surface mining* methods (for shallow deposits < 75 m) and thermal *in-situ* technologies (for deep deposits > 200 m) [1], [3], [9]. For reservoirs between these two depths, neither method is economically viable [9]. The amount of recoverable oil varies based on the extraction method: over 90% is achievable using mining methods, but in-situ technology can only reach up to 60% [8]. Regardless, only 20% of the total oil sands reserves are mineable; the remaining 80% must be reached through in-situ drilling [10].

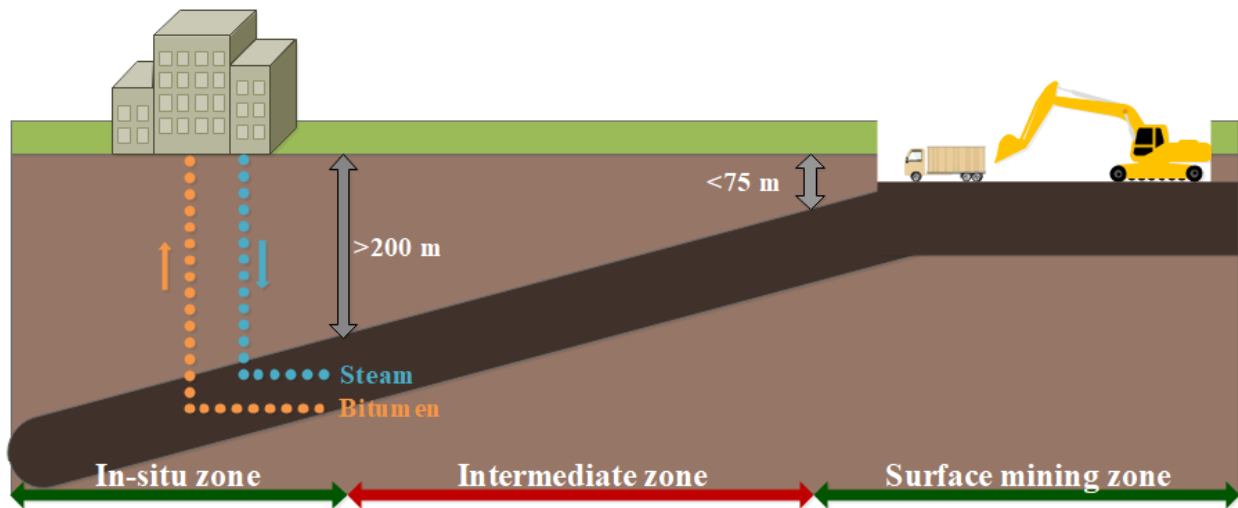


Figure 2.2: In-situ and surface mining bitumen extraction (redrawn from [11]).

Surface mining uses shovels and trucks to extract ore from the reserves closer to the surface. The Athabasca oil sands area is the largest of the three, and it is the only one with reserves

that are shallow enough to be mined [4]. In this method, the ore is shoveled out of the mine, loaded into transport trucks, and taken to the processing plant. At the plant, the ore is dumped into a crusher to break down any oversized materials. A slurry made up of hot water and caustic soda (NaOH, pH \approx 9) is added to disperse the sands and clays and to ease bitumen separation [6], [12]. A special pipeline with several pumps, known as a hydrotransport, is then used to move this slurry to the main plant for primary extraction of the bitumen froth. This well-known process of water-based bitumen separation was pioneered by many researchers in the early 1920s, most notably by the Research Council of Alberta and Dr. Karl Clark [13], [14]. The Clark Hot Water Extraction process (CHWE) was patented in 1929 and achieved its first commercial large-scale application in 1967 by the Great Canadian Oil Sands (GCOS) [5], [14]. This was a turning point in the industry, as the efficiency and economical attributes of this invention helped propel the oil sands industry in Alberta.

Currently, the active mining footprint in Alberta is less than 1% (901 km²) of the total surface area covered by the oil reserves and only 3% can ever be reached by mining activities [10]. Therefore, improvements for in-situ extraction methods are becoming increasingly important for the future of bitumen recovery.

For in-situ extraction, steam or solvent is injected into the deep deposits to heat and separate the bitumen enough to be pumped to the surface [8]. As the production of steam is energy intensive, greenhouse gas emissions are a large consideration for in-situ systems. Commercially, some techniques employed for in-situ extraction include Steam Assisted Gravity Drainage (SAGD), and Cyclic Steam Stimulation (CSS) [10]. In the commonly used SAGD method, two horizontal wells are drilled parallel to each other to allow steam injection in the upper well while bitumen and condensed steam are recovered in the lower well [3], [4]. Despite higher emissions and lower recovery rates compared to mining, in-situ methods are increasing in popularity. In-situ facilities have a smaller land footprint, utilize water more efficiently, create fewer unwanted materials, and once established are more economical than mining facilities [6].

2.1.3 Bitumen Upgrading and Refining

Once the raw bitumen is extracted from the oil sand ore, it needs to be processed before it is transported downstream for refining. In the petroleum industry, crude oil and bitumen are sold based on their liquid densities. Bitumen is dense, highly viscous, and contains contaminants such as asphaltenes and sulfur. Raw bitumen is too viscous to flow in pipelines. In the industry, its viscosity can be lowered through several methods, including *diluent addition*, *upgrading* or *partial upgrading*, as shown in Figure 2.3.

Adding diluent to raw bitumen decreases its viscosity and density to values that allow it to be transported to a refinery. The two major diluent types used in industry are condensate, which produces a light blend known as *dilbit*, or synthetic crude oil (SCO), which makes a heavier blend called *synbit* [15], [16]. Despite the ease of blending, diluent is costly and as large volumes are required to meet regulations, the oil capacity in pipelines is restricted [15]. This capacity is severely decreased when producing synbit, as upwards of 50% by volume of SCO is needed, while dilbit requires only 30% condensate to meet the same pipeline specifications [15], [16]. In Alberta, condensate is largely preferred because, unlike SCO, it can be recycled and reused, or used in refining operations downstream [15].

Due to constraints associated with diluent use, other practices, including upgrading and partial upgrading methods, have been employed. Upgrading is a process that requires either physical separation, chemical reactions, or a combination of both to remove asphaltenes and other contaminants to enhance the product quality [17]. In upgrading plants, the chemical composition of bitumen changes by eliminating undesired components to create SCO, which is further treated at light oil refineries. Despite of using no diluent and producing a higher quality product, this process is capital intensive and costly to operate [17]. Additionally, full upgraders in Alberta have a limited capacity which is quickly being surpassed by the growth in oil sands production. Partial upgrading is a newer technology that applies aspects of both diluent addition and complete upgrading. This method benefits from lower capital and operating costs than complete upgrading and the resulting product is a heavy oil that can meet pipeline specs with less diluent [15]. To be practicable in industry, partial upgraders must have substantially lower capital costs than full

upgraders, as well as lower total costs than purchasing and blending diluent to meet the same pipeline specifications [18].

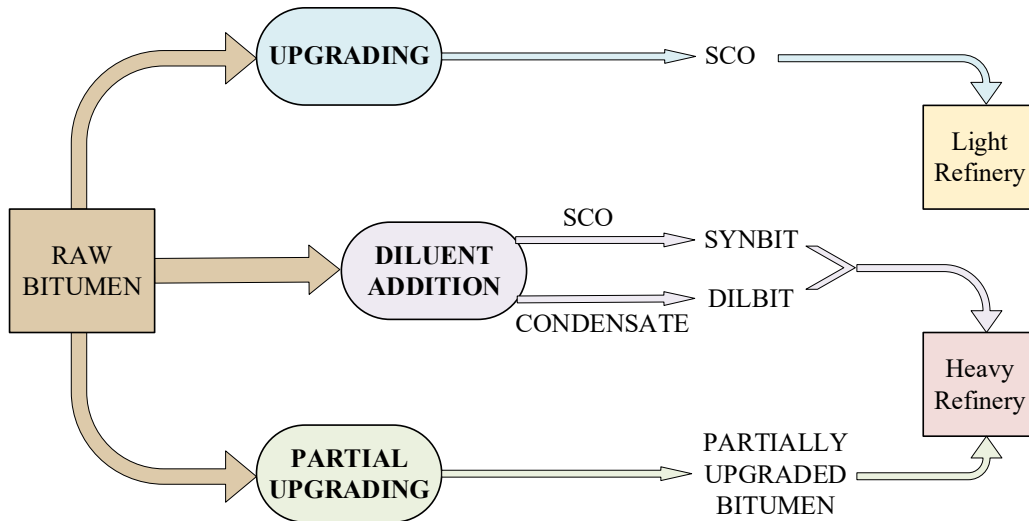


Figure 2.3: Bitumen pathways to market (redrawn from [15]).

2.1.4 Water Usage

Water is a key component in the oil sands industry because it is needed to extract bitumen. The amount of water that is consumed in the extraction of bitumen differs considerably based on the method employed. In mining techniques, 2.5 to 4 barrels of fresh water are required to produce 1 barrel of SCO; conversely, 0.21 to 0.5 barrels of fresh water per barrel of SCO are used in in-situ facilities [10], [19], [20]. Furthermore, as the Alberta government has a strict *zero discharge policy*, the process water used must remain on-site and, on average, 80% (for mining facilities) to 94% (for in-situ facilities) is recycled back into the process [20]. It is important to point out that the water trapped in waste materials (such as tailings) after bitumen extraction and upgrading can have a substantial long-term impact on the environment and, therefore, needs to be managed.

2.2 The Tailings Problem and Management Techniques

2.2.1 Tailings Ponds

Oil sands tailings ponds are formed from the waste by-products of both extraction and upgrading practices. In surface mining technologies, approximately 3.3 m³ of by-product waste is created in the extraction of 1 barrel of crude bitumen [4]. This effluent is known as oil sands tailings and is made up of a mixture of coarse sands, fine silt, clays (mainly kaolinite and illite), water, and unrecovered bitumen. Several other compounds may be found in these tailings, including metal salts, naphthenic acids, polycyclic aromatic hydrocarbons, and other inorganic and organic contaminants [12]. Tailings are transported away from the extraction facility to large ponds which are used to help settle materials and reclaim water, as seen in Figure 2.4. In Alberta, these man-made ponds cover approximately 176 km² of land and are associated with problems related to the quality of the recycled water, the negative impact on the surrounding environment, and effects on wildlife [21].

A major problem with these ponds arises from the limited consolidation of mature fine tailings (MFT). When a fresh tailings slurry is discharged into a pond, larger and heavier materials, such as sands and clays, separate and settle rapidly [22]. As these heavier constituents settle to the bottom of the pond, a large amount of recyclable water is released to the top. Unfortunately, a significant fraction of the water remains trapped with about 6 to 10 wt.% of the fine solids [23]. This heterogeneous mixture does not settle noticeably and is termed fluid fine tailings (FFT). After several years, the FFT degrade to a thick and gel-like sludge in the middle layer of the pond. This layer, made up of a mixture of 20 to 30 wt.% fine solids, 70 to 80 wt.% water, and 1 to 3 wt.% bitumen, is known as mature fine tailings (MFT) [4], [12], [22]. Treating MFT is notoriously difficult, as its properties vary depending on the location of the deposit from which the ore was extracted and the method of processing. These variations include differing clay surface areas, particle sizes, charges, and chemical species [21].

Even though the inability to recycle the large amount of water trapped in MFT is one of the major issues associated with these ponds, other complications also exist. The chemistry of the recovered process water is a large consideration because it contains many of the harmful compounds found in the tailings themselves; water quality affects not only bitumen recovery but

the integrity of the equipment in the extraction plant. Furthermore, the land occupied by tailings ponds must be reclaimed to create trafficable surfaces that can sustain vegetation and wildlife [24]. For this goal to be met, the sediments shear strength and solids content at the base of the pond must increase to improve its mechanical properties [25].

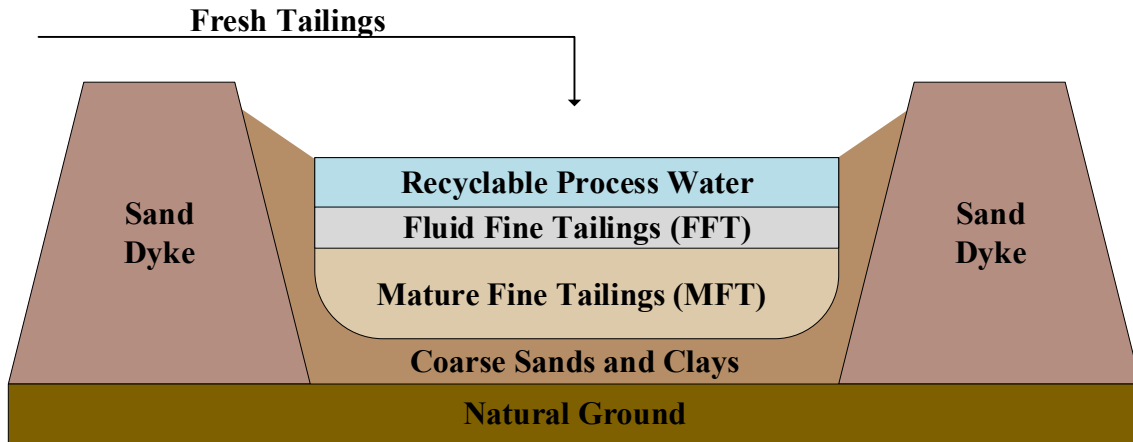


Figure 2.4: Oil sands tailings pond diagram (redrawn from [26]).

Since the volume of tailings is increasing faster than the land from these ponds can be reclaimed, their remediation has become a major concern for the province. The Alberta Energy Regulator (AER) implemented *Directive 085: Fluid Tailings Management for Oil Sands Mining Projects* in July of 2016. This directive holds companies accountable and enforces explicit rules regarding progressive reclamation through the reduction of the overall volume of fluid tailings to deal with pre-existing (legacy) tailings as well as new tailings growth [27]. As a result, the industry and academia have allocated more resources to investigate alternate ways to dewater and minimize tailings.

2.2.2 General Treatment Technologies

Oil sands tailings treatment methods can be divided into five main categories: 1) physical or mechanical processes, 2) natural processes, 3) chemical or biological processes, 4) mixtures or

co-disposal, and 5) permanent storage [28]. The first category involves using physical/mechanical methods to separate the reusable water from the solids. Natural processes attain the same goal by environmental or geophysical means, while chemical modification changes the tailings properties to release water. In the fourth category, tailings are mixed with other materials or waste products to increase their density. Finally, when permanent storage methods are used, tailings are not treated, but simply stored in their original condition. Two oil sands tailings treatment technologies that have been used in large-scale industrial operations include composite/consolidated tailings and paste/thickened tailings [29].

2.2.3 Composite/Consolidated Tailings

A key technology used for MFT treatment in the mixtures and co-disposal category is known as Composite or Consolidated Tailings (CT). In this method, a 60 wt.% solids non-segregating slurry is created by mixing coarse sands from fresh tailings, MFT (4:1 sand to fines ratio) and a chemical additive, typically gypsum [25], [28], [30], [31]. This slurry is then transferred to CT deposit sites where the fine and coarse particles aggregate to form dense sediments. The addition of sand enhances settling, promotes faster water release, and improves the strength of the deposits. Additionally, this process has low operational costs and has been implemented on a large scale [28].

Though the CT process may reduce legacy tailings, a major disadvantage is the change in water chemistry, with an eventual build-up of ions (Ca^{2+} and SO_4^{2-}) in the recycled water that can cause scaling in the equipment, as well as hinder bitumen recovery [29]–[31]. Furthermore, using polymer flocculants in the CT process is still under investigation, as CT deposits made by flocculation are generally unable to meet geotechnical benchmarks.

2.2.4 Paste Technology/Thickened Tailings

Paste technology (PT), also known as Thickened Tailings (TT), is another major treatment method for oil sands tailings. In this chemical modification process, additives such as polymer

flocculants are added to a fluid fine tailings slurry in a thickener vessel. The resulting flocs settle rapidly creating a thick paste. Unlike the transformation of fresh tailings to MFT, which may take several years, PT can accelerate this timeline to about half an hour [29]. Typically, the paste consists of approximately 25-30 wt.% solids, but higher solids contents are achievable with the addition of sand [28], [29], [32]. This is an appealing strategy due to its reduced energy costs and greenhouse gas emissions. Since the water recovered from the slurry is still warm (between 30-50 °C), it can be reused in the extraction process with little reheating [28], [32].

Despite these advantages, tailings ponds are still required. The thickened paste resembles MFT and still retains large amounts of water that cannot be easily extracted. Furthermore, the type of polymer flocculant largely affects the efficiency of this method. Currently, the polymers used are not tailored to perform well in the presence of bitumen [28], [29], [32]. Other significant drawbacks include high start-up and operational costs, the impact of bitumen build-up in the flocculation vessel, equipment limitations (such as pumping the high viscosity paste through pipelines), and inability to treat legacy MFT [28].

As a result of these limitations, there is a need to improve tailings treatment technologies. To do so, it is important to understand the colloidal nature of tailings, particularly MFT, and how destabilization occurs.

2.3 The Colloidal Nature of Mature Fine Tailings

2.3.1 Stability of Mature Fine Tailings

Though dispersed clays are beneficial for bitumen liberation, because the negatively charged fine clay particles remain dispersed in MFT, they also create a stable, gel-like colloidal suspension. Fines in the oil sands industry categorizes solids smaller than 44 μm , while clays include mineral solids smaller than 2 μm [33]–[35]. Typically, coagulants, flocculants or a combination of the two may be used to destabilize tailings and aggregate their particles. Surface forces play a large role in this stability. The Derjaguin-Landau-Verwey-Overbeek (DLVO) colloidal stability theory can be used to explain these forces and how particle aggregation occurs

[21], [36]. This theory considers the total net interaction of both attractive and repulsive forces as a function of the distance among neighbouring colloidal particles. Attractive forces arise from van der Waals forces while repulsive forces are due to the electric double layer, as shown in Figure 2.5.

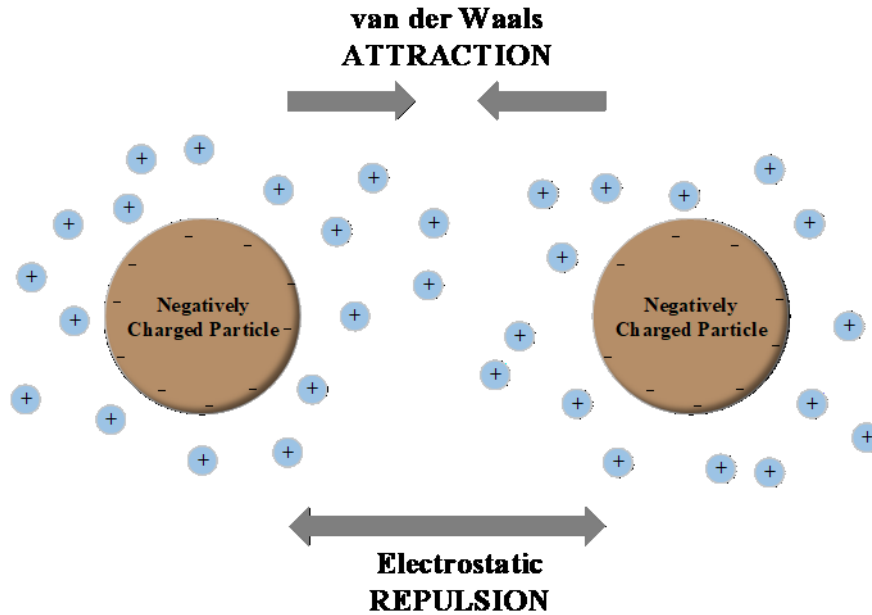


Figure 2.5: Attractive and repulsive interactions between particles (redrawn from [37]).

Van der Waals forces account for intermolecular forces between molecules, excluding electrostatic interactions, chemical, and ionic bonds. Figure 2.6 shows the van der Waals interactions from strongest to weakest, including Keesom, Debye, and London dispersion forces [38]. Keesom forces occur due to permanent dipole–permanent dipole interactions [37]. When two permanent dipoles are oriented in an anti-parallel fashion, they will attract each other. Debye forces result from permanent dipole-induced dipole systems [37]. The weakest, but most prevalent interactions, are London dispersion forces between induced dipoles [37]. These interactions arise due to momentary random charge fluctuations that create attractive neighbouring induced dipoles. Compared to other intermolecular forces, van der Waals forces are weak and occur only in close

range. In fact, they become negligible at distances greater than about 100 nm [39]. As such, as in the case of MFT, they are largely overcome by repulsive forces [40].

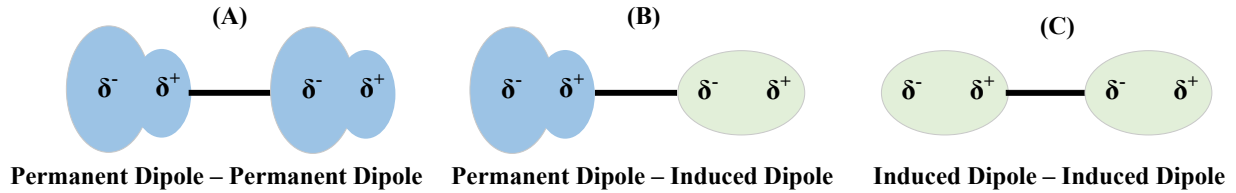


Figure 2.6: Keesom forces (A), Debye forces (B), and London dispersion forces (C) (redrawn from [41]).

Repulsion forces are due to the electrical double layer (EDL), as displayed in Figure 2.7. A negatively-charged colloidal particle in suspension has two layers of charges surrounding it (the EDL). The electric potential at the particle surface is referred to as surface potential. The first layer surrounding the particle contains immobile positively charged ions, known as counterions, that are attracted to the surface by electrostatic forces. This layer is known as the Stern or Helmholtz layer and has an associated electric potential on its outer boundary known as the Stern potential, ψ_S [42], [43]. The electric potential decreases linearly from the surface to the Stern plane. The second layer is termed the diffuse layer and is comprised of mobile ions [42], [43]. This layer is loosely affected by the particle surface charges; thus, the counterion concentration is high closest to the particle but decreases farther away from it. It is important to note that in the diffuse layer a slipping or shear plane is conventionally presented as the limit separating mobile fluid from the fluid that remains attached to the particle as it moves in the medium [44]. The electrical potential at this plane is called the electrokinetic or zeta potential, ζ [44]. Past the Stern plane, the electrical potential decreases exponentially and reaches zero at the EDL boundary.

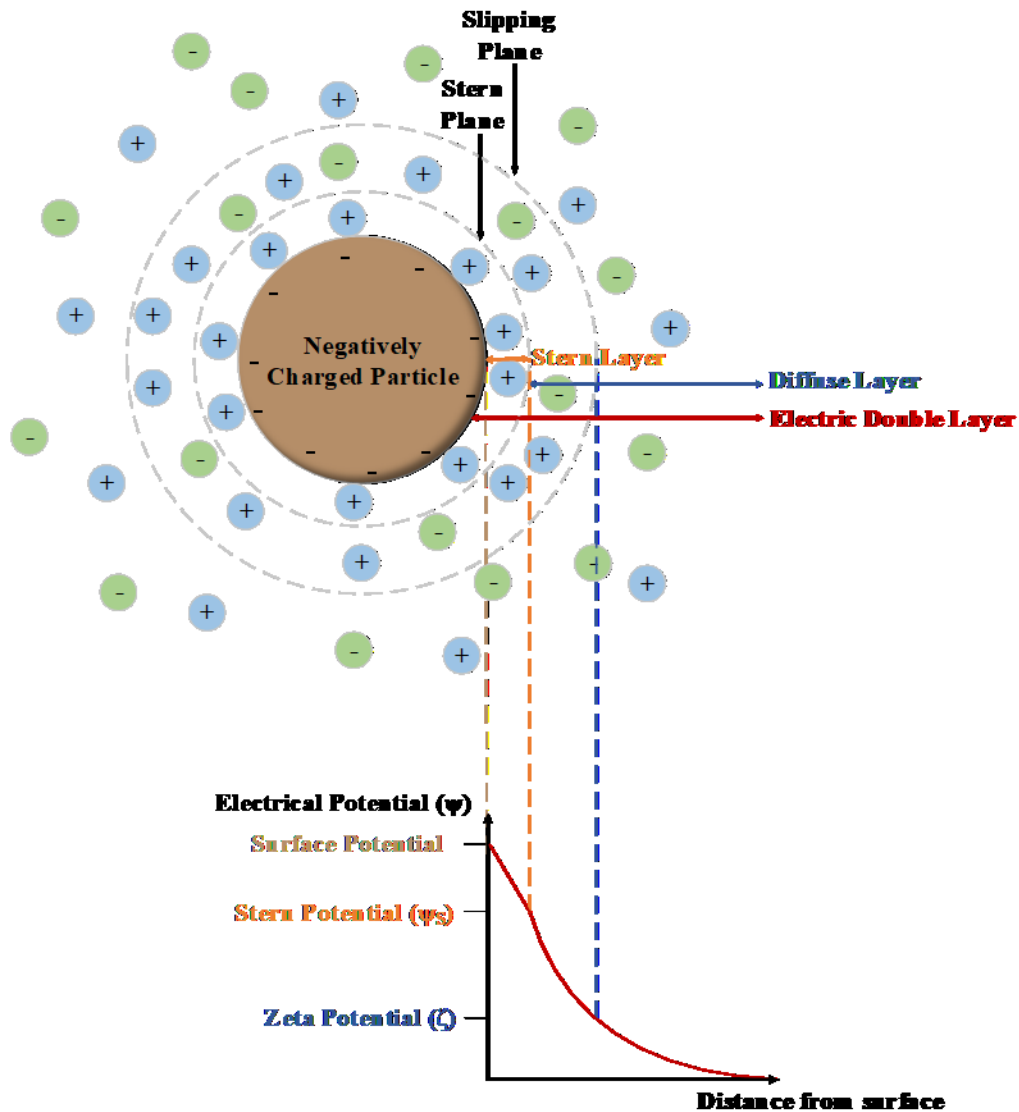


Figure 2.7: Electric double layer diagram (redrawn from [37]).

The DLVO interaction profile shown in Figure 2.8 is the total interaction energy curve of the combined repulsive EDL and attractive van der Waals potentials as a function of the distance between two spherical particle surfaces [37]. A small well, known as the secondary minimum, exists at larger distances, and a deep well, termed the primary minimum, exists when the particles come into contact. At distances between these two wells, the interaction profile goes through a maximum, known as the energy barrier. The height of the energy barrier indicates the stability of the system [37], [42], [45]. In the case of MFT, the net interaction of the suspension is repulsive. Accordingly, the system is stable, and the particles are dispersed. For destabilization and

aggregation of particles to occur, the energy barrier must be lowered, or either the thermal or mechanical energy of the particles must be high enough to surpass it [36].

It should be noted that even though the DLVO theory works reasonably well for MFT, it is geared towards zero-charge isotropic particle suspensions. As the clay particles in MFT are anisotropic, the system cannot be fully described by this theory [21]. The DLVO theory is, therefore, limited in the case of MFT as some non-DLVO forces should be considered, including hydrophobic forces, steric forces, and hydration forces [21], [40].

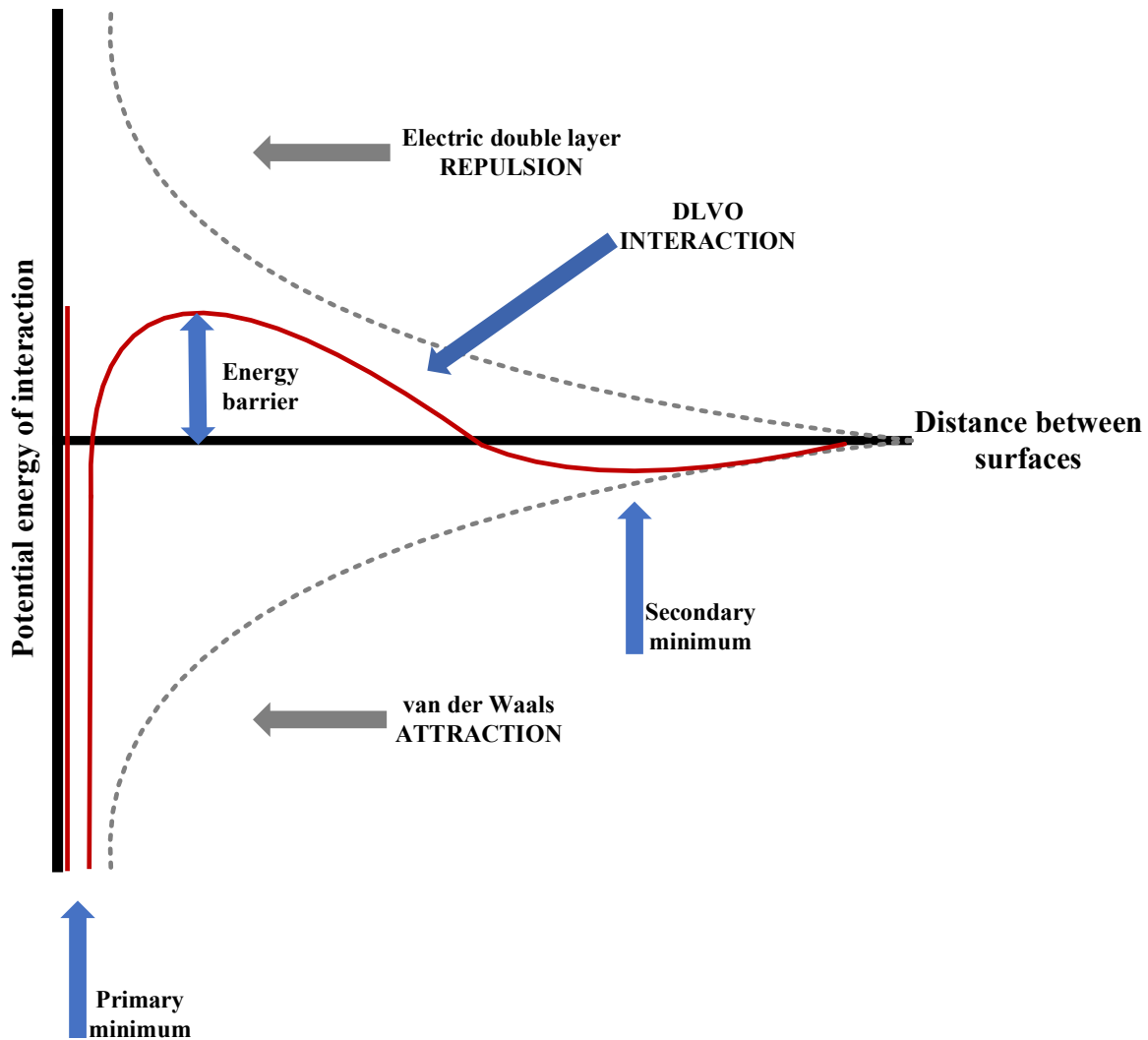


Figure 2.8: DLVO interaction curve (redrawn from [37], [43]).

2.3.2 Flocculation and Coagulation

Additives such as coagulants, flocculants, or a combination of both can be used to destabilize and aggregate the fine particles in MFT, as seen in Figure 2.9. Notably, the figure used is not to scale and is exaggerated to portray the mechanism occurring. Inorganic metal salts are coagulants that dissociate in aqueous solutions. Common coagulants for wastewater treatment include alum, sodium aluminate, ferrous sulphate, lime, acid, and ferric chloride [30], [46], [47]. For the case of tailings treatment, gypsum has proven to be the most practicable coagulant option [29]. These coagulants destabilize the system as the (typically multivalent) cations (Al^{3+} , Mg^{2+} , Cu^{2+} , Fe^{3+} , or Ca^{2+}) are attracted to the negatively charged clay particles [47], [48]. Reducing the electrostatic repulsive force compresses the EDL surrounding neighbouring particles and lowers the energy barrier, allowing the van der Waals attraction forces to dominate and micro flocs to form [49]. However, the use of inorganic coagulants increases the concentration of residual ions in the treated water, which may reduce bitumen recovery [30], [50]. Furthermore, coagulants create small flocs that tend to shear easily. The use of inorganic coagulants can be lowered or even eliminated using polymer flocculants [51].

Flocculation is another method for aggregating fine particles or micro flocs to enhance solid-liquid separation. It is typically a two-stage process where the destabilization of particles occurs followed by a stage of increasing floc growth [36]. Flocculants are water-soluble, typically high molecular weight synthetic or natural polymers that can aggregate the clay particles and create large flocs through molecular bridges. Polymers can also be categorized by their ionic charges as cationic, anionic, or non-ionic. Polymers that contain an ionic charge are also known as polyelectrolytes [52]. To create effective polymer flocculants, some key concepts must be understood, including the mechanisms of polymer-particle interactions during flocculation.

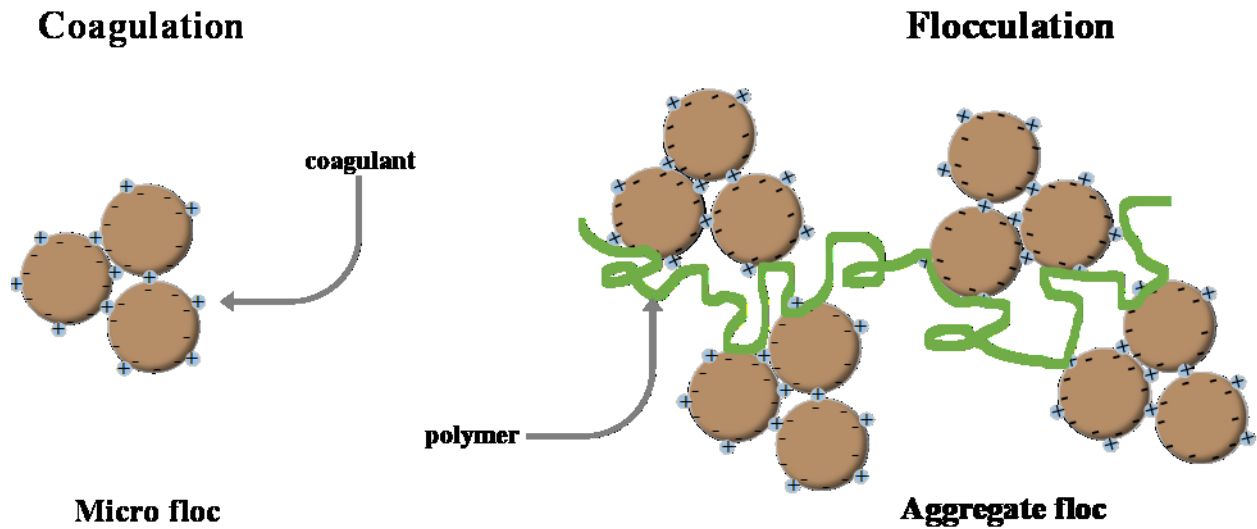


Figure 2.9: Particle aggregation by coagulation followed by flocculation.

2.3.3 Flocculation Mechanisms

Polymers aggregate the fine clay particles in MFT. Based on the DLVO theory, flocculation occurs when the particles aggregate in the secondary minimum [37]. Typically, high molecular weight polymers are used because longer chains are more likely to adsorb onto the clay particle surfaces and extend beyond the electrical double layer [32], [53]. The MFT should be stirred when the polymer flocculant is added to increase polymer dispersion and particle collisions [48]. Floccs are formed after the polymer disperses in the water phase, diffuses towards the solid-liquid interface, and adsorbs onto the particle surfaces [32]. It is important to note that flocculation cannot occur without this adsorption step. Up to a certain extent, increasing the particle collision frequency leads to the formation of larger floccs [54]. The conformation of the adsorbed polymer molecules on the surface of the clays also plays a role in its performance. For optimal efficacy, the polymer should not fully cover the surface, but form short “trains” that attach to the surface, while middle “loops” and end “tails” extend out into the solution, making it possible to adsorb to more than one particle, as shown in Figure 2.10 [36].

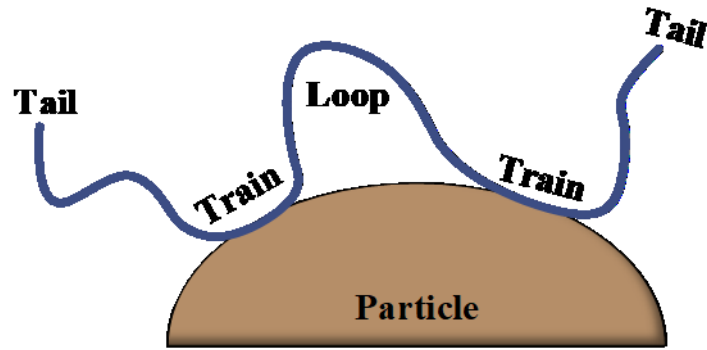


Figure 2.10: Segment conformations of an adsorbed polymer on a particle surface (redrawn from [36], [39]).

Figure 2.11, Figure 2.12, and Figure 2.13 show the three dominant flocculation mechanisms that may follow adsorption: polymer bridging, charge neutralization, and electrostatic patch formation [51], [52], [54], [55].

Polymer bridging results from the addition of very high molecular weight polymers, as shown in Figure 2.11. As high molecular weight polymers have long tails and loops, they can extend from the surface of the particle into the solution beyond the electrical double layer, allowing the individual polymer chains to adsorb onto multiple particles simultaneously, creating large flocs [51], [54], [56], [57]. Non-ionic polymers adsorb to particles via hydrogen bonding. Despite being relatively weak, the large number of hydrogen bonds created between polymer chain and solid surface leads to strong adsorption [51], [57]. Since low molecular weight polymers have shorter chains that cannot extend as far into the solution, they are typically less effective at bridging particles together [54]. Polymer bridging also depends on the fraction of unoccupied space on the clay surface. If too much polymer is adsorbed onto the particle surfaces, there will be little to no available sites for bridging, and thus, steric stabilization and redispersion may occur [56], [58]. The optimum flocculant dosage is obtained when the adsorption density is adjusted to achieve maximum bridging.

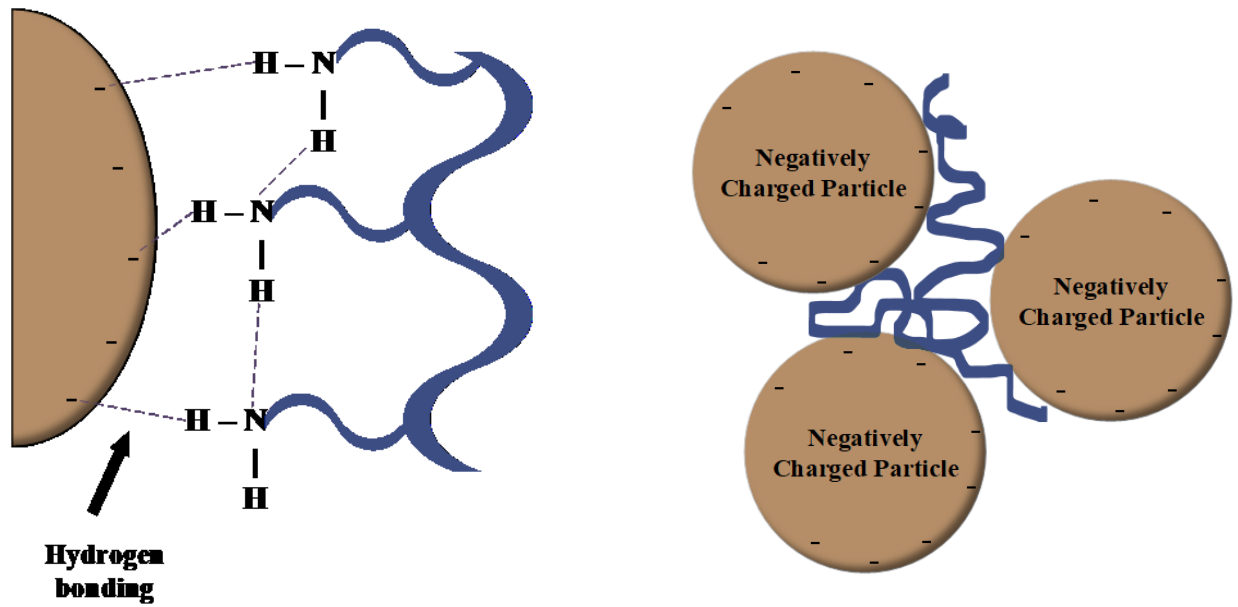


Figure 2.11: Adsorption and polymer bridging of negatively charged particles with a neutral polymer (redrawn from [51], [57]).

Charge neutralization occurs when the flocculant carries an opposite charge to that of the clay particle, as seen in Figure 2.12. In this case, the attraction between the opposite charges destabilizes the repulsive charges on the clay particle surface, and flocs can then be formed through van der Waals attraction forces. For this mechanism, the optimum flocculant dosage is achieved at the isoelectric point (zeta potential = 0) when the charges are completely neutralized [56]. Polymer overdose results when an excess of polyelectrolyte is used. This excess charge may reverse the overall particle charge and re-stabilize the suspension, allowing the particles to become dispersed again.

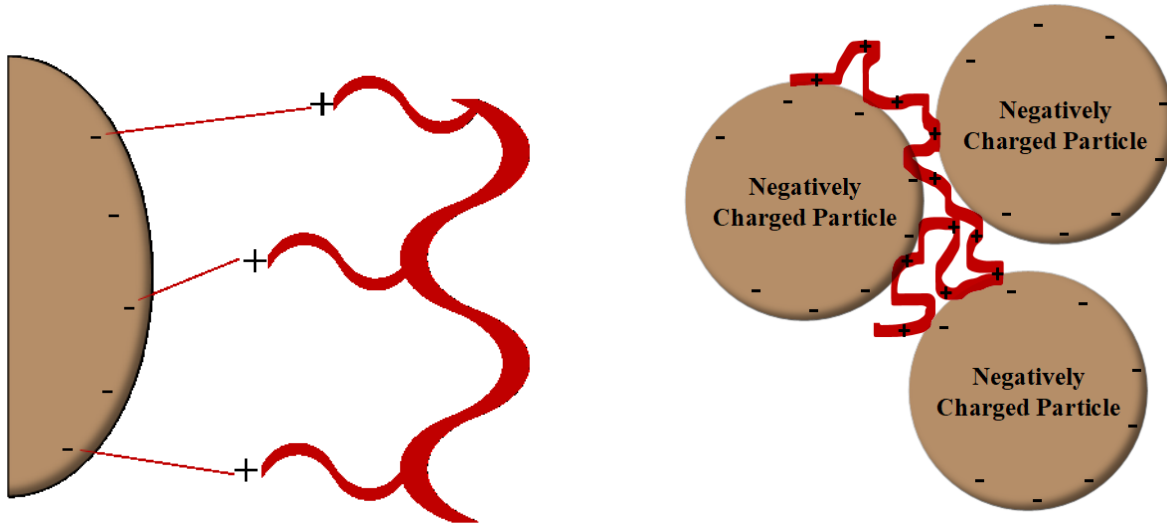


Figure 2.12: Adsorption and charge neutralization of negatively charged particles with a cationic polymer (redrawn from [51], [57]).

Electrostatic patch formation may occur when a low molecular weight polyelectrolyte is added to the suspension (Figure 2.13). The polyelectrolyte creates a localized patch of reverse charge when attached to a clay particle [51]. Even though the likelihood of obtaining complete charge neutralization is low, when a high charge density of polyelectrolyte is added, charged patches may form on the clay particle surface which can attach to other particles. This electrostatic patch forms flocs through the continuous attraction and attachment to other clay particles. These flocs, however, tend to be shear sensitive [51], [56].

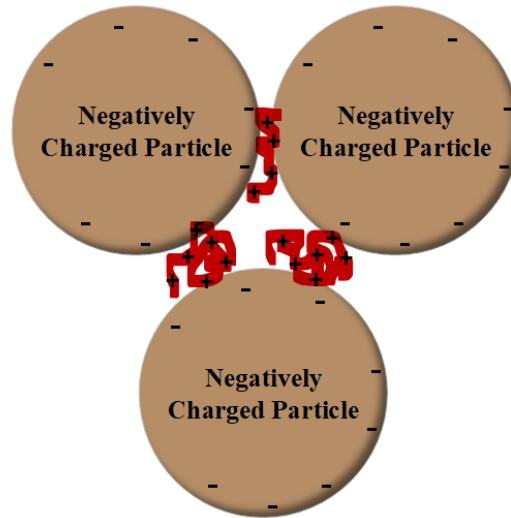


Figure 2.13: Electrostatic patch flocculation of negatively charged particles with a cationic polymer (redrawn from [57]).

The charge of the clay particles and of the polymer also determine whether coagulant addition is needed. For the negatively charged clays in MFT, no coagulant is needed if the polyelectrolyte is cationic. On the other hand, for anionic polyelectrolytes and negatively charged particles, a cationic coagulant must be added to create salt linkages between the particle and polymer, as seen in Figure 2.14 [51]. Here, the salt linkages allow the polymer to adsorb onto the clay surface and form flocs through polymer bridging.

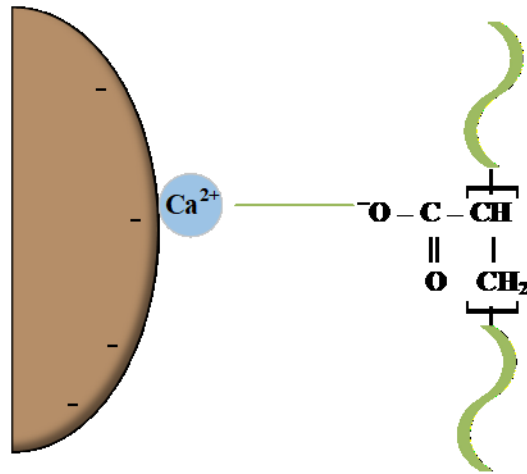


Figure 2.14: Adsorption of a negatively charged particle with an anionic polymer via a salt linkage (redrawn from [51]).

2.4 Synthetic, Natural, and Graft Copolymer Flocculants

2.4.1 Synthetic and Natural Polymers

Synthetic and natural polymers have been investigated for their flocculation efficacy. Typically, synthetic polymers are used to treat and dewater various industrial effluents, wastewater, and mineral tailings. More recently, environmental and ecological concerns have spiked the interest in eco-friendly and bio-based flocculants.

Synthetic polymers are manmade, highly efficient, tailorable, flexible, and perform well at low dosages. Commonly used polymer flocculants for MFT dewatering include anionic polyacrylamide, poly(diallyl dimethyl ammonium chloride), and polyacrylic acid [29], [54]. These polymers, however, may degrade into environmentally harmful compounds and tend to be shear sensitive [54], [59]–[65]. As many polymer properties affect flocculation (such as molecular weight, configuration, chemical composition, ionic charge type, and charge density), synthetic polymers are advantageous as they can be custom-made for the desired operation [29]. Despite their good performance, shear stability is a large concern because the treated tailings undergo high shear forces when they are pumped through pipelines to the tailings ponds. If the flocs are irreversibly damaged, the effect of the polymer is largely decreased.

Bio-based polymers are found in nature from abundant sources including plants, tree bark, seeds, nuts, shellfish exoskeletons, bone and shell extracts, and some soils [66]. Common natural polymers include starch, cellulose, chitosan, tannin, alginate, gums, and their derivatives [54], [67]. These polymers are inherently more rigid and shear resistant, available at a low cost, and are largely eco-friendly. Unfortunately, they are only effective at high dosages and their biodegradability can shorten their shelf lives [54], [59]–[65].

Even though both polymer categories have advantages, they also have drawbacks that can hinder their usability. Recent works have attempted to combine the beneficial properties of synthetic and natural polymers by synthesizing hybrid polymers known as natural graft copolymers.

2.4.2 Natural Graft Copolymers

Graft copolymerization is a technique that modifies polymer backbones by incorporating branches or grafts to change some of the chemical and/or physical properties of the backbones [68]. The use of natural graft copolymers in flocculation is a growing field of research and several of these polymers have been studied. In natural graft copolymers, the natural polymer forms the backbone to which the synthetic polymer chains are grafted via covalent bonds to create comb-like structures. Three main grafting mechanisms have been studied: 1) grafting through, 2) grafting onto, and 3) grafting from [65], [69]. Figure 2.15 shows the “grafting from” method that has been extensively studied, particularly for free radical polymerizations of natural copolymers. This technique involves growing the synthetic polymer chains directly from active sites generated on the natural polymer backbone [65]. Various “grafting from” methods exist including, chemical methods (free radical initiators or redox systems), radiation-induced grafting, enzymatic grafting, or plasma-initiated grafting [70].

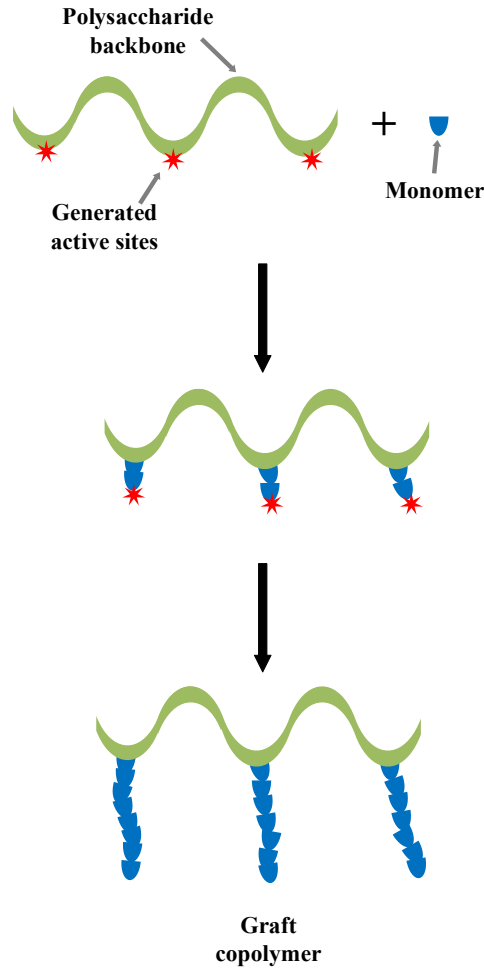


Figure 2.15: Schematic representation of the “grafting from” method (redrawn from [65]).

Grafting synthetic polymers onto shear resistant natural polymer backbones improves their shear stability. Moreover, natural graft copolymers are better flocculants than their natural backbones [71]. Singh’s *easy approachability model* may be used to explain why natural graft copolymers are better flocculants [63], [72]. The model proposes that very long linear chains that extend far into solution are needed for effective bridging because they create flocs by adsorbing onto the particle surfaces and linking them with loops and tails. Conversely, the dangling side chains of graft copolymers can approach the colloidal particles more easily, which favours strong bridging with many particles, as seen in Figure 2.16 [58], [59], [71]–[74]. Additionally, the Brostow, Pal, and Singh model relates effective flocculation to polymers pervading large volumes in solution and thus having a large radius of gyration and hydrodynamic radius [60], [75].

According to this model, as grafting increases the pervaded volume and the radius of gyration of a polymer, its flocculation efficacy should also improve.

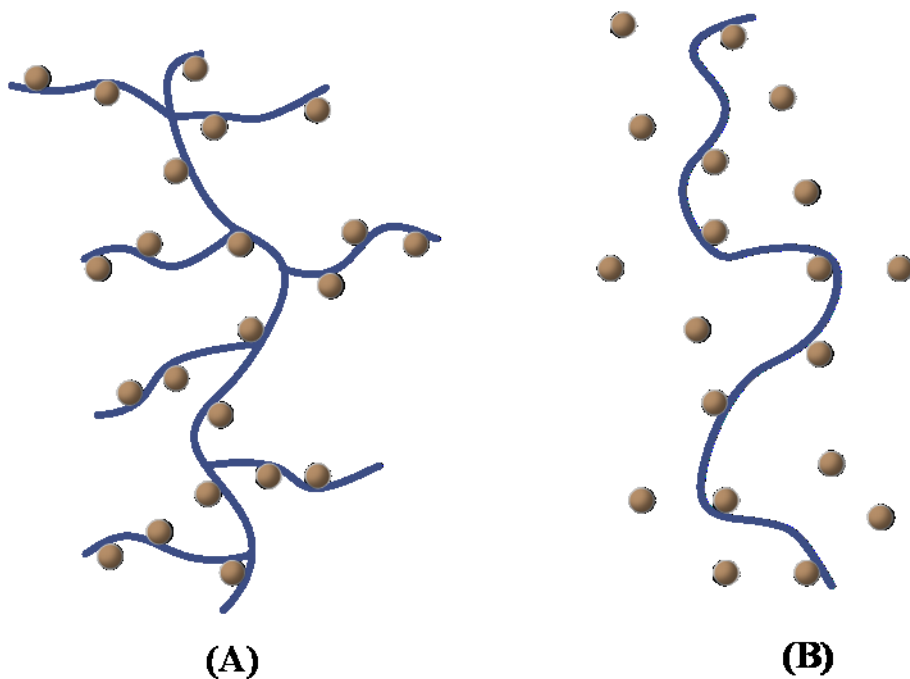


Figure 2.16: Singh's model for graft (A) and linear (B) polymers (redrawn from [59], [63]).

2.5 Amylopectin Based Copolymers

2.5.1 Starch, Amylose, and Amylopectin

Polysaccharide-based graft copolymers have largely been studied for many applications, including drug delivery, dye removal, superabsorbents, ion exchangers, and flocculants [68], [70], [76]. Polysaccharides are the most abundant natural source of organic material on Earth. They include starch, glycogen, cellulose, dextrin, guar gum, and chitosan. They have attractive physical and chemical properties, including high rigidity, relatively high molecular weight, and the presence of polar functional groups [70]. The hydroxyl groups on the polysaccharide backbones provide reactive sites for grafting. Furthermore, investigations of several polysaccharides (guar gum, xanthan gum, carboxymethyl cellulose, and starch) grafted with polyacrylamide (PAM) have

shown that they perform well as flocculants [63], [72], [76]. Starch and its derivatives have received considerable attention from researchers due to its superior performance, abundance, inexpensiveness, and easy modification by grafting vinyl monomers [68].

Starch constitutes a major source of energy required for life. It can be found in roots, grains, fruits, stems, and many other sources [76], [77]. Starch is comprised of two different polymers, amylose and amylopectin, that are made up of anhydroglucose units (AGU), as seen in Figure 2.17 [68]. The amount of each varies depending on the source, typically ranging from 20-25% amylose and 75-80% amylopectin [76], [78]. Amylose, a linear polymer made up of repeating glucose units with α -1,4 glycosidic linkages, is amorphous [76]. Amylopectin (AP), a crystalline and branched polymer, is also made up of repeating glucose units. The general form of amylopectin includes α -1,4 glycosidic bonds, as well as α -1,6 glycosidic linkages for branches occurring approximately after every 28-30 glucose units [76], [78]. Amylose is not soluble in water and highly prone to retrogradation due to its linearity, while branched amylopectin is largely soluble in water at high temperatures and has a lower retrogradation tendency.

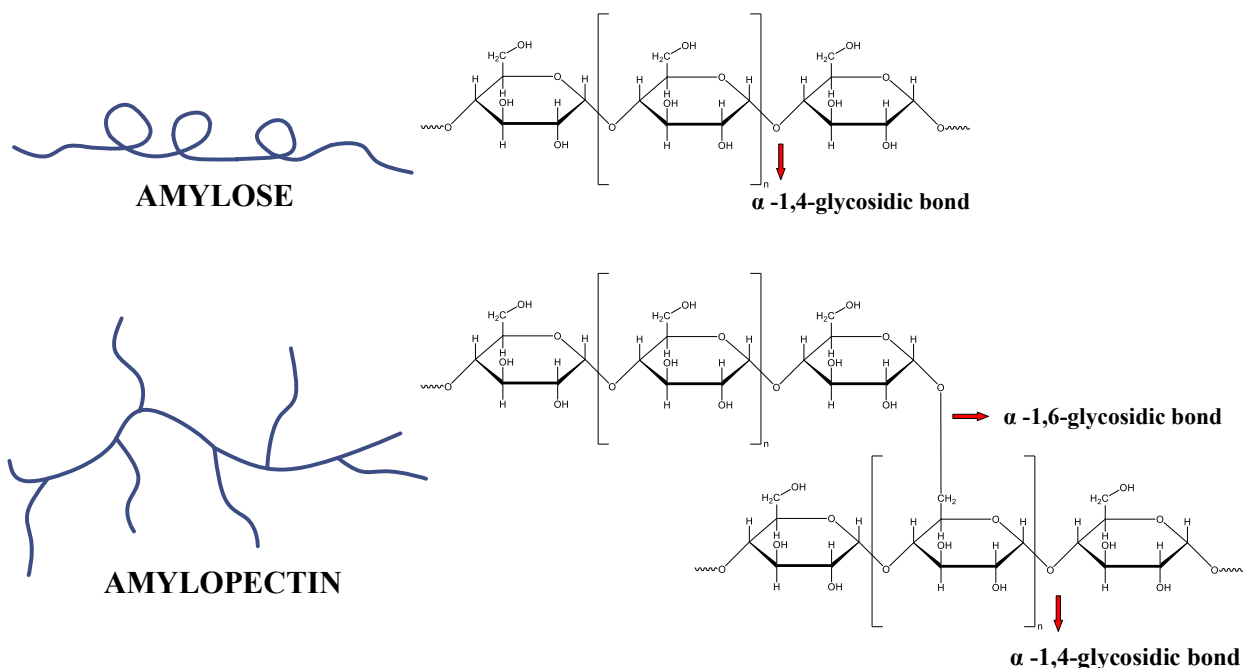


Figure 2.17: Amylose and amylopectin (redrawn from [79]).

In 1997, Rath and Singh compared the flocculation performance of starch, amylose, and amylopectin grafted with polyacrylamide (PAM) [71]. They reported that the amylopectin graft copolymers (AP-g-PAM) outperformed both the amylose and starch graft copolymers, which was attributed to the higher molecular weight and higher branching frequency of amylopectin [71]. Typically, the molecular weight of amylose (10,000-60,000 g/mol) is much lower than that of amylopectin (50,000-1,000,000 g/mol) [59], [63]. In addition, in amylopectin, the grafted chains are likely not only attached to the main backbone, as in the case of amylose, but also to the branches, which allows for more effective contact with solids in suspension during flocculation.

2.5.2 Amylopectin Graft Copolymers

Due to the superior flocculation performance of amylopectin graft copolymers, researchers have studied the effects of changing reaction conditions, as well as grafting different monomers to amylopectin for various applications. Table 2.1 summarizes the results published for amylopectin graft copolymers.

Rath and Singh (1997) compared the flocculation ability of various grades of AP-g-PAM [71]. They used a ceric-ion induced redox initiation method (CAN) and varied the amounts of monomer and catalyst to produce four different graft copolymers. The flocculation performance was determined using the jar test on a kaolin clay suspension. The best flocculant had fewer but longer grafted PAM chains [71]. In 1998, Rath and Singh continued their research by producing four more AP-g-PAMs (made with the same methodology) to further investigate the flocculation of a kaolin suspension and an industrial paper-mill white effluent [80]. The kaolin tests corroborated their previous findings, but not for the paper-mill effluent, showing that flocculation performance does not depend only on flocculant type but also on the nature of the colloidal system [80]. Similarly, Karmakar et al. (2002) applied polysaccharide-based graft copolymers to flocculate a chromite ore fines suspension [81]. They found out that amylopectin performed better than starch, sodium alginate, and carboxymethyl cellulose as a backbone, and that AP-g-PAM had the potential to treat effluents from chromite ore processing [81].

In another work, Singh et al. (2013) created novel amphoteric graft copolymer flocculants based on amylopectin [82]. In this study, AP-g-PAM was produced via the microwave-assisted method, followed by subsequent base hydrolysis (Hyd. AP-g-PAM) and cationization by either conventional or microwave-assisted methods to make it amphoteric (Amp. AP). Each of these polymers was tested for their flocculation performance on kaolin clay and iron ore suspensions, and also for their dye removal capacity. The results of all tests showed that Amp. AP performed better than the other polymers (Amp. AP > Hyd. AP-g-PAM > AP-g-PAM > AP) and that those made through microwave-assisted synthesis performed better than those made by the conventional method [82].

Kolya and Tripathy compared various polysaccharides grafted with PAM and poly(N,N-dimethylacrylamide) (PDMA) [83], [84]. In both studies, AP-g-PAM and AP-g-PDMA were synthesized using CAN and their flocculation abilities were tested. On all the tested colloidal suspensions, the graft copolymers with PDMA had a higher flocculation efficiency than those grafted with PAM and other tested commercial flocculants [83], [84]. The authors postulated that the PDMA grafts were more flexible than the PAM grafts since no intramolecular hydrogen bonding could occur. As a result of their higher flexibility, they could approach the colloidal

particles more easily. Furthermore, a biodegradation study revealed that both the AP-g-PAM and AP-g-PDMA were biodegradable and that they degraded more slowly than unaltered AP [84].

Around the same timeframe, Sarkar et al. synthesized amylopectin grafted with poly(acrylic acid) (AP-g-PAA) using potassium persulfate (KPS) as a free radical initiator [60], [85]. In their 2013 study, after producing the natural graft copolymers under optimum conditions, they tested their flocculation performance on different synthetic effluents (Fe-ore, Mn-ore, and kaolin) and mining industry wastewater. The AP-g-PAA was an effective flocculant and the best performing graft copolymer had the highest hydrodynamic radius and volume, giving credence to the Brostow, Pal and Singh model of flocculation [60]. In 2014, they evaluated the biodegradability of AP-g-PAA and its capacity to remove toxic malachite green dye. The study showed that the graft copolymer was indeed biodegradable, while its adsorption efficiency depended on a higher solution pH to produce more ionized groups to better attract the positively charged adsorbate [85].

Further studies have explored the effects of grafting more than one monomer onto the amylopectin backbone. In one investigation, Pal and Pal performed a two-step binary reaction using KPS as a free radical initiator to produce amylopectin grafted with poly(acrylamide) and later poly(acrylic acid) [(AP-g-PAM)-g-PAA] [86]. Standard jar and settling tests showed that the binary grafted products flocculated the Fe-ore suspension better than AP-g-PAM, because of its higher radius of gyration and molecular weight [86]. In another study, Adhikary and Krishnamoorthi synthesized amylopectin graft copolymers in a one-step process using CAN as the initiator and both acrylamide and 2-acrylamido-2-methylpropanesulfonic acid monomers [AP-g-p(AM-co-AMPS)] [87]. They observed that the products with the highest grafting efficiency and intrinsic viscosity had the best kaolin flocculation performance and Cu^{2+} metal ion absorption [87]. Kumar et al. synthesized novel cationic and amphoteric flocculants (AP-g-C and AP-AT-C) based on amylopectin with acrylamide and (3-acrylamidopropyl) triethylammonium chloride (ATMAC) monomers using an ammonium persulfate free radical initiator (APS) [88]. These polymers were used to flocculate a kaolin suspension, as well as to remove methylene blue dye from solution. Both showed promising results for future use. The cationic polymers appeared to favour the bridging mechanism while the amphoteric polymers flocculated mainly via electrostatic interactions [88]. However, as the electrostatic interactions within and between polymer chains increased, the degree of chain straightening and resulting performance decreased [88]. Sasmal et

al. synthesized amylopectin grafted copolymers through a KPS free radical polymerization with acrylamide and *N*-methylacrylamide [AP-*g*-poly(AM-*co*-NMA)] and studied its flocculation and biodegradation capabilities [89]. The product was partially biodegradable and in some of the solid suspensions tested, namely the iron ore slime and bentonite clay suspension, AP-*g*-poly(AM-*co*-NMA) showed better flocculation performance than AP-*g*-PAM and other commercial flocculants [89]. For the dye removal tests, the AP-*g*-poly(AM-*co*-NMA) had the highest decolourization efficiency [89]. It was suggested that the mixed grafted chains inhibited intramolecular hydrogen bonds to some extent and the presence of more polar -CONHMe groups enhanced the flocculation capabilities compared to less polar -CONH₂ groups exclusively in AP-*g*-PAM.

More recently, Sasmal et al. synthesized an efficient cadmium ion (Cd(II)) binder by grafting methyl acrylate (MA) onto amylopectin (AP-*g*-PMA) using a free radical KPS initiator, followed by partial alkaline hydrolysis (PHAP) [90]. PMA is a hydrophobic polymer and requires alkaline hydrolysis to make it water-soluble through the modification of methyl ester groups (-COOCH₃) to carboxylate groups (-COO⁻). In this study, it was shown that PHAP was biodegradable and effectively adsorbed Cd(II) ions through ionic interactions with the -COO⁻ groups of the graft copolymer [90]. Motta et al. (2019) also synthesized AP-*g*-PMA and solidification tests showed it could be used as an efficient oil spill control aid [91]. The biodegradability, adsorptive characteristics, and tailorable attributes of this natural graft copolymer make it a suitable candidate for use in MFT treatment. Therefore, it was the focus of this thesis work.

Table 2.1: Summary of published amylopectin graft copolymers used as flocculants.

Graft Copolymer	Flocculation Tests	Other Tests	Reference
AP-g-PAM	Jar Test: 0.25% kaolin clay suspension		[71]
AP-g-PAM	Jar Test: 0.25% w/v kaolin clay suspension Paper-mill white effluent		[80]
AP-g-PAM	Jar Test: 1 wt.% chromite ore fines suspension Settling Test: 10 wt.% chromite ore fines suspension		[81]
AP-g-PAM Hyd. AP-g-PAM Amp. AP	Column Sedimentation Test: 5 wt.% Fe-ore suspension 3 wt.% kaolin suspension	Methylene Blue Dye Removal: 0.001 wt.% dye solution	[82]
AP-g-PDMA AP-g-PAM	Jar Test: 1 wt.% kaolin clay suspension 0.25 wt. % iron ore slime		[83]
AP-g-PAM AP-g-PDMA	Jar Test: 1 wt.% coal suspension 1 wt.% silica suspension Settling Test: Fe-ore suspension Kaolin suspension Mn-ore suspension	Biodegradation Study: Enzyme hydrolysis	[84]
AP-g-PAA	Fe-ore suspension Kaolin suspension Mn-ore suspension	Pollutant Load & Colour Removal: Mining Industry Wastewater	[60]
AP-g-PAA		Biodegradation Study: with <i>Aspergillus niger</i> fungus Adsorption/Desorption Study: Malachite green dye solution	[85]
(AP-g-PAM)-g-PAA	Jar Test: 0.25 wt.% iron ore suspension Settling Test: 5 wt.% iron ore suspension		[86]
Ap-g-p(AM-co-AMPS)	Jar Test: 1 % kaolin suspension	Absorption Study: Cu ²⁺ metal ion solution	[87]
AP-g-C AP-AT-C	Jar Test & Settling Test: kaolin suspension	Methylene Blue Dye Removal: Column filtration 0.025 mg/mL dye solution Dye removal kinetics 0.001 mg/mL dye solution	[88]
AP-g-poly(AM-co-NMA)	Jar Test: 1 wt.% coal suspension 1 wt.% silica suspension 1 wt.% kaolin clay suspension 0.25 wt.% iron ore slime 1 wt.% bentonite clay suspension	Biodegradation Study: Enzyme hydrolysis Colour removal Study: Malachite green solution	[89]
AP-g-PMA PHAP		Biodegradation Study: with <i>Fusarium</i> sp fungal mycelia Adsorption & Desorption Study: 0.01 mol/L Cd(II) ion solution	[90]
AP-g-PMA		Solidification Studies: Crude oil Diluted bitumen Diesel	[91]

These previous publications have confirmed that amylopectin is an effective backbone for natural graft copolymer flocculants and that these flocculants can outperform some commercial products. These studies have further shown that the optimal performance of these polymers depends on the synthesis conditions, type of monomer grafted, and the application medium. Nonetheless, these polymers are typically tested on synthetically created effluents, and subsequently may perform differently for industrial wastewaters, like MFT, that contain many different chemical species.

Previous investigations in our group have examined some natural graft copolymers, such as AP-*g*-PAM and chitosan-based flocculants, for the treatment of oil sands MFT with promising results [92]–[94]. In these works, however, PAM was the grafted synthetic polymer. Even though it is commonly used for the treatment of MFT, PAM has limitations associated with its high hydrophilicity. Such limitations include its inability to adsorb onto bitumen and organic coatings that can be found on MFT clay surfaces, as well as its hydrogen bonding capacity that creates low-density flocs due to water retention [53]. The incorporation of non-hydrogen bonding moieties, as well as some ionic groups in the grafts, may greatly improve the effectiveness of AP graft copolymers. Therefore, the main objectives of this thesis were to synthesize and characterize amylopectin-*graft*-hydrolyzed-poly(methyl acrylate) copolymers (AP-*g*-H-PMA) and use these products to flocculate MFT from Alberta's oil sands, which is a novel application for this flocculant.

3. Materials and Methods

3.1 Materials

Powdered amylopectin from maize (AP), methyl acrylate monomer (MA) (99%), potassium persulfate free radical initiator (KPS) ($\geq 99\%$), sodium hydroxide pellets (NaOH) ($\geq 98\%$), methanol ($\geq 99.9\%$), and acetone ($\geq 99.5\%$) were purchased from Sigma-Aldrich. Hydrochloric acid (HCl) was bought from Thermo Fisher Scientific. The commercial anionic polyacrylamide (A-PAM) used as a reference flocculant had approximately 30% anionic charge density ($M_w > 10,000,000$ g/mol). All required MFT suspensions were prepared using deionized water (DI).

3.2 Production of Amylopectin Graft Copolymer Flocculants

3.2.1 Synthesis of Amylopectin-*graft*-poly(methyl acrylate) (AP-*g*-PMA)

The synthesis procedure followed the method outlined by Sasmal et al. (2016) with some notable modifications [90]. Firstly, the desired amount of AP was mixed with DI water in a 250 mL Erlenmeyer flask fitted with a magnetic stir bar. The mixture was stirred at 300 rpm and heated to dissolution for 25 minutes at approximately 90 °C in an oil bath (until the solution became more transparent). A Vigreux condenser column was used to prevent any loss of solution. This process is known as gelatinization. Amylopectin is insoluble in cold water but generally becomes soluble when mixed at higher temperatures [78]. Following this dissolution step, the temperature of the solution was reduced to 70 °C, the flask was sealed with a rubber septum, and the solution was set to mix at 300 rpm. The solution was then purged with nitrogen for 1 hour to remove any oxygen. During this time, a stock KPS initiator solution was prepared by dissolving the required mass in DI water and purged with nitrogen for 15 minutes. After purging the AP solution for 1 hour, 2 mL of the initiator solution was added using a syringe needle. As KPS decomposes at temperatures above 50 °C, radicals were formed which could abstract hydrogen atoms from the AP backbone, leading to the formation of active sites (macroradicals) where the graft copolymerization could then occur [77]. The solution was then left to mix for 20 minutes under nitrogen purge to give

ample pre-interaction time for the backbone and initiator to form macroradicals. During this period, the MA monomer was purged with nitrogen. After purging, the desired amount of MA was added to the solution using a syringe needle. The purge was then stopped, and the reaction flask was sealed. The reaction mixture was kept stirring at a constant rate (300 rpm) for 4 hours. The reaction was stopped by exposing it to air, cooling it, precipitating the crude product in excess methanol, and washing it overnight in excess methanol and water (3:2 by volume) to remove any unreacted monomer. The product was filtered, and rinsed multiple times with DI water, and freeze-dried. The proposed chemical reaction scheme is depicted in Figure 3.1 [95].

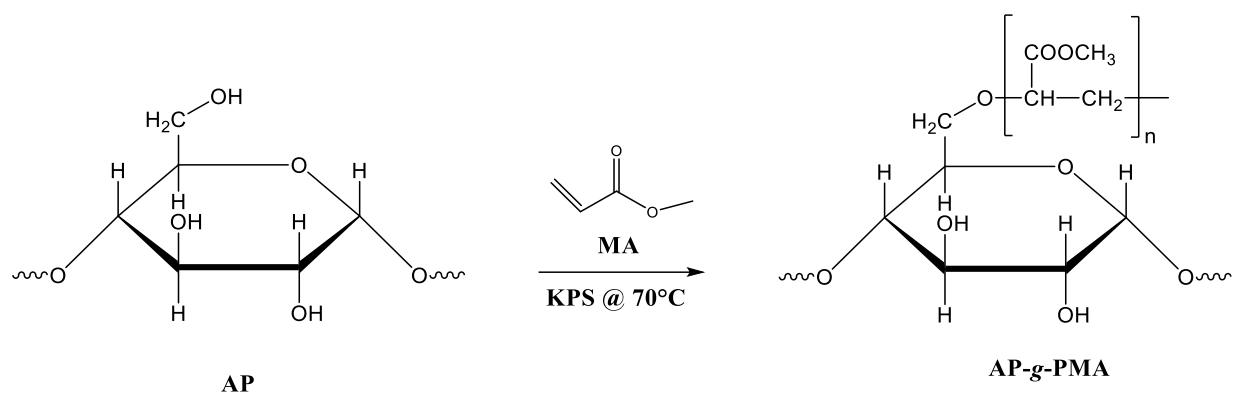


Figure 3.1: Chemical reaction scheme for amylopectin-*graft*-poly(methyl acrylate) (AP-g-PMA).

3.2.2 AP-g-PMA Purification

The crude product containing the graft copolymer (AP-g-PMA) and homopolymer (PMA) was then further purified to remove the PMA. This was done via Soxhlet extraction with acetone [96]–[99]. Figure 3.2 depicts a typical Soxhlet extraction apparatus. For this purification, a small portion of the crude product (~ 3 g) was weighed and transferred into a cellulose extraction thimble (1 mm wall thickness). The thimble was then inserted into the Soxhlet apparatus and the system was refluxed for 72 hours to ensure the purity of the final product. The graft copolymer was then dried and weighed. It should be noted that purification studies were performed to determine the required extraction time and effectiveness of the acetone separation procedure (see Appendix A).

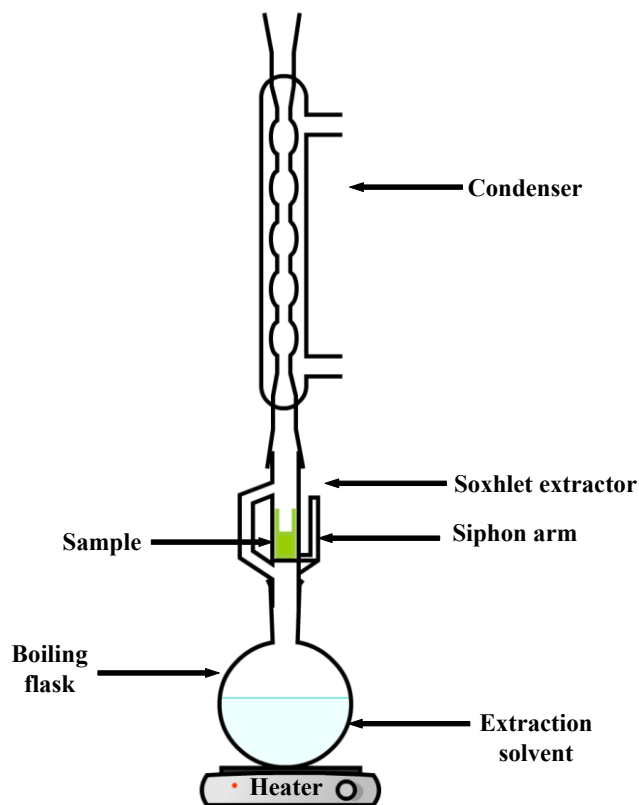


Figure 3.2: Soxhlet extraction apparatus.

3.2.3 Grafting Parameters

In previous natural graft copolymerization studies, it has been observed that changes in the reaction variables impacted the grafting parameters and flocculation efficacy of the resulting polymers [60], [100]. In this work, the grafting parameters, including monomer conversion, grafting efficiency, homopolymerization (PMA homopolymer fraction), grafting ratio, add-on % (PMA wt.%), and AP wt.% were calculated after purification using Equations (3.1) to (3.6) [68], [76]:

$$\text{Monomer Conversion (\%)} = \frac{\text{wt. of PMA grafted chains} + \text{wt. of PMA homopolymer}}{\text{wt. of MA monomer initially}} \times 100\% \quad (3.1)$$

$$\text{Grafting Efficiency (\%)} = \frac{\text{wt. of PMA grafted chains}}{\text{wt. of PMA grafted chains} + \text{wt. of PMA homopolymer}} \times 100\% \quad (3.2a)$$

or

$$\text{Grafting Efficiency (\%)} = \frac{\text{wt. of PMA grafted chains}}{\text{wt. of MA monomer initially}} \times 100\% \quad (3.2b)$$

$$\text{Homopolymerization (\%)} = \frac{\text{wt. of PMA homopolymer}}{\text{wt. of PMA grafted chains} + \text{wt. of PMA homopolymer}} \times 100\% \quad (3.3a)$$

or

$$\text{Homopolymerization (\%)} = \frac{\text{wt. of PMA homopolymer}}{\text{wt. of MA monomer initially}} \times 100\% \quad (3.3b)$$

$$\text{Grafting Ratio} = \frac{\text{wt. of PMA grafted chains}}{\text{wt. of AP backbone}} \quad (3.4)$$

$$\text{Add-on (\%)} \text{ (or PMA wt. \%)} = \frac{\text{wt. of PMA grafted chains}}{\text{wt. of graft copolymer}} \times 100\% \quad (3.5)$$

$$\text{AP wt. \%} = \frac{\text{wt. of AP backbone}}{\text{wt. of graft copolymer}} \times 100\% \quad (3.6)$$

Even though the formulae for homopolymerization (PMA homopolymer fraction) and grafting efficiency have been presented in the literature in different ways, Equations (3.2b) and (3.3b) were used in this work. The equations chosen are based on the amount of monomer initially charged to the polymerization. As MA homopolymerization is an unwanted side reaction, it was not considered in the efficiency calculation.

3.2.4 Alkaline Hydrolysis (AP-g-H-PMA)

As the purified graft copolymers were not soluble in water, an alkaline hydrolysis step was performed to convert the methyl groups in the PMA grafted chains to carboxylates, as shown in Figure 3.3. A small portion of the purified graft copolymer (0.5 g) was weighed and transferred into a 250 mL round bottom flask. A 100 mL alkaline solution (0.5 M) was prepared with the

required amount of sodium hydroxide (NaOH) pellets dissolved in DI water. The solution was then transferred into the flask, fitted with a magnetic stir bar, and placed in an oil bath at 75 °C. A Vigreux condenser column was fitted to the flask to prevent evaporation. The solution was set to mix at 250 rpm for 24 hours until the polymer was completely soluble in the basic solution. At this point, the solution was cooled to room temperature and neutralized to a weak alkaline condition (pH = 9) with a 1 M hydrochloric acid (HCl) solution. The polymer was precipitated in excess methanol and washed overnight in a mixture of methanol and water (3:2 by volume). The polymer was then filtered, rinsed, dissolved in DI water, and freeze-dried. Figure 3.4 outlines the entire synthesis process including the graft copolymerization, purification, and alkaline hydrolysis.

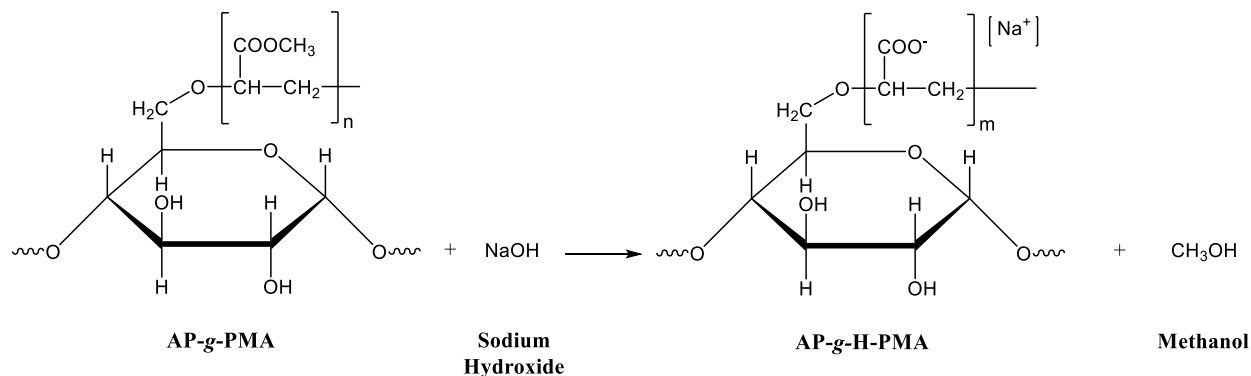


Figure 3.3: Alkaline hydrolysis reaction scheme of amylopectin-*graft*-poly(methyl acrylate) (AP-g-PMA) to amylopectin-*graft*-hydrolyzed-poly(methyl acrylate) (AP-g-H-PMA).

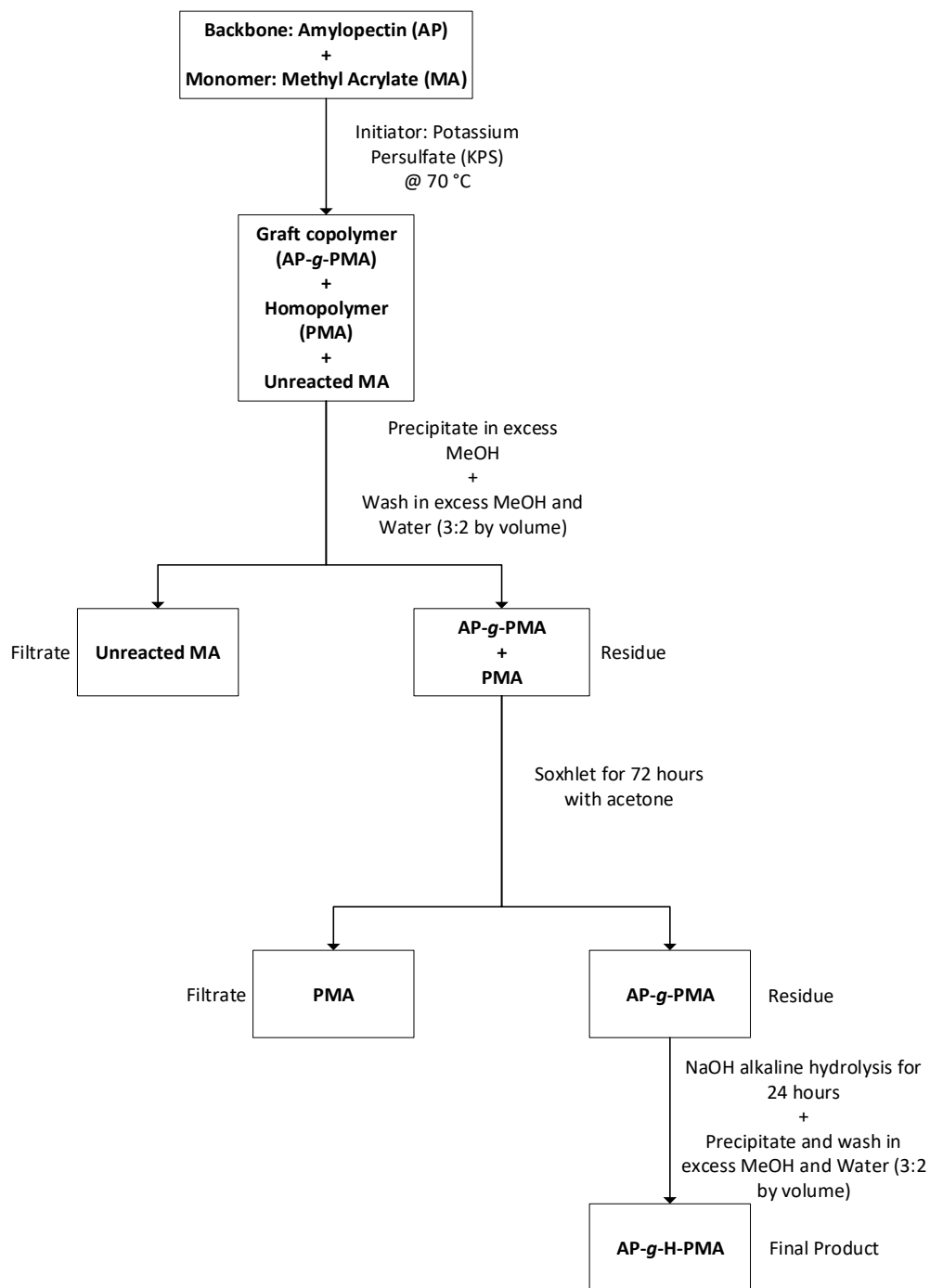


Figure 3.4: Amylopectin-*graft*-hydrolyzed-poly(methyl acrylate) (AP-g-H-PMA) synthesis overview.

3.2.5 Central Composite Design of Experiments

In this work, a rotatable central composite experimental design (CCD) was used to analyze how different grades of the graft copolymer affected MFT flocculation. This type of experimental design was proposed by Box and Wilson in 1951 [101]. Generally, the design includes a fractional or full factorial design, a star design with experimental points located α distance from the centre, and a centre point $(-\alpha, -1, 0, +1, +\alpha)$ [102], [103]. This statistical tool can fit second-order polynomial equations, Equation (3.7), and generate predictive response surfaces [103]. In this second-order model, Y represents the responses, ϵ is the error term, β_0 is the intercept, k is the number of factors, X_i and X_j are the coded levels for the independent variables, and β_i , β_{ii} , and β_{ij} represent coefficient values for the linear, quadratic, and interaction effects, respectively [103], [104].

$$Y = \beta_0 + \sum_{i=1}^k \beta_i X_i + \sum_{i=1}^k \beta_{ii} X_i^2 + \sum \sum_{i < j} \beta_{ij} X_i X_j + \epsilon \quad (3.7)$$

The required number of experiments for the design is determined using Equation (3.8) [102]. In this equation, N is the total number of experiments with k independent factors and c_p is the number of centre point replicates.

$$N = k^2 + 2k + c_p \quad (3.8)$$

Further, for the case of a CCD including a full factorial design, the value of the axial points, α , can be calculated with Equation (3.9) [102].

$$\alpha = 2^{\frac{k}{4}} \quad (3.9)$$

In this study, three independent variables ($k = 3$) were altered including: 1) monomer molar concentration $[M]$, 2) backbone molar concentration $[B]$, and 3) flocculant dosage. As 3 factors were altered in this design, the computed value of α was 1.682. In the design, 15 unique combinations were made from the five-level coded values associated with each independent variable, as shown in Table 3.1. The design, therefore, consisted of eight cube points, six axial points, and a centre point. Additionally, the centre point was repeated twice ($c_p = 2$) for a total of

17 runs. A replicate of each of the flocculation tests was also planned to ensure the results were reproducible.

Table 3.1: Central composite design (CCD) independent variables and their level values.

Independent variables	Variable levels				
	-1.682	-1	0	+1	+1.682
X_1 : [M] (mol/L)	0.207	0.275	0.375	0.475	0.543
X_2 : [B] (AGU mol/L)	0.033	0.050	0.075	0.100	0.117
X_3 : Polymer dosage (kppm)*	0.636	2.000	4.000	6.000	7.364

* kilo parts per million (kppm)

The results of the design were analyzed using a response surface regression method (Tibco Statistica 13.3, Ultimate Academic Bundle). In this program, significant effects were identified, multiple regression analysis of the model was performed, and response surface plots were constructed.

Several grades of the graft copolymer were produced based on the output of the CCD which varied the three main factors. In each reaction, the concentration of initiator [I] was kept constant at 2.5×10^{-4} M. By changing the amount of monomer used in the polymerization from 0.207 to 0.543 M, the monomer to initiator molar ratio ($[M]/[I]$) changed. This was done to vary the length of the grafted PMA chains, as a low $[M]/[I]$ typically produces shorter chains (on average), while a high $[M]/[I]$ makes longer chains. The range of monomer concentrations chosen was kept under the solubility limit of MA in water (~ 5 g/100 mL) [105]. As the molecular weight of amylopectin may vary greatly, the backbone amounts were expressed in terms of anhydroglucose units (AGU) (molecular weight = 162.14 g/mol) [106]. In this study, the concentration of AGU was varied from 0.033 to 0.117 M. The range of backbone concentrations was chosen based on viscosity limitations noted in the literature [84]. By varying the backbone to initiator molar ratio ($[B]/[I]$), the frequency of the PMA grafts was adjusted. It is expected that a low $[B]/[I]$ results in a more densely grafted copolymer (high frequency), while a high $[B]/[I]$ should result in less dense grafting (low frequency). Furthermore, different dosages of the graft copolymers were tested, from 0.636 to 7.364 kppm, to find out how flocculants with different microstructures affected the performance

over a range of dosages. The polymerization conditions were kept constant in each run and the total volume for each reaction was 200 mL. A total of 11 polymers were produced, as summarized in Table 3.2. Each purified polymer was initially coded with the notation “GP#” representing the purified graft copolymer followed by the reaction run number. After hydrolysis, an “H” was introduced as the first character. When tested for flocculation, the characters following the hyphen signify the dosage tested. Therefore, sample HGP1-2k is a hydrolyzed AP-g-PMA sample made in reaction 1 and tested at a concentration of 2,000 ppm.

Table 3.2: Summary of the 3-factor central composite design (CCD).

Run (AP-g-PMA)	Hydrolyzed Polymer (AP-g-H-PMA)	[I] (mol/L)	[M] (mol/L)	[B] (mol AGU/L)	Dosage (kppm)	[M]/[I]	[B]/[I]
GP1	HGP1-2k	2.5E-4	0.275 (-1)	0.050 (-1)	2.000 (-1)	1100	200
	HGP1-6k	2.5E-4	0.275 (-1)	0.050 (-1)	6.000 (+1)	1100	200
GP2	HGP2-2k	2.5E-4	0.475 (+1)	0.050 (-1)	2.000 (-1)	1900	200
	HGP2-6k	2.5E-4	0.475 (+1)	0.050 (-1)	6.000 (+1)	1900	200
GP3	HGP3-2k	2.5E-4	0.275 (-1)	0.100 (+1)	2.000 (-1)	1100	400
	HGP3-6k	2.5E-4	0.275 (-1)	0.100 (+1)	6.000 (+1)	1100	400
GP4	HGP4-2k	2.5E-4	0.475 (+1)	0.100 (+1)	2.000 (-1)	1900	400
	HGP4-6k	2.5E-4	0.475 (+1)	0.100 (+1)	6.000 (+1)	1900	400
GP5	HGP5-4k	2.5E-4	0.375 (0)	0.033 (- α)	4.000 (0)	1500	132
GP6	HGP6-4k	2.5E-4	0.375 (0)	0.117 (+ α)	4.000 (0)	1500	468
GP7	HGP7-4k	2.5E-4	0.207 (- α)	0.075 (0)	4.000 (0)	827	300
GP8	HGP8-4k	2.5E-4	0.543 (+ α)	0.075 (0)	4.000 (0)	2173	300
	HGP9-0.6k	2.5E-4	0.375 (0)	0.075 (0)	0.636 (- α)	1500	300
GP9	HGP9-7k	2.5E-4	0.375 (0)	0.075 (0)	7.364 (+ α)	1500	300
(C)*	HGP9-4k	2.5E-4	0.375 (0)	0.075 (0)	4.000 (0)	1500	300
GP10 (C)*	HGP10-4k	2.5E-4	0.375 (0)	0.075 (0)	4.000 (0)	1500	300
GP11 (C)*	HGP11-4k	2.5E-4	0.375 (0)	0.075 (0)	4.000 (0)	1500	300

* Centre point runs (C)

An MA homopolymerization was also performed following the same procedure and using the same concentrations ($[M]/[I]$) as the AP-g-PMA centre points (GP9, GP10, and GP11), without the addition of the AP backbone. This polymer was prepared as a reference to compare its

performance to the graft copolymers. An AP-PMA blend was also prepared with a comparable composition to the centre point of the AP-g-PMA experimental design (40 wt.% AP and 60 wt.% PMA) for characterization comparisons. The required amount of each polymer was weighed out, dissolved in dimethyl sulfoxide (DMSO), and set to mix at 300 rpm. To ensure the AP and PMA were fully dissolved the mixture was heated in an oil bath at 70 °C for 1 hour. After dissolution, the blend was precipitated and washed in excess methanol, filtered, and dried to a constant weight.

3.3 Proof of Grafting and Flocculant Characterization

3.3.1 Fourier-Transform Infrared Spectroscopy (FTIR)

An Agilent Technologies Cary 600 Series Fourier transform infrared (FTIR) spectrometer was used to determine key functional groups in the tested samples. The attenuated total reflectance (ATR) technique was used for the spectral analysis and each sample was scanned with 30 runs. The FTIR system analyzed the samples with infrared light to produce an absorbance spectra in the mid-IR region from about 4000-666 cm^{-1} [107]. Considerable differences exist between the spectra of AP, PMA, and AP-g-PMA, which help to indicate if the grafting was successful.

Table 3.3 lists the 7 samples analyzed, as well as the 3 analyses performed: 1) identification of key functional groups and differences between the homopolymers and the graft copolymer, 2) comparison of the AP-PMA blend, crude graft copolymer, and purified graft copolymer, and 3) comparison before and after alkaline hydrolysis.

Table 3.3: FTIR analysis summary.

Sample	Analyses
AP	1
PMA	1
AP-PMA blend	2
Crude GP11	2
GP11	1,2
GP3	3
HGP3	3

3.3.2 Nuclear Magnetic Resonance Spectroscopy (NMR)

Nuclear magnetic resonance spectroscopy (NMR) was performed to further characterize the samples using an Agilent/Varian Inova three-channel 400 MHz spectrometer. The samples were analyzed using a one-dimensional technique to identify key properties of the chemical structure.

All samples were first dissolved in the appropriate deuterated solvent, then proton (^1H) and carbon (^{13}C) NMR testing were performed on each sample at 27 °C. Table 3.4 summarizes the samples analyzed and conditions used for the NMR testing.

Table 3.4: NMR analysis summary.

Sample	Solvent	Analyses
AP	DMSO- d_6	^1H , ^{13}C
PMA	DMSO- d_6	^1H , ^{13}C
AP-PMA blend	DMSO- d_6	^1H , ^{13}C
GP10	DMSO- d_6	^1H , ^{13}C

3.3.3 Helium-ion Microscopy (HiM)

A Zeiss Orion Nanofab helium-ion microscope (HiM) was used to analyze the surface morphological differences between the samples. Unlike a scanning electron microscope (SEM),

the HiM does not require the samples to be sputter-coated with a conductive material, such as gold; as a result, more accurate images can be taken of the polymer surface morphology. Table 3.5 lists the samples and the field of view examined with the instrument.

Table 3.5: HiM analysis summary.

Sample	Description	Field of View
AP	Before gelatinization	50 μm & 10 μm
AP	After gelatinization	50 μm & 10 μm
PMA	Homopolymer	50 μm & 10 μm
AP-PMA	Blend	50 μm & 10 μm
GP10	Purified AP-g-PMA	50 μm & 10 μm

3.3.4 Thermogravimetric Analysis (TGA)

A thermal analysis was performed using a Thermal Gravimetric Analyzer (TGA) to identify changes in sample weight as the temperature was gradually increased. The instrument used was a Thermax 300 Thermo Cahn analyzer. The testing was performed from approximately 25 °C to 600 °C, in an inert argon atmosphere with a flow rate of 50 mL/min, using a uniform heating rate of 10 °C/min for all cases.

Table 3.6 summarizes the samples tested with this instrument and the 2 analyses performed: 1) analysis of weight-loss trends of the homopolymers, graft copolymer, and the AP-PMA blend, and 2) analysis of various grades of AP-g-PMA.

Table 3.6: TGA analysis summary.

Sample	Analyses
AP	1
PMA	1
AP-PMA blend	1
GP9	1,2
GP5	2
GP6	2
GP7	2
GP8	2

3.3.5 Field Flow Fractionation (FFF)

Molecular weight distribution results for the AP-g-H-PMA graft copolymers were obtained using a Postnova AF2000 Flow Field Flow Fractionation (FFF) instrument. Each sample was dissolved at a concentration of 3 mg/mL and sonicated for about three minutes prior to injection.

3.4 MFT Characterization

3.4.1 Dean-Stark Extraction

A Dean-Stark apparatus was used to determine the composition (amount of water, residual bitumen, and solids present) in the MFT sample used for testing. The extraction apparatus consisted of a long neck round bottom flask, a reflux condenser, and a trap [25], [108]. In this analysis, 100 g of MFT was weighed into an extraction thimble while approximately 250 mL of toluene was transferred into the round bottom flask. The thimble was then hung in the neck portion of the flask and the rest of the apparatus was assembled. The temperature of the system was adjusted above the boiling point of toluene ($> 111\text{ }^{\circ}\text{C}$) to allow the system to be refluxed. When the desired temperature was reached, the toluene evaporated, passing through the thimble and in turn, evaporating the water in the MFT sample. The vapours rose to the condenser where they cooled, condensed, and dropped into the trap. As toluene and water are immiscible, the condensed

liquid separated into two layers with the toluene as the less dense top layer and water as the denser bottom layer. This separation allowed only the water to be drained from the system. Over time, the rising level in the trap caused the toluene to overflow and drop back down through the MFT sample, in turn dissolving the bitumen as it returned to the flask. The system was left to reflux until the water level stabilized and the toluene dripping down from the thimble was colourless. At this point, the remaining water was extracted from the trap, the solids were dried in a vacuum oven, and each component was weighed. The mass of bitumen was also calculated by evaporating the toluene in the toluene-bitumen mixture. This extraction was then repeated on a new sample to ensure the accuracy of the results.

3.4.2 Solids and Moisture Analysis

An MB45 moisture analyzer was used to further quantify the solids and moisture percentage in the MFT sample. For the analysis, a small amount of sample (~ 1 g) was weighed on an aluminium pan and the temperature was raised to evaporate the moisture in the sample until the dry solids weight remained constant. This test was performed twice, and the average of the results was recorded.

3.4.3 Particle Size Distribution (PSD)

The particle size distributions (PSD), including the number and volume distributions, of the MFT sample were computed using a Malvern Mastersizer 3000. Two runs were performed on the sample (before and after sonication) consisting of five measurements per run.

3.4.4 Atomic Absorption Spectrophotometry (AAS)

The major ion concentrations for the MFT sample were determined via atomic absorption spectrophotometry (AAS). For this analysis, an MFT sample was centrifuged to separate the solids from the process water and the supernatant was subsequently collected. A VARIAN 220FS Atomic

Absorption Spectrophotometer was then used to measure the ion composition of the process water in the MFT sample.

3.5 MFT Flocculation and Dewatering Tests

3.5.1 Benchtop Mixing

The flocculation and dewatering experiments were performed via a benchtop method, where the MFT was first diluted with deionized (DI) water to 10 wt.% solids in a 250 mL glass beaker. The dosages used for the experiments were determined on a weight basis relative to the MFT solids (mg polymer per kg MFT solids). The concentration of the polymer solution (~ 3.3 mg/mL) was not changed while the dose was varied, therefore, the dilution of the MFT was also based on the polymer dosage used. As the volume of each experiment was maintained at 100 mL, the higher the polymer dose required, the less DI water was initially added to the MFT. A Heidolph Hei-Torque Precision 200 Overhead Stirrer and a four-blade impeller were used to mix the suspension. Firstly, the diluted mixture was initially stirred for 1 minute at 600 rpm then for 1 minute at 300 rpm to ensure a homogenized sample. Next, the flocculant was injected into the mixing stream and the sample was stirred for 10 seconds. As positively charged ions are necessary to bridge the negatively charged clay particles to the anionic polymer, 1500 ppm of calcium ions from a stock 1 M calcium chloride solution was added to the sample. The whole suspension was further mixed for 50 more seconds, totaling 1 minute of mixing. Flocculation metrics on the slurry were performed immediately following the mixing. Figure 3.5 depicts the general benchtop setup.

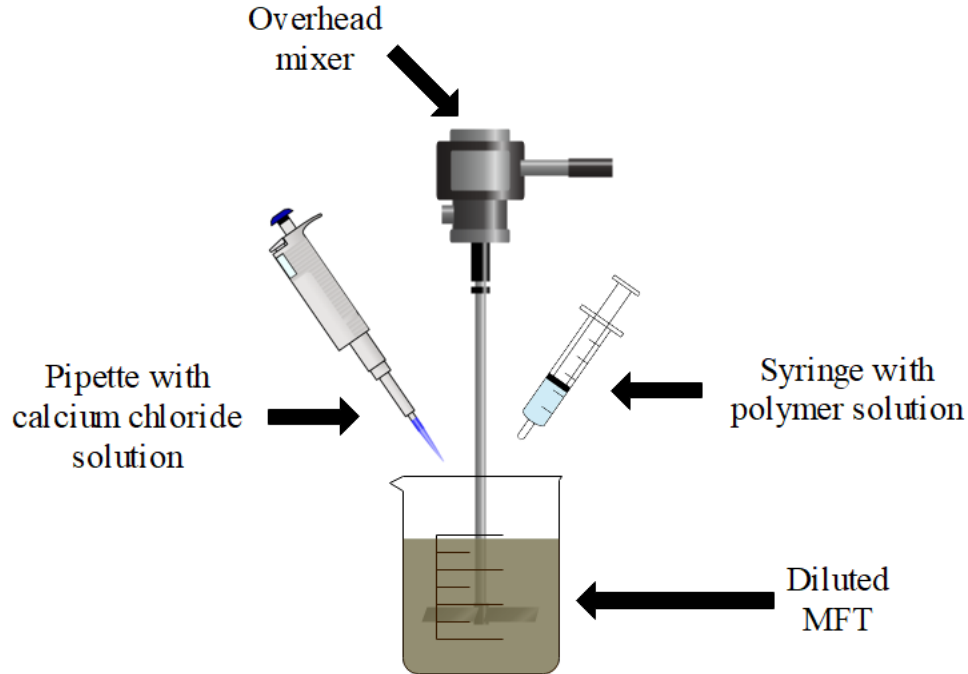


Figure 3.5: Diagram of a typical benchtop flocculation setup.

3.5.2 Capillary Suction Time (CST)

Capillary suction time (CST) was used to measure dewatering of the initial floc slurry as well as the settled solids after a 24-hour period. A Triton Electronics Meter (Type 319 multipurpose CST) instrument and standard (7 cm by 9 cm) Triton filter paper were used for this test. A schematic of the CST apparatus is presented in Figure 3.6. The analysis was performed using 5 mL of sample poured into the small cylinder which was secured on the filter paper. The CST is a measurement of the time taken for the sediments to dewater and for this expelled water to travel via capillary action concentrically from one electrode to another using filter paper as the medium [109]. The less time that is taken for this to occur, the better the dewaterability of the sample. The test was repeated three times to ensure reproducibility and the average time and standard error of the mean were calculated.

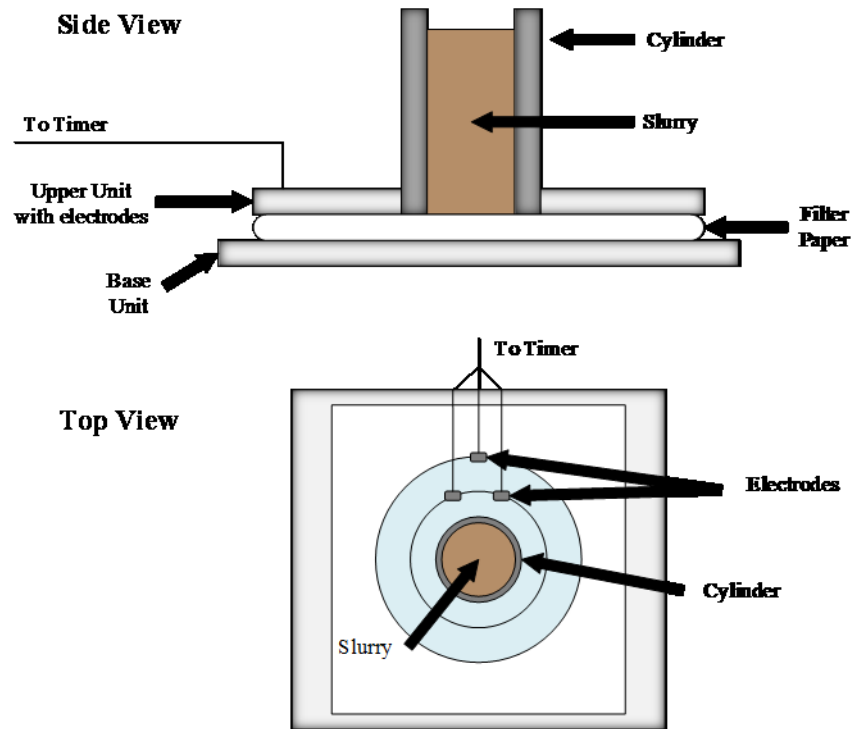


Figure 3.6: CST apparatus (redrawn from [110]).

3.5.3 Initial Settling Rate (ISR)

Initial settling rate (ISR) experiments were performed by first transferring the remaining slurry into a 100 mL graduated cylinder. The cylinder was sealed, and the flocs were then allowed to settle under gravity. The descending mudline height (height of the solid-liquid interface) was measured for the first hour of settling using a stopwatch. This is represented as a schematic in Figure 3.7. The ISR was then calculated from the slope of the linear portion of the mudline height versus time settling curve. The slurry was then left to consolidate in the cylinder for 24 hours.

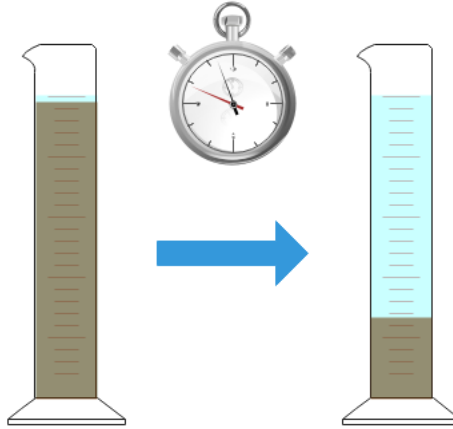


Figure 3.7: Graphic image of the graduated cylinder initially and after settling.

3.5.4 Supernatant Turbidity

After settling for 24 hours, the supernatant was separated from the sediment, and the interfacial material was thrown away. The turbidity was then measured using a Hach 2100AN Laboratory Turbidity Meter. This test was performed to determine the quality of the water released from the flocs. The more suspended particles present in the sample (low transparency), the higher the measured turbidity reading given in nephelometric turbidity units (NTU) (Figure 3.8). In industry, low turbidity (high transparency) is desirable, as cleaner recycled water will have less of an impact on the efficiency of bitumen extraction, as well as on the process equipment.

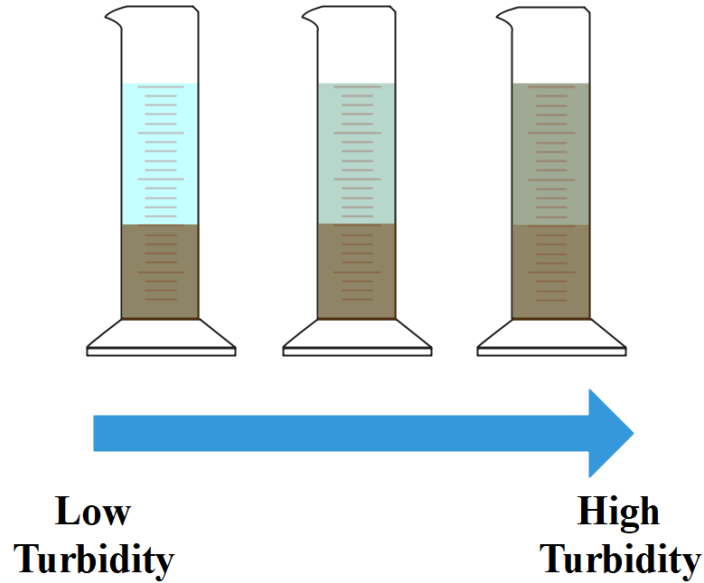


Figure 3.8: Visual representation of a range of supernatant turbidity.

3.5.5 Solids Content

The evaluation of the solids content measured the amount of compactness that the sample was able to achieve, as well as the amount of water that was trapped within the flocs. For this test, containers made from aluminium foil were first created and weighed. Next, 3 mL of the wet settled sample was extracted, placed into the container, and again weighed before drying. Sample drying was expedited using a vacuum oven at 50 °C for 24 hours. After the samples were dried, the foil containers holding the dry solids were weighed once more. The solids content was calculated using a ratio of the dry sample weight to the wet sample weight, as expressed by Equation (3.10) [25]. To calculate the average and standard error of the mean, three measurements were performed for each sample.

$$\text{Solids Content (\%)} = \frac{\text{dry weight} - \text{foil weight}}{\text{wet weight} - \text{foil weight}} \times 100\% \quad (3.10)$$

3.6 Comparison Testing

3.6.1 Benchtop Flocculation Comparison Tests

Benchtop flocculation tests were also performed for a commercial A-PAM, AP, H-PMA, and an AP and H-PMA blend (35% and 65% by weight, respectively) to compare their performance with that of the AP-g-H-PMA graft copolymer (HGP11). The H-PMA used in these tests was synthesized with the same $[M]/[I]$ as HGP11. Crude HGP11 was also tested to observe if the purification step is important in the resulting performance. It should be noted that the optimal mixing regime for A-PAM was not the same as for the other polymers. For A-PAM, after homogenization of the diluted MFT, the mixing speed was increased to 650 rpm and calcium was added. After allowing the calcium ions to mix for 30 seconds, the A-PAM was added and mixed for 2 minutes at this speed, followed by slow mixing at 230 rpm for 8 minutes [53], [108]. A series of dosages (500, 1000, 2000, 4000, 6000, and 9000 ppm) were tested for each polymer and the ISR, initial CST, sediment CST, supernatant turbidity, and solids content were compared. The experiments were all performed using MFT suspensions diluted to 10 wt.% solids. A blank test was also performed where only 1500 ppm of calcium ions were added to the MFT suspension to test whether the polymers truly made a difference in the settling and dewatering processes.

4. Results and Discussion

4.1 Synthesis of Amylopectin Grafted with Poly(methyl acrylate) (AP-g-PMA)

4.1.1 Proposed Graft Copolymerization Mechanism

A possible scheme for the mechanism of the free radical graft copolymerization of AP, KPS, and MA, as proposed in the literature for similar reactions, is shown in Table 4.1 [60], [90], [96], [111].

Table 4.1: Proposed graft copolymerization reaction scheme.

Initiation	$K_2S_2O_8 \rightarrow 2K^+ + 2SO_4^{2-} \rightarrow 2SO_4^{\cdot -}$
	$AP-OH + SO_4^{\cdot -} \rightarrow AP-O^{\cdot} + HSO_4^-$
	$M + SO_4^{\cdot -} \rightarrow M^{\cdot}$
Propagation	$AP-O^{\cdot} + M \rightarrow AP-O-M^{\cdot}$
	$AP-O-M^{\cdot} + nM \rightarrow AP-O-(M)_n-M^{\cdot}$
	$M^{\cdot} + nM \rightarrow (M)_n-M^{\cdot}$
Termination	by coupling with an initiator radical
	by combination
	by disproportionation
	↓
AP-g-PMA (graft copolymer) or PMA (homopolymer)	

Here, AP-OH represents the reactive hydroxyl group in the AP backbone, M is the MA monomer, AP-O \cdot and M \cdot are polymer radicals, and the subscript n is the length of the polymer radical. It is important to note that the two propagation reactions that occur in parallel may either form AP-g-PMA graft copolymers or the undesirable PMA homopolymer. Since it has previously

been reported in the literature that a prolonged pre-interaction time between the backbone and the initiator leads to more efficient grafting, the side reaction that formed PMA homopolymer was limited by using a long pre-interacting time (20 minutes) in this study [96].

4.1.2 Synthesis Results

Many previous investigations have studied the effect of reaction variables on the grafting efficiency for different graft copolymer systems. These studies, however, were conducted by varying only one variable at a time while keeping the others constant [60], [84], [96], [99]. By varying both the backbone concentration ($[B]$) and the monomer concentration ($[M]$) at the same time, a more comprehensive understanding of the system can be gathered. Furthermore, from reviewing the literature, it appears that the amylopectin and methyl acrylate system has not been thoroughly studied for a wide range of polymerization conditions.

To address this deficiency, the most important grafting parameters for the graft copolymers produced following the central composite design (CCD) were investigated. The grafting parameters, calculated after the graft copolymerization and purification, are listed in Table 4.2. Even though optimizing the grafting parameters was not the objective of this work, a general prediction of how they are affected by reaction variables may be useful for future studies.

Table 4.2: Grafting parameter results for the amylopectin-*graft*-poly(methyl acrylate) (AP-*g*-PMA) grades.

Run (AP- <i>g</i> -PMA)	Monomer Conversion (%)	Grafting Efficiency (%)	Grafting Ratio	Add-on/ PMA wt. (%)	AP wt. (%)	PMA Homopolymer Fraction (%)
GP1	71	52	1.51	60	40	19
GP2	87	76	3.82	79	21	12
GP3	74	57	0.84	46	54	16
GP4	86	69	1.74	64	36	17
GP5	83	66	3.99	80	20	17
GP6	76	56	0.95	49	51	20
GP7	71	52	0.76	43	57	19
GP8	86	71	2.74	73	27	15
GP9	81	61	1.61	62	38	21
GP10	78	63	1.67	63	37	15
GP11	78	64	1.69	63	37	14

4.1.3 Effects on Monomer Conversion

Figure 4.1 shows that methyl acrylate conversion is mainly affected by monomer concentration, as conversion significantly increases with monomer concentration. This behaviour was expected, since the rate of polymerization (either for AP-*g*-PMA or PMA) is proportional to monomer concentration. Increasing the backbone concentration at high monomer concentrations appears to have a slightly negative impact on the monomer conversion. This may be due to the increased viscosity of the polymerization medium at higher backbone concentrations, which may slow down the propagation of methyl acrylate.

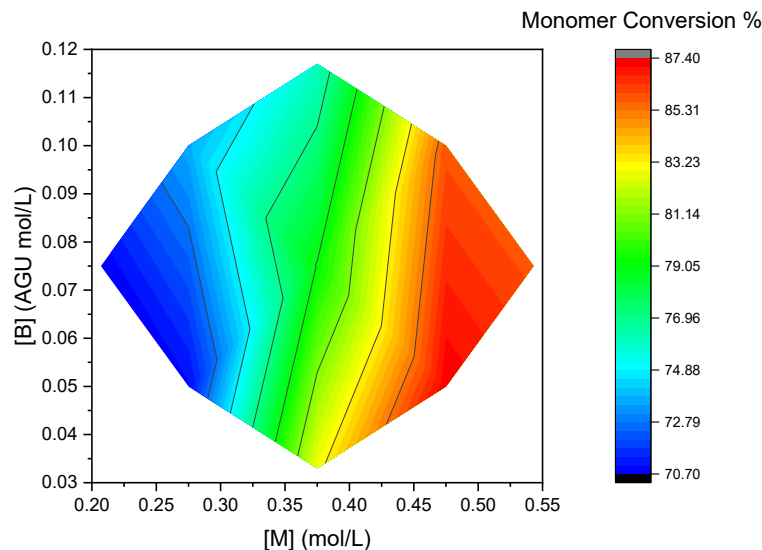


Figure 4.1: Methyl acrylate conversion as a function of methyl acrylate [M] and amylopectin [B] concentration.

4.1.4 Effects on Grafting Efficiency and Homopolymer Formation

Similar to the trends for monomer conversion, grafting efficiency increases markedly when higher monomer concentrations are used (Figure 4.2). This agrees with the general consensus in the literature: when more monomer is present in the reactor, more monomer molecules become available for grafting reactions with the backbone macroradicals [60], [84], [96], [99]. At lower monomer concentrations (see the left half part of the plot), increasing the backbone concentration slightly improves the grafting efficiency, but the opposite trend is observed at higher monomer concentrations. It has been previously reported that increasing the backbone concentration up to a certain threshold value may improve the grafting efficiency by creating more available grafting sites, but once this limit is crossed it may have the opposite effect [84]. When the backbone concentration is increased past this limit, grafting reactions may be hindered by an increase in solution viscosity and an increase in the rate of termination due to greater macroradical interactions [84], [112], [113]. Furthermore, it has also been suggested that when the monomer concentration is too high, the lower monomer-to-backbone macroradical ratio may lead to greater homopolymerization and lower grafting efficiencies [60], [84], [99].

Even though in this work, no significant trends for homopolymer formation (Figure 4.3) were observed, the monomer range tested may not have gone beyond the point where homopolymerization would dominate. As well, despite no obvious trends, a significant portion of the monomer converts to homopolymers (~ 12–21%), which ultimately decreases the overall grafting efficiency.

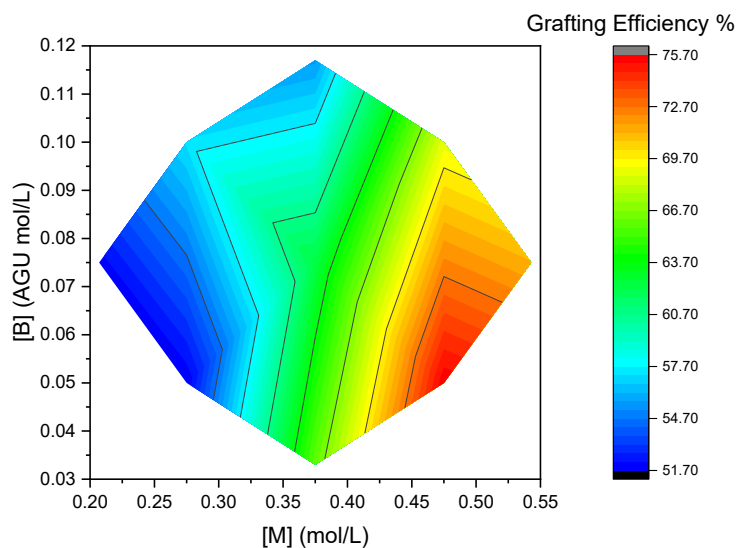


Figure 4.2: Grafting efficiency as a function of methyl acrylate [M] and amylopectin [B] concentration.

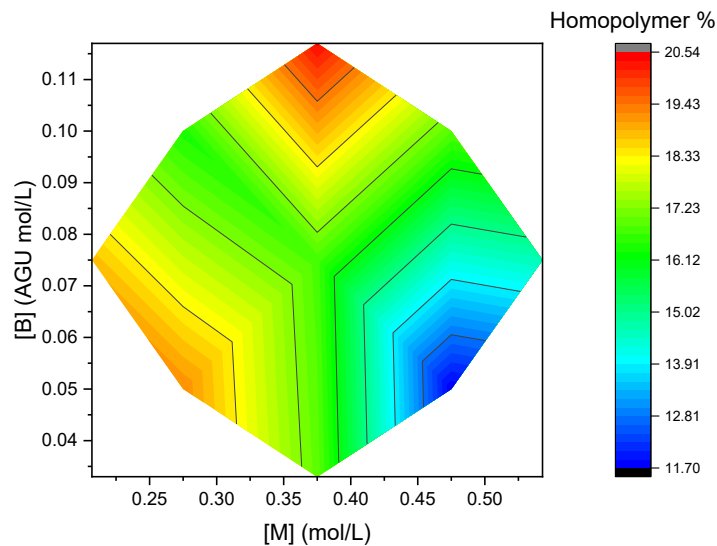


Figure 4.3: Homopolymer percentage as a function of methyl acrylate [M] and amylopectin [B] concentration.

4.1.5 Effects on Grafting Ratio

The contour plot for grafting ratio is shown in Figure 4.4. The observable trends can easily be explained as the grafting ratio is simply the ratio of grafted PMA chains to the AP backbone. As expected, the grafting ratio is highest (lower right quadrant) when the monomer concentration is high and the backbone concentration is low, decreasing for lower monomer concentrations and higher backbone concentrations (upper left quadrant). This trend has also been noted in previous studies and is confirmed in this work [96], [114].

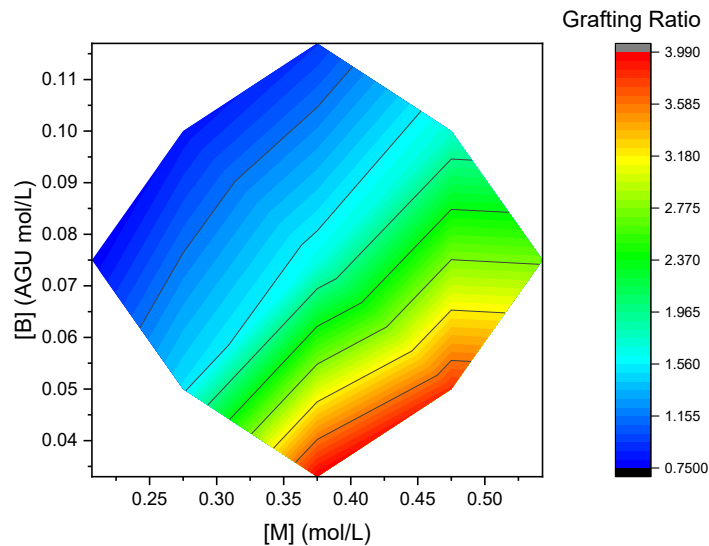


Figure 4.4: Grafting ratio as a function of methyl acrylate [M] and amylopectin [B] concentration.

4.2 Hydrolysis Discussion

The intent of the hydrolysis reaction was to create water-soluble flocculants by adjusting the charge density whilst maintaining some hydrophobicity. Multiple screening experiments were initially performed using exact molar amounts of the base to obtain partially hydrolyzed graft copolymers at various hydrolysis levels. The resulting products were not completely water-soluble, thus resulting in extremely poor flocculation performance. Therefore, each hydrolysis was run with an excess of NaOH to produce fully hydrolyzed and water-soluble polymers in the proposed CCD.

It is also important to point out that although the saponification reaction of the methyl groups to carboxylate groups is desired in the hydrolysis step, it has been reported that an undesired depolymerization reaction of the backbone may also occur [115], [116]. Even though starches have a higher affinity towards water in the presence of an alkali, it has also been noted that increased temperatures can cause starches to undergo some degradation [115], [117]. However, previous studies have further shown that this unwanted reaction is largely avoided if the NaOH concentration in the solution is lower than 1.0 (N) [115], [116], [118]. To avoid impacting the integrity of the amylopectin, the concentration of alkali was kept below this limit such that only the saponification reaction would occur. Moreover, it has been also been suggested in the literature

that in the case of starch, amylopectin is impacted by the alkali to a lesser degree than amylose; as such, it should undergo little to no degradation [117].

4.3 Proof of Grafting and Flocculant Characterization

4.3.1 FTIR Analysis

Figure 4.5 compares the FTIR analyses of PMA, commercial AP, and AP-g-PMA (made at the centre point, sample GP11). To confirm that PMA chains were indeed grafted to the AP backbone, the key absorption peaks of PMA and AP were first identified and then compared to the spectrum of the AP-g-PMA graft copolymer. If grafting was successful, the AP-g-PMA spectrum should present peaks for the key functional groups of both the AP and PMA. The FTIR spectrum for AP shows a broad peak at approximately 3325 cm^{-1} (-OH stretching), a peak at 2920 cm^{-1} (-CH stretching), and triplet peaks at 1150 , 1080 , and 1000 cm^{-1} (C-O stretching) [90], [119], [120]. Table 4.3 provides a detailed FTIR peak summary for AP [107], [121]. In the PMA spectrum, the main absorption peaks arise at approximately 2950 cm^{-1} (-CH stretching), 1440 cm^{-1} (-CH bending), and 1727 and 1155 cm^{-1} (C=O and C-O stretching for the ester functionalities, COOCH_3) [90], [95]. The list of characteristic functional groups and corresponding wavenumbers for PMA are listed in Table 4.4 [107], [121].

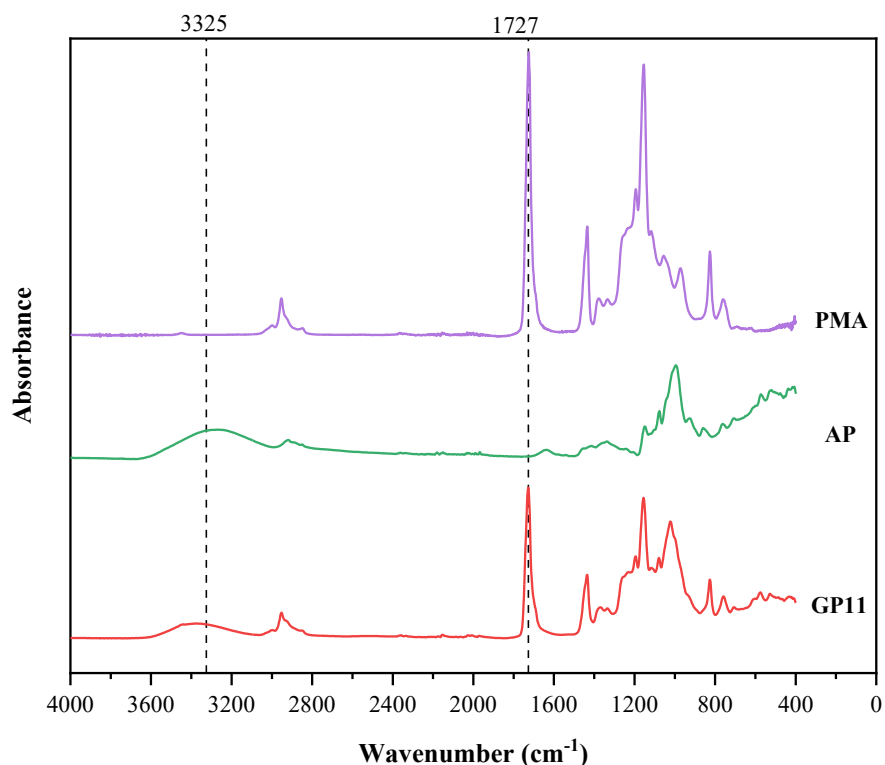


Figure 4.5: FTIR absorbance spectra of poly(methyl acrylate) (PMA), amylopectin (AP), and amylopectin-*graft*-poly(methyl acrylate) (AP-g-PMA) (sample GP11).

Figure 4.5 shows that the absorption peaks for key functional groups of both AP and PMA are present in the purified AP-g-PMA sample: 3325 cm^{-1} corresponding to -OH stretching in AP and 1727 cm^{-1} for C=O stretching in PMA. Since the AP spectrum lacks strong peaks between $1800\text{--}1500\text{ cm}^{-1}$, the presence of a peak in this region for GP11 proves the presence of PMA chains via their carbonyl (C=O) stretching peak. Likewise, the broad -OH stretch peak is present in GP11, but absent from the PMA spectrum. This is a clear confirmation that the AP backbone is also present in the graft copolymer. Furthermore, the intensity of the -OH stretch in the graft copolymer is noticeably weaker than in the unmodified AP, suggesting that grafting has taken place through the hydroxyl groups, as expected.

Table 4.3: Amylopectin (AP) FTIR absorption peaks and corresponding functional groups.

Peak Assignment	Wavenumber (cm ⁻¹)
* -OH (stretching)	~3600-3000
-CH (stretching)	~2900-2800
-OH (bending)	~1650
-CH ₂ (symmetric bending)	~1420
-CH (bending)	~1350
C-O (antisymmetric stretching)	~1150
C-OH (stretching)	~1080
C-O, C-C, and C-O-C (stretching)	~1000
Anhydroglucose ring (stretching)	~929, 855, 765, 575

*Key attributable peak in the AP-g-PMA spectrum

Table 4.4: Poly(methyl acrylate) (PMA) FTIR absorption peaks and corresponding functional groups.

Peak Assignment	Wavenumber (cm ⁻¹)
-CH (stretching)	~3000-2850
* C=O (ester) (stretching)	~1727
-CH (antisymmetric and symmetric bending)	~1440 & 1375
C-O (ester) (stretching)	~1300-1000

*Key attributable peak in the AP-g-PMA spectrum

Figure 4.6 further investigates these polymers by comparing a physical blend of AP and PMA (no grafts), purified sample GP11, and crude sample GP11. When comparing the unwashed crude GP11 with the purified GP11 sample, the peak wavenumbers remain unaltered, while the relative intensities of the AP peaks increase after the purification, showing that as the PMA ungrafted chains were washed away, the proportion of AP in the final graft product increased. In addition, the relative intensities of the PMA peaks did not decrease substantially after purification, suggesting that the final grafted product still contained a large proportion of PMA.

Even though the presence of both AP and PMA in the AP-g-PMA graft copolymer suggests that grafting is likely to have occurred, there were no identifiable characteristic grafting peaks that

differed from the AP and PMA spectra. Therefore, this spectrum alone cannot be used as indisputable evidence of grafting. Additionally, when comparing the spectra of GP11 and the AP-PMA blend, the absorption peaks appear almost identical. This was expected as the composition of the blend was designed to be the same as that of GP11. As no discernible differences exist between the two spectra, it is not conclusive from the FTIR analysis that GP11 is grafted and not just a blend of two homopolymers; however, the strong intensity of both AP and PMA peaks even after the extensive purification steps helps support the assumption that the final product was not a simple blend (refer to Appendix A for more information).

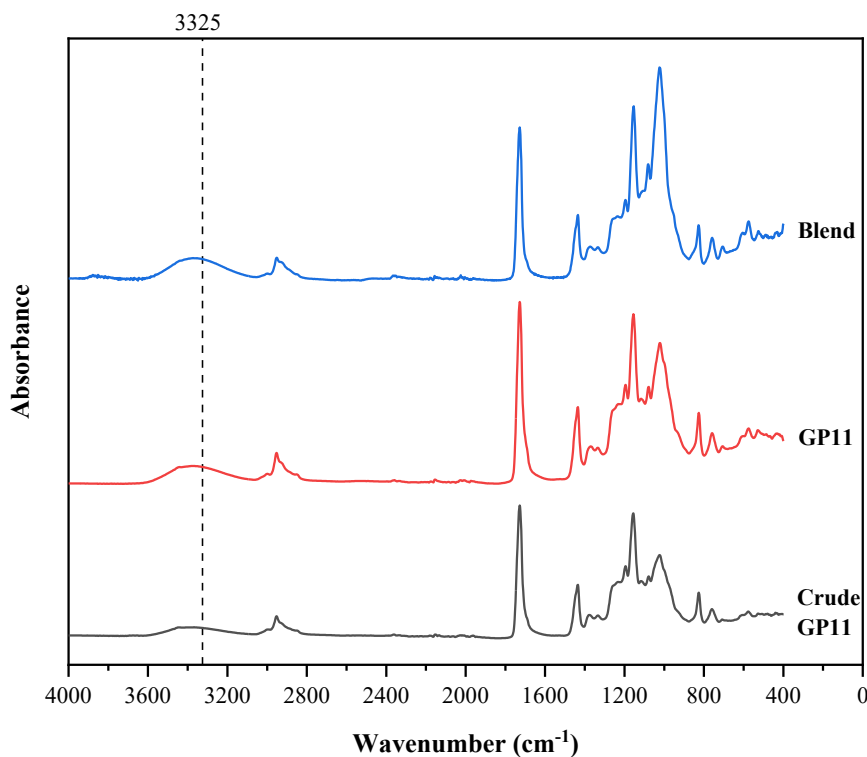


Figure 4.6: FTIR absorbance spectra of the amylopectin and poly(methyl acrylate) (AP-PMA) blend, amylopectin-graft-poly(methyl acrylate) (AP-g-PMA) (sample GP11), and crude GP11.

After hydrolysis, some prominent differences can be observed in the graft copolymer spectra. Figure 4.7 compares the graft copolymer before (GP3) and after hydrolysis (HGP3). The major differences between GP3 and HGP3 are the disappearance of the carbonyl stretch in the

ester group (COOCH_3) at 1727 cm^{-1} , and the appearance of two new peaks at about 1555 cm^{-1} and 1400 cm^{-1} . These peaks are characteristic of the asymmetric (1555 cm^{-1}) and symmetric (1400 cm^{-1}) stretching vibrations in the carboxylate functionalities (COO^-) formed during the hydrolysis [90]. The peak at 1727 cm^{-1} completely disappeared, proving that complete hydrolysis was achieved. This was also confirmed for the other grades of the graft copolymer.

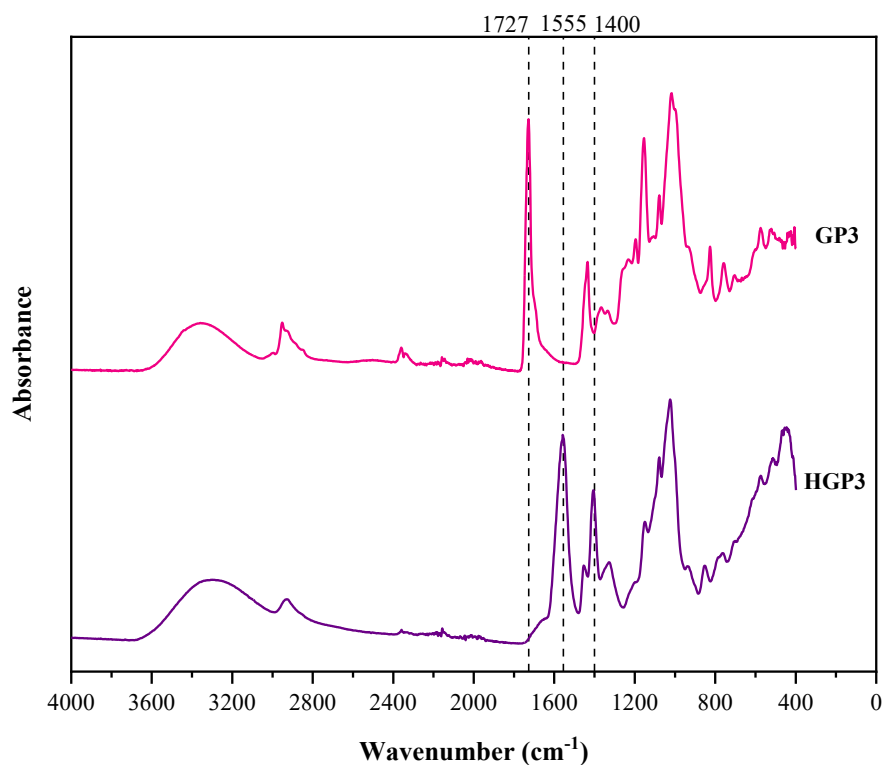


Figure 4.7: FTIR absorbance spectra of amylopectin-*graft*-poly(methyl acrylate) (AP-*g*-PMA) (sample GP3), and amylopectin-*graft*-hydrolyzed-poly(methyl acrylate) (AP-*g*-H-PMA) (sample HGP3).

4.3.2 ^1H NMR Analysis

A ^1H NMR study was performed to investigate if the grafting reaction was successful. The ^1H NMR spectra for AP, PMA, the AP-PMA blend, and an AP-*g*-PMA centre point (GP10) before hydrolysis are shown in Figure 4.8, Figure 4.9, Figure 4.10, and Figure 4.11, respectively. In each figure, the chemical structure is provided, the carbon atoms are numbered, and the key hydrogen

atoms are highlighted. The chemical shifts have also been labelled based on their corresponding hydrogen atoms.

In Figure 4.8, the peaks identified are characteristic of AP and are consistent with previous studies [122]–[124]. The chemical shifts at 5.416 ppm and 5.342 ppm are due to the hydroxyl protons attached to C₃ and C₂ (-OH), respectively, and the signal at 4.530 ppm is indicative of the hydroxyl proton of C₆ (-OH). The peak at 5.045 ppm is due to the proton attached to C₁ (-CH). Additionally, the two hydrogen atoms linked to C₆ (-CH₂) and the other protons in the glucose ring, attached to C₂, C₃, C₄, and C₅ (-CH) cause the peak range from 3.270 ppm to 3.587 ppm. Interestingly, a small peak appears around 4.849 ppm. According to previous studies, this is largely due to branching (α -1,6 glycosidic linkages) in AP as this signal is not typically present for amylose [123]. As deuterated DMSO was used as the solvent for this test, its corresponding peak appears at 2.449 ppm in the spectrum. Unexpectedly, a large, sharp signal appears at about 3.372 ppm which is not consistent with the expected AP spectrum. This chemical shift results from water absorbed in the sample. As DMSO-d₆ is highly hygroscopic, over time and during handling the solvent can absorb moisture in the air and a strong water peak may appear in the spectrum which is difficult to avoid [125].

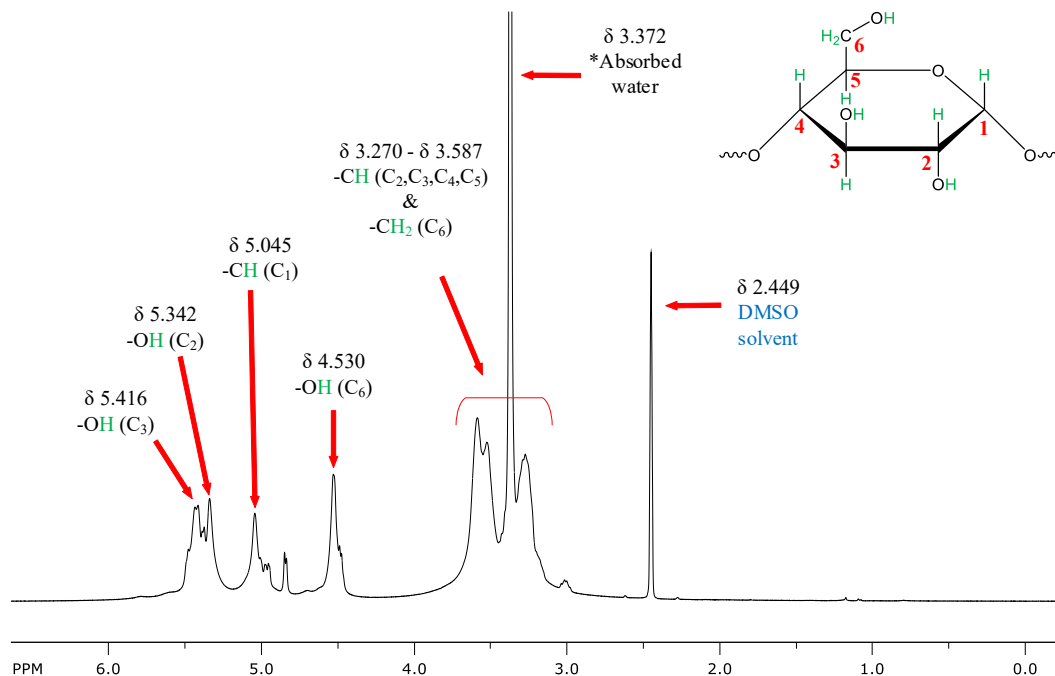


Figure 4.8: ^1H NMR spectrum for amylopectin (AP).

Figure 4.9 displays the ^1H NMR spectrum for PMA. The three different types of hydrogen atoms in this polymer are attached to C_7 , C_8 , and C_{10} , which correspond to three distinct chemical shift regions. The peak at 3.518 ppm is characteristic of the three protons connected to C_{10} ($-\text{OCH}_3$), and the broad peak at 2.154 ppm is attributed to the proton attached to C_7 ($-\text{CH}$). Furthermore, the hydrogen atoms associated with C_8 ($-\text{CH}_2$) are the cause for the peaks between 1.405 ppm to 1.709 ppm. The deuterated DMSO peak can also be seen at 2.446 ppm and an absorbed water peak is present at a shift of 3.287 ppm. It is important to note that there is no MA left in this sample, as alkene protons in MA would cause peaks between 5.5 and 6.5 ppm [90]. As such, the identified chemical shifts in the spectrum were expected for PMA and agree with the literature [95].

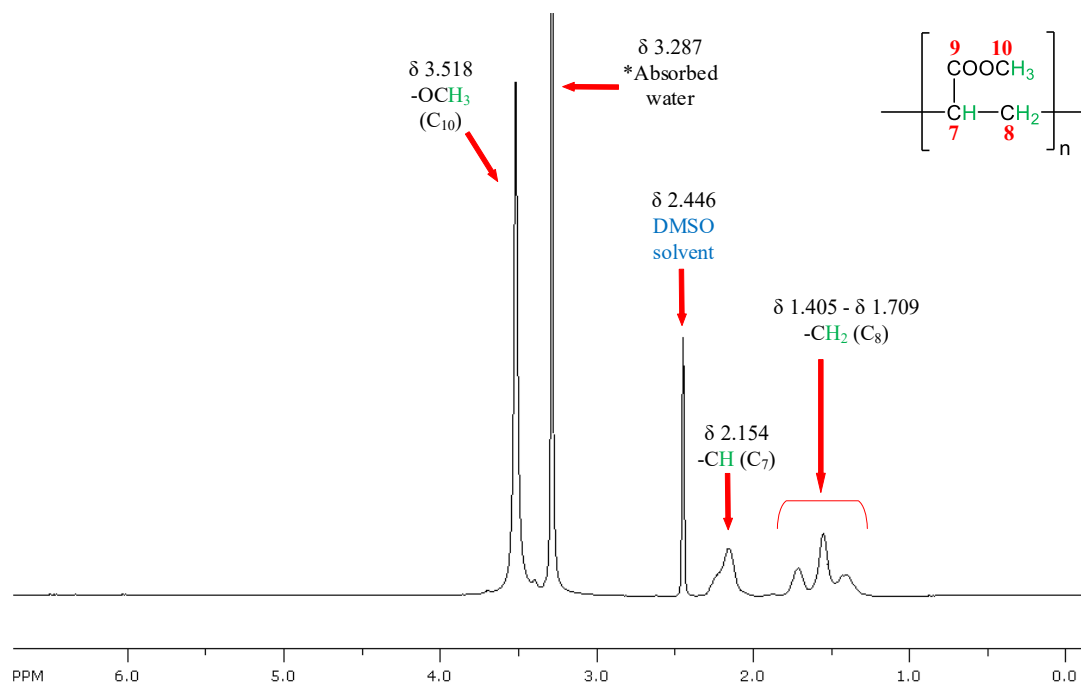


Figure 4.9: ^1H NMR spectrum for poly(methyl acrylate) (PMA).

The AP-PMA blend and the AP-g-PMA (GP10) proton NMR spectra are shown in Figure 4.10 and Figure 4.11, respectively. These spectra were compared to determine whether the grafting point could be determined. In both spectra, the indicative signals of AP and PMA are seen with no discernible MA monomer peaks. The DMSO- d_6 solvent peak and the absorbed water peak are also visible in both spectra. Furthermore, in the GP10 spectrum, the signal at 2.063 ppm is likely due to residual acetone from the purification step. As the AP and PMA peaks overlap from 3.0 to 4.0 ppm, the other notable AP peaks can be seen between 4.5 to 5.5 ppm, while the distinctive PMA signals are visible from 1.4 to 2.2 ppm. As both components are present in the graft copolymer after extensive purification, it is likely that the grafting reaction did happen. This evidence, however, is not unquestionable as both components are also present in the blend and one may argue that the purification step was not efficient enough to remove all ungrafted material from the product.

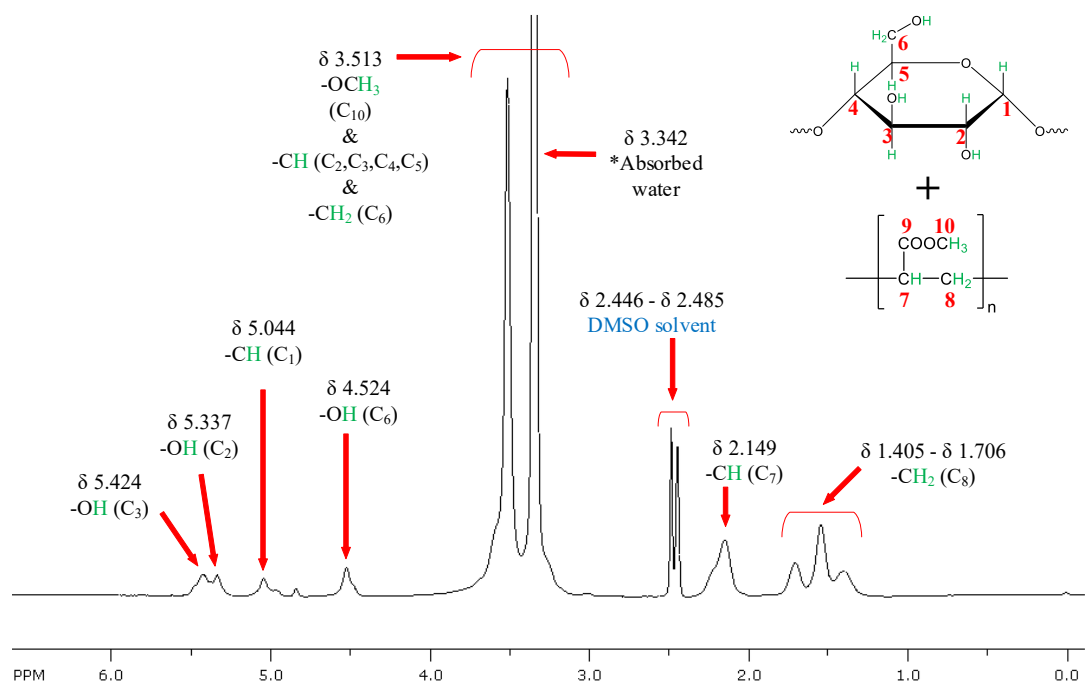


Figure 4.10: ¹H NMR spectrum for the amylopectin and poly(methyl acrylate) (AP-PMA) blend.

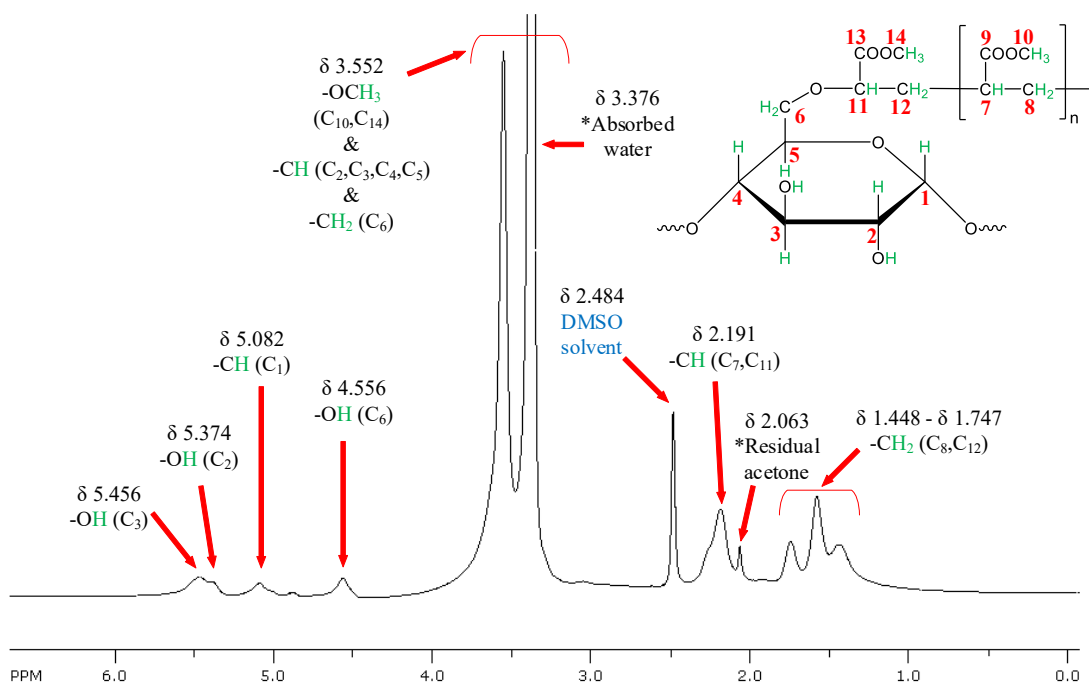


Figure 4.11: ¹H NMR spectrum for amylopectin-graft-poly(methyl acrylate) (AP-g-PMA) (sample GP10).

Taking a closer look at the region of the hydroxyl protons (~ 4 to 6 ppm), a comparison of AP, the AP-PMA blend, and GP10 in Figure 4.12 shows some significant differences. As the grafting reaction takes place through the abstraction of hydroxyl protons, looking at this region may show where this reaction may have occurred. The most prominent difference in the GP10 spectrum appears when the peak of the hydroxyl proton for C₆ (-OH) is compared to the others. The signal intensity appears similar for AP and the blend, but it noticeably decreases for GP10. As the signal intensity for proton NMR is proportional to the molar concentration, this may be an indication that most of the grafting occurred at C₆. Another difference between the spectra appears with the hydroxyl proton at C₂ (-OH), as its intensity has slightly decreased for GP10 as well. This may indicate that grafting does not solely take place at C₆ but may also to a lesser degree occur elsewhere, such as at C₂.

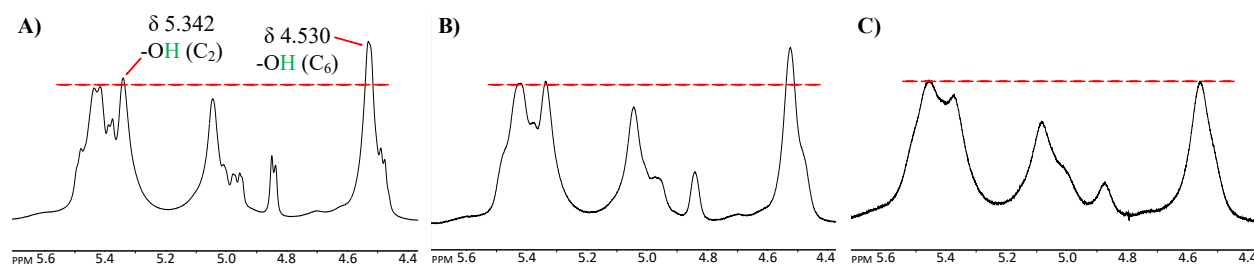


Figure 4.12: ¹H NMR spectra of the hydroxyl regions for A) amylopectin (AP), B) amylopectin and poly(methyl acrylate) (AP-PMA) blend, and C) amylopectin-*graft*-poly(methyl acrylate) (AP-*g*-PMA) (sample GP10).

4.3.3 ¹³C NMR Analysis

The ¹³C NMR results for the same AP, PMA, AP-PMA blend and AP-*g*-PMA (GP10) samples are shown in Figure 4.13, Figure 4.14, Figure 4.15, and Figure 4.16, respectively. In each figure, the chemical structure is provided, and the carbon atoms are numbered and highlighted. The NMR signals have also been labelled based on their corresponding carbon atoms.

In Figure 4.13, the peaks representing the six different carbon atoms in AP are consistent with the literature [90], [95], [122], [123]. The sharp peak at 100.416 ppm is indicative of C₁ and the peak at 79.079 ppm is attributed to C₄. The three peaks at 73.580 ppm, 72.312 ppm, and 71.955

ppm are associated with C₃, C₂, and C₅, respectively. Lastly, the signal at about 60.820 ppm is caused by C₆ in the AP structure. On the righthand side of the spectrum, the very large peak at 39.831 ppm is characteristic of the deuterated DMSO solvent.

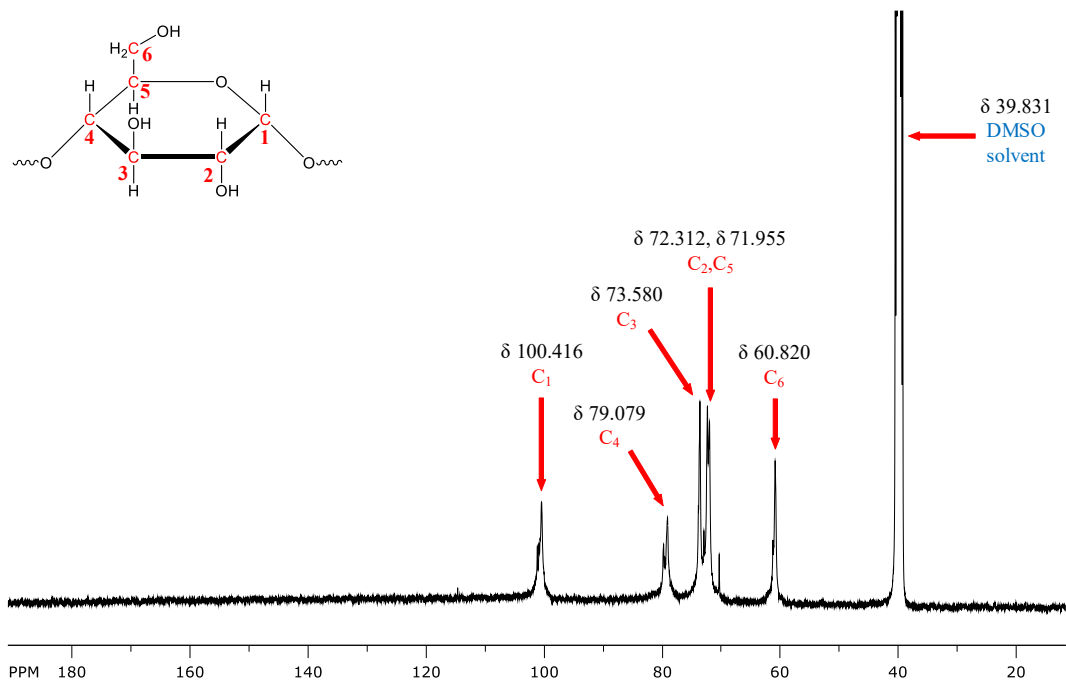


Figure 4.13: ¹³C NMR spectrum for amylopectin (AP).

Figure 4.14 displays the ¹³C NMR chemical shifts corresponding to the four different carbons in PMA. The shift on the left side of the spectrum at 174.755 ppm is characteristic of C₉, while the peak at 51.932 ppm is associated with C₁₀. Additionally, the less intense peak at 34.683 ppm is attributed to C₈. A large residual DMSO-d₆ solvent peak is present at 39.926 ppm, and a shouldering signal at 41.141 ppm is due to C₇. These peaks agree with the previous literature results for PMA [90], [95]. Again, it can be noted that no unreacted MA remains in the sample, as alkene carbons produce a peak around 130 ppm, which is absent from the PMA spectrum [90].

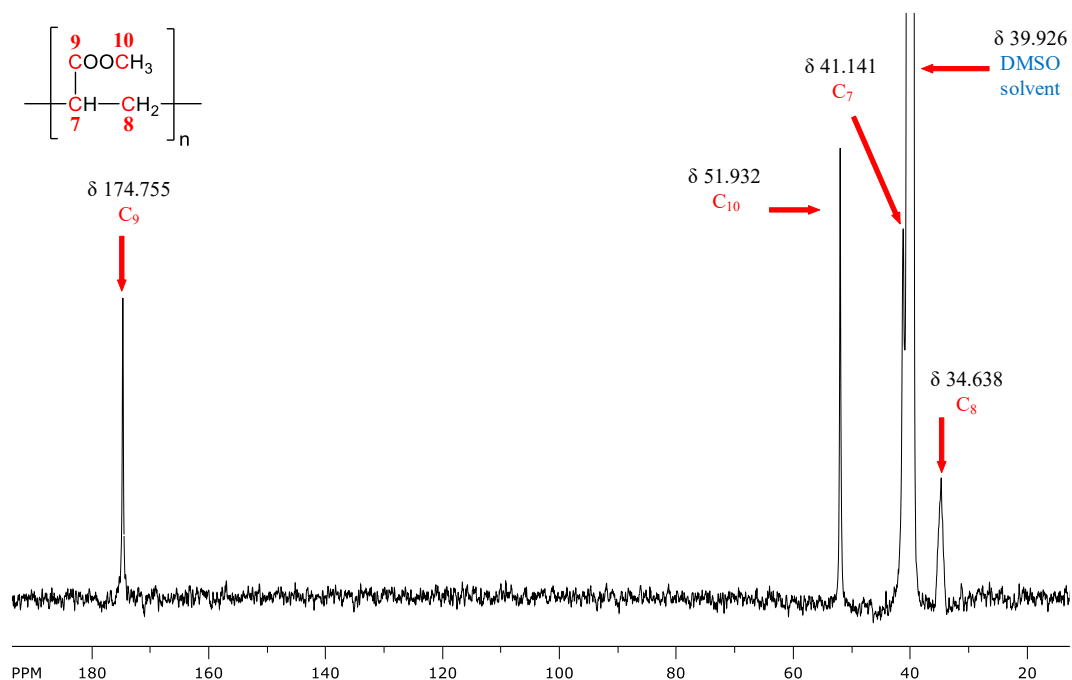


Figure 4.14: ^{13}C NMR spectrum for poly(methyl acrylate) (PMA).

The ^{13}C NMR results for the AP-PMA blend and the AP-*g*-PMA (GP10) are shown in Figure 4.15 and Figure 4.16, respectively. Both the polymer blend and the graft copolymer were compared to determine whether a distinct grafting point could be located. As the location of the AP and PMA chemical shifts in the carbon spectrum do not overlap, all the diagnostic signals of AP and PMA can be identified in both spectra, proving that both components are present. In addition, there are no discernible MA monomer peaks. As in the proton spectrum of GP10, a residual acetone peak is seen in its carbon spectrum at 31.090 ppm. It has been suggested that the point of chemical grafting on the AP backbone occurs at C_6 , either as a broadening or shoulder on the C_6 peak for solid-state ^{13}C NMR or, by the addition of a very small sharp peak downfield of C_6 in solution-state ^{13}C NMR [62], [95], [120], [126], [127]. It has been postulated that because a fraction of the hydroxyl groups attached to C_6 participate in the grafting reaction, the peak should slightly shift downfield due to the shielding effect [95], [126]. In the case of the GP10 spectrum, a new peak near C_6 was not discernible, possibly due to solubility issues increasing the background noise. Unlike the proton spectrum, the carbon spectrum gave no perceptible evidence of a grafting point; however, as both components were present in the spectrum after extensive purification, grafting likely occurred in this product.

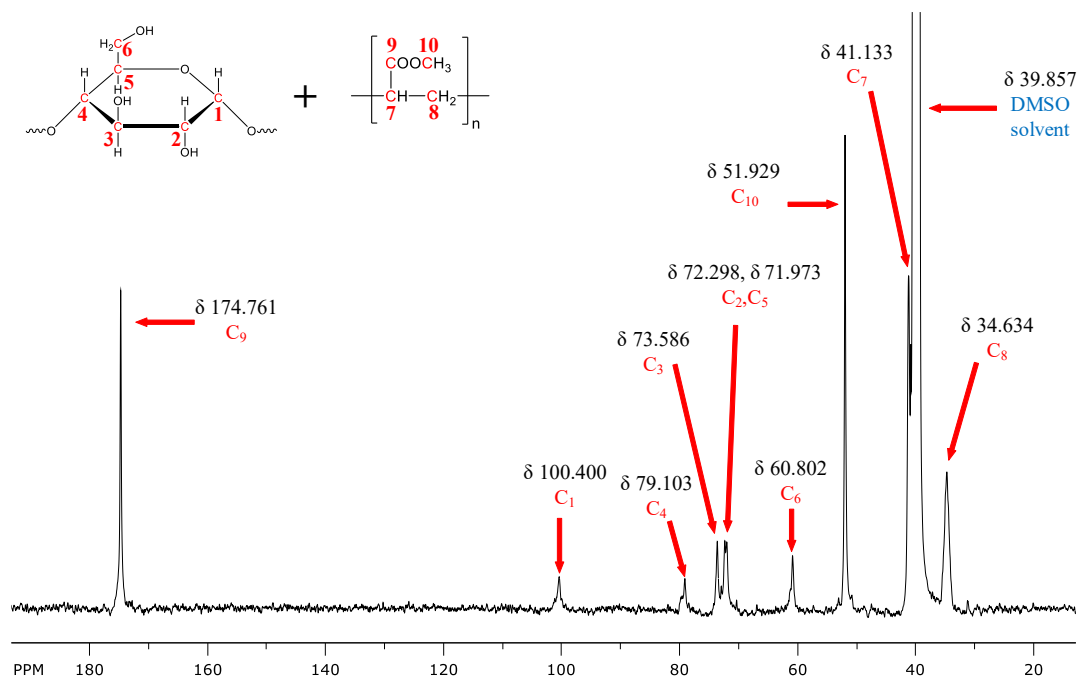


Figure 4.15: ¹³C NMR spectrum for the amylopectin and poly(methyl acrylate) (AP-PMA) blend.

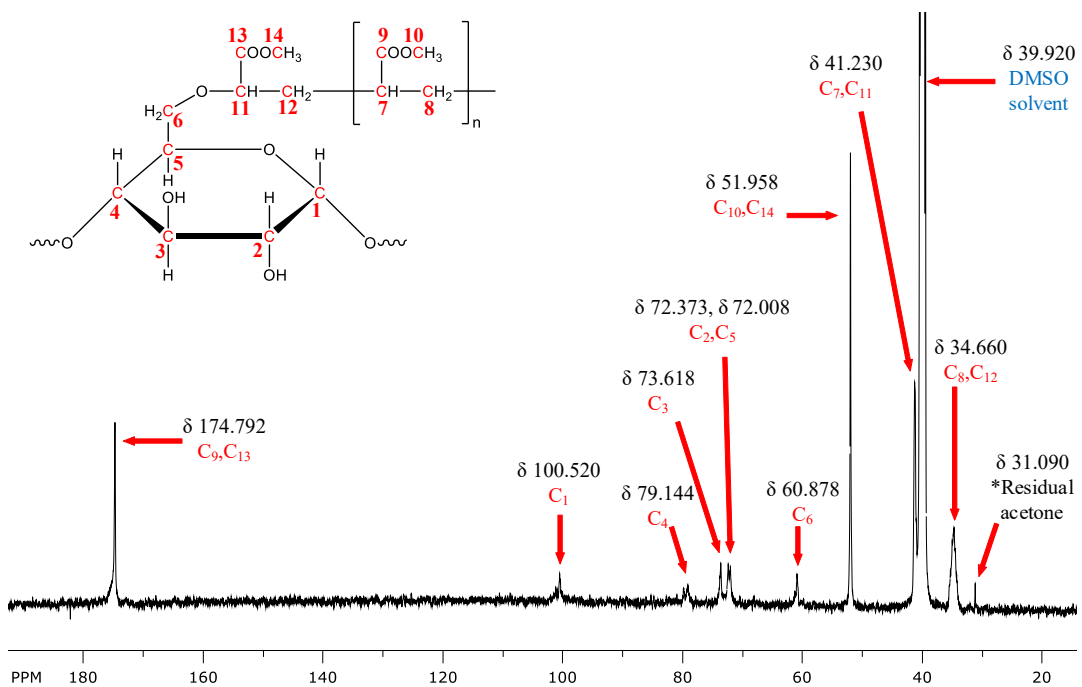


Figure 4.16: ¹³C NMR spectrum for amylopectin-graft-poly(methyl acrylate) (AP-g-PMA) (sample GP10).

4.3.4 HiM Morphological Analysis

The HiM images of the polymer surface morphologies are shown in Figure 4.17, Figure 4.18, Figure 4.19, Figure 4.20, and Figure 4.21. These images were analyzed to observe if the surface of the AP-g-PMA graft copolymer differed from the homopolymers and polymer blend. The morphology of commercial AP powder is distinctly granular, as seen in Figure 4.17. The granules appear to have smooth surfaces with a distribution of sizes and irregular shapes [119], [120]. This morphology changes drastically when the AP is gelatinized, as visible in Figure 4.18. The distinct granules appear to have shrunk and formed an interconnected thread-like network. This appears to show that even though the distinct granular shape has disappeared, the AP does not fully dissolve. This makes sense, as the resulting solution is not completely transparent. This morphology is considerably different than that of PMA, shown in Figure 4.19, which contains larger and relatively smooth linked segments.

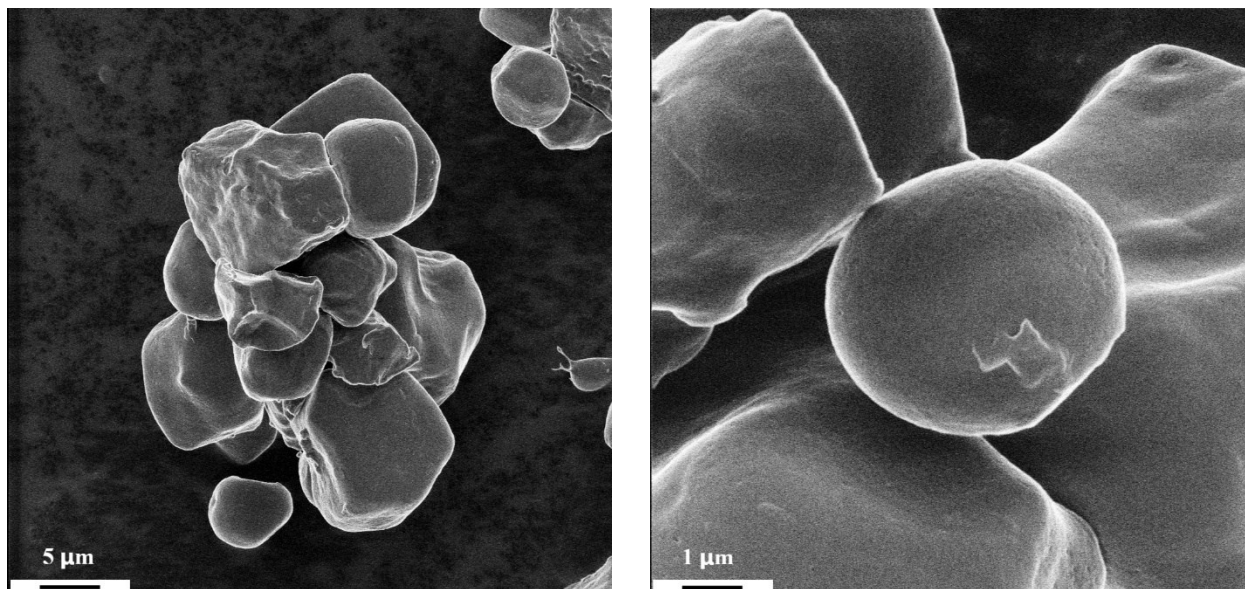


Figure 4.17: HiM images of commercial amylopectin (AP) powder.

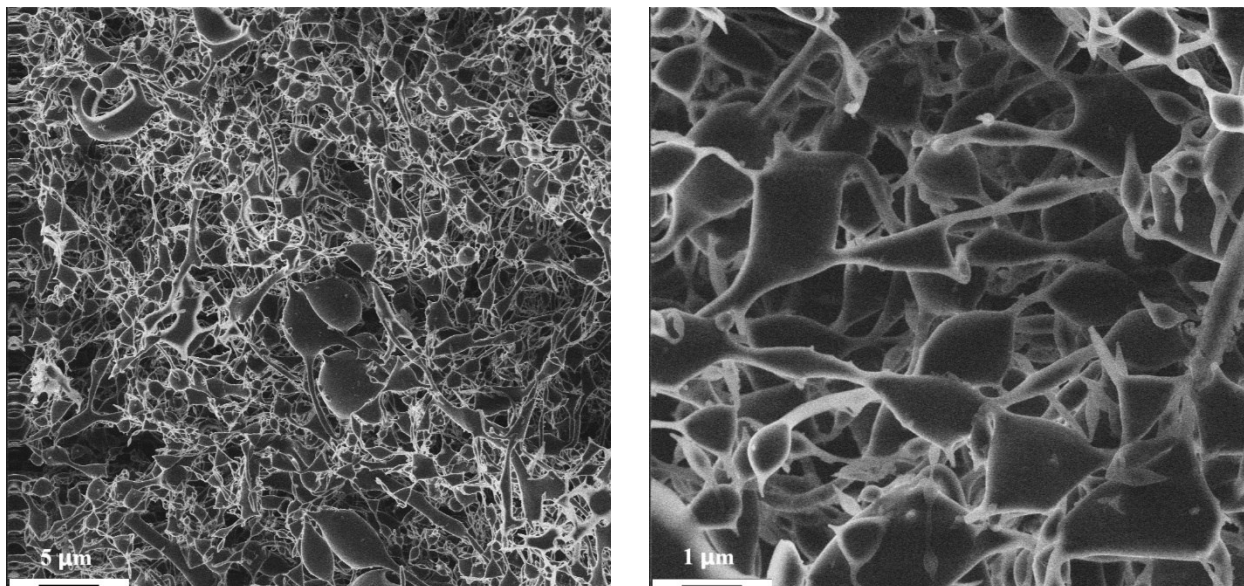


Figure 4.18: HiM images of gelatinized amylopectin (AP).

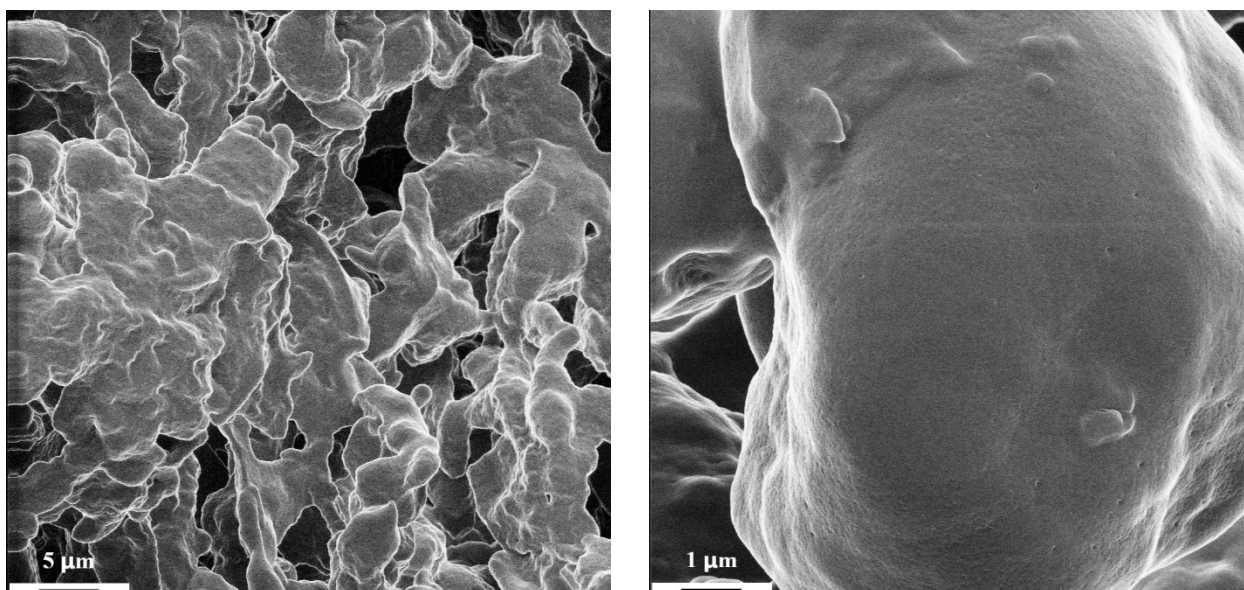


Figure 4.19: HiM images of poly(methyl acrylate) (PMA).

The morphology differences were analyzed further by comparing Figure 4.20 and Figure 4.21, which show the AP-PMA blend and the AP-g-PMA (GP10), respectively. At the lowest magnification, the blend and the graft copolymer images look similar, but the blend appears to have coarser surface structures. As the magnification is increased, this roughness in the blend can

be explained, as two distinct morphologies are identified. The blend contains larger polymer portions (likely PMA), which are covered by regions of a smaller polymer constituent (likely AP). This differs from the graft copolymer, as the higher magnification images show a single uniform polymer. This evidence supports the assumption that the graft copolymer is indeed chemically connected and not just a physical mixture of the two homopolymers.

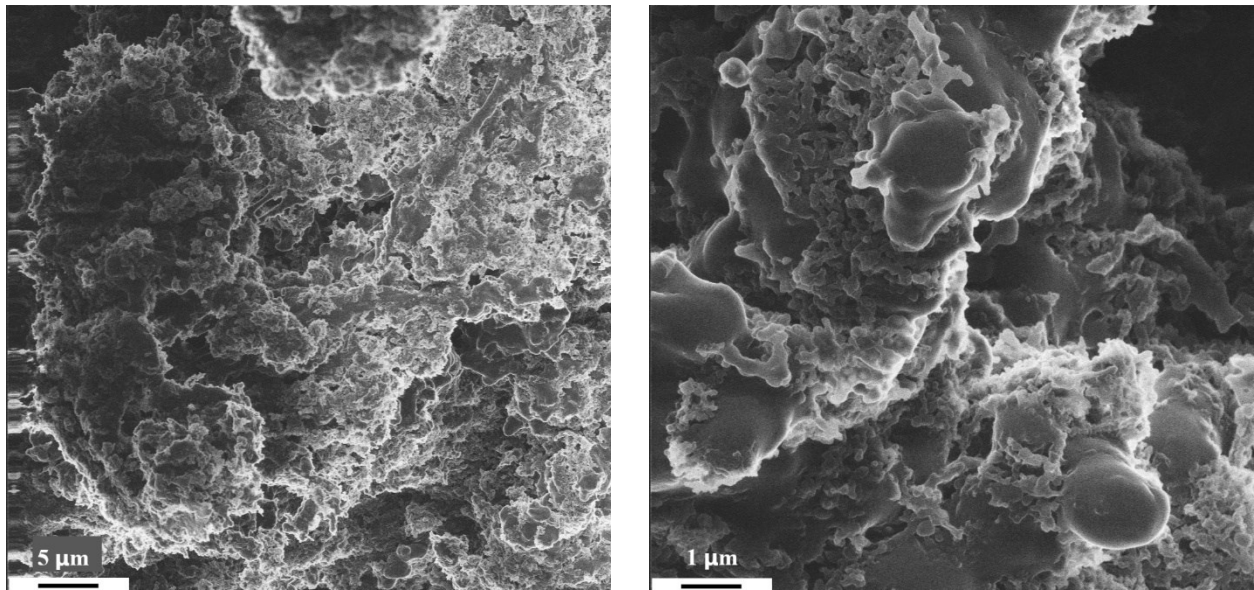


Figure 4.20: HiM images of the amylopectin and poly(methyl acrylate) (AP-PMA) blend.

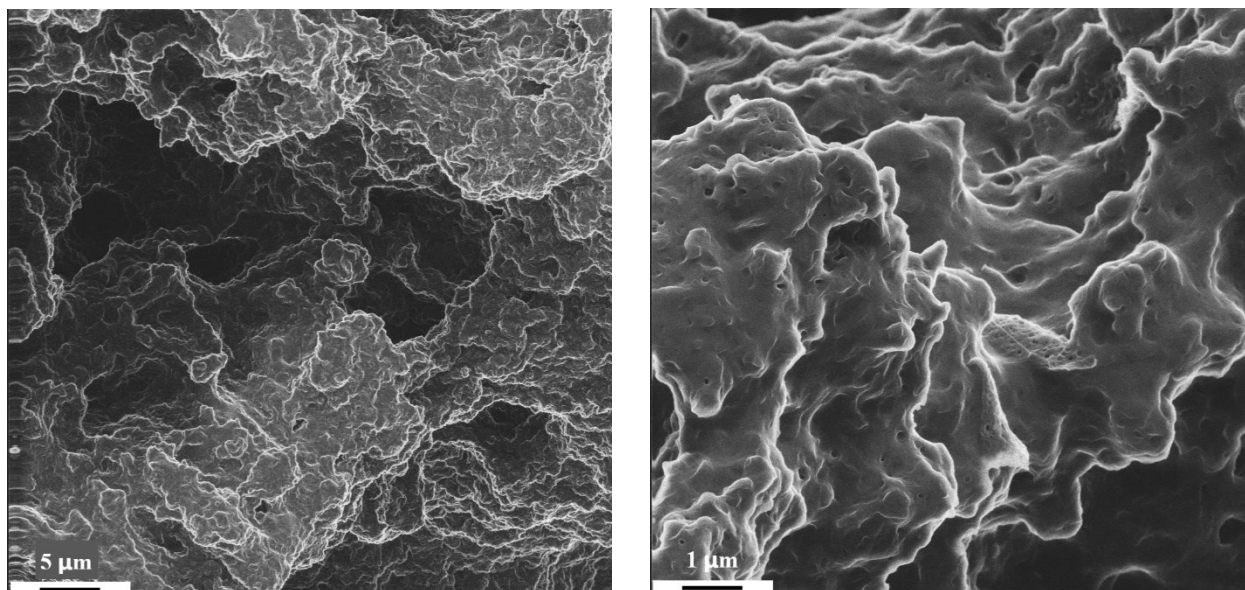


Figure 4.21: HiM images of amylopectin-*graft*-poly(methyl acrylate) (AP-*g*-PMA) (sample GP10).

4.3.5 Thermal Analysis

Figure 4.22 compares the TGA analyses of commercial AP, PMA homopolymer, AP-*g*-PMA (GP9), and the AP-PMA blend. The TGA curve for AP comprises two distinct weight loss regions. The primary weight loss zone, between 25 and 150 °C, is due to moisture present within the sample. As seen in the literature, AP degradation is represented by the second and largest weight loss region, occurring from 290 to 380 °C, with the largest loss zone taking place between 325 and 350 °C [60]. A similar trend is seen for PMA, with an initial weight loss zone from 25 to 150 °C (due to moisture) and a large decomposition region occurring between 300 and 455 °C [90]. PMA is more thermally resistant than AP, as most of the polymer degradation occurs above 400 °C. The weight loss trend for GP9 shows three separate weight loss regions and is consistent with the literature [91]. The first region is due to the loss of residual moisture, while the second and third regions are attributed to AP and PMA degradation, respectively. As the thermal degradation trends of both AP and PMA are present in the graft copolymer after extensive purification, this indicates that PMA chains have been grafted onto the AP backbone. The TGA curve for the AP-PMA blend was also compared to further scrutinize this claim. The weight loss trend for the blend is similar to the graft copolymer, as both AP and PMA weight loss regions can be seen, but a subtle difference between the curves can be identified in the second region. The AP

backbone degradation region for GP9 occurs at a noticeably lower temperature ($\sim 240\text{--}330\text{ }^{\circ}\text{C}$) than for the blend ($\sim 270\text{--}360\text{ }^{\circ}\text{C}$) and for the unmodified AP ($\sim 290\text{--}380\text{ }^{\circ}\text{C}$). This outcome was expected and agrees with the literature, as it has previously been observed that the thermal stability in this region of modified starch is lower than starch in its raw state [60], [128], [129]. Therefore, the lower thermal stability in this region for the graft copolymer is likely due to the modification of the AP backbone via the grafted PMA chains.

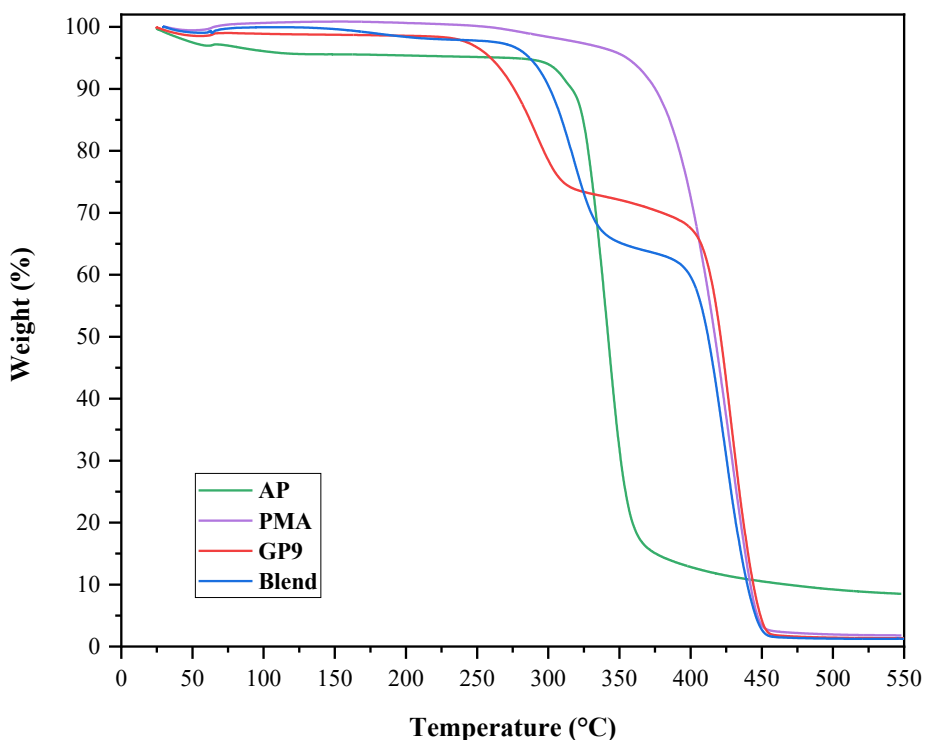


Figure 4.22: Thermal analysis comparison of amylopectin (AP), poly(methyl acrylate) (PMA), amylopectin-*graft*-poly(methyl acrylate) (AP-*g*-PMA) (sample GP9), and the amylopectin and poly(methyl acrylate) (AP-PMA) blend.

Figure 4.23 compares the thermal stability of five different grades of AP-*g*-PMA, including the axial points GP5, GP6, GP7, GP8, and centre point GP9. All graft copolymer grades follow the same trend with three distinct weight loss regions. The largest difference between the grades is due to the relative content of AP and PMA in the polymers. GP5 and GP6 were synthesized using the same concentration of monomer, but the backbone concentration was low for GP5 and

high for GP6. This can be seen in Figure 4.23 as the weight loss for the backbone degradation in GP5 is lower than that of the PMA grafted chains, while the AP degradation region is greater for GP6. GP7 and GP8 were synthesized using the same concentration of backbone, but the monomer concentration was low for GP7 and high for GP8. Figure 4.23 shows that the relative weight of PMA chains in GP7 is less than in GP8. As GP9 is the centre point in the CCD, the curve appropriately lies in the middle of the others. It is important to note that the physical form of the various graft copolymers differed based on their relative contents of AP and PMA. Higher PMA content in the graft copolymers resulted in rubbery polymers, compared to those which contained more AP, which were more powder-like. This structural difference may have also caused slight deviations in all the TGA results, and as a result, further testing should be done in this regard in the future.

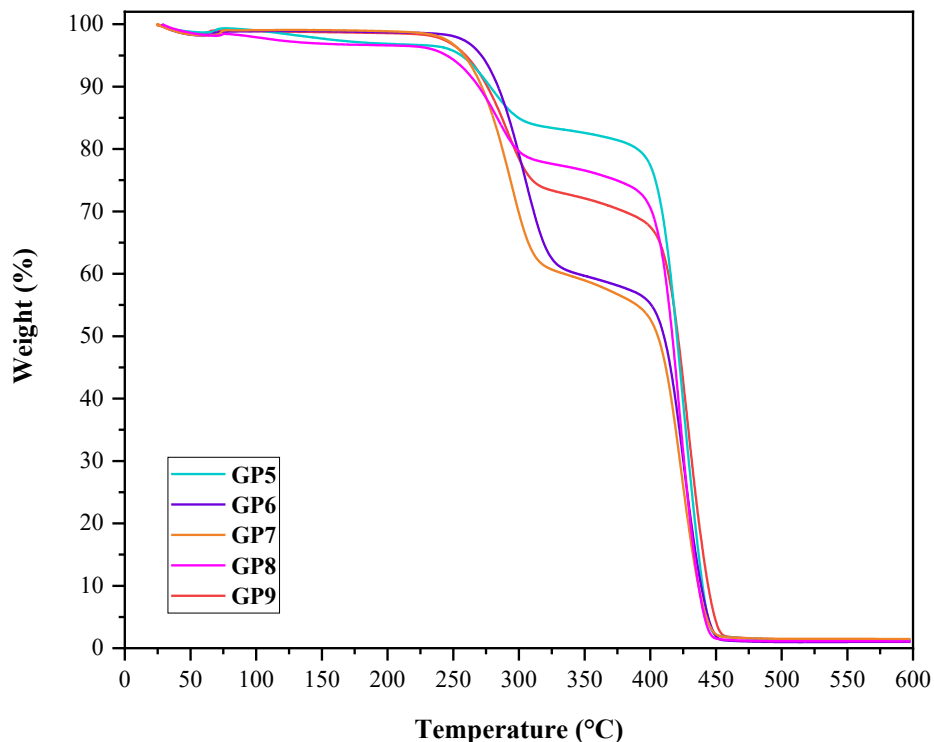


Figure 4.23: Thermal analysis of different grades of amylopectin-*graft*-poly(methyl acrylate) (AP-g-PMA).

4.3.6 Molecular Weight Analysis

The molecular weight results for the water-soluble flocculants measured by FFF are presented in Table 4.5. The number average molecular weights, M_n , varied from about 790,000 to 2,200,000 g/mol, while the weight average molecular weights, M_w , spanned from about 2,700,000 to 5,810,000 g/mol. These molecular weight averages are higher than those for the unmodified AP ($M_n \approx 400,000$ g/mol and $M_w \approx 1,700,00$ g/mol), confirming that grafting was successful. As expected, the polydispersity indices, PDI, were high since free radical polymerization was used to make the polymers. The variation in molecular weights reflects differences in the grafting length, density, and efficiency. It is also important to note that the molecular weight measurements were difficult to obtain, as AP does not fully dissolve in water and may retrograde over time. The samples were sonicated before testing to help break up any aggregates.

Table 4.5: FFF molecular weight results.

Hydrolyzed Polymer (AP-g-H-PMA)	M_n (g/mol)	M_w (g/mol)	PDI
HGP1	790,000	3,400,000	4.30
HGP2	857,000	3,760,000	4.39
HGP3	918,000	5,153,000	5.61
HGP4	791,000	2,746,000	3.47
HGP5	2,218,000	5,810,000	2.62
HGP6	1,165,000	5,422,000	4.65
HGP7	1,294,000	3,057,000	2.36
HGP8	1,367,700	2,942,000	2.15
HGP9	1,075,000	5,218,000	4.85
HGP10	1,150,000	4,308,000	3.75
HGP11	1,041,000	4,629,000	4.45

4.4 MFT Characterization

4.4.1 Dean-Stark Extraction Analysis

Dean-Stark extraction was performed on MFT samples to determine the solids, water, and bitumen content. The results of the two extractions and the standard error of the mean are presented in Table 4.6.

Table 4.6: Dean-Stark extraction MFT composition.

	Run 1	Run 2	Average	St. Error
Constituent	Wt.%	Wt.%	Wt.%	%
Solids	32.0	32.8	32.4	0.4
Water	63.3	64.3	63.8	0.5
Bitumen	4.7	2.9	3.8	0.9

4.4.2 Solids and Moisture Analysis

The results and standard error of the mean for the solids and moisture analyses are shown in Table 4.7. Comparing these results to those obtained by the Dean-Stark extraction, the solids and water content differ slightly. This variation may be due to the bitumen content in the sample as this equipment cannot measure this component. An average value of 33.8 wt. % was calculated for the solids content of the MFT based on the two characterization tests performed. This value was then used to determine the dilution requirements for the MFT flocculation study.

Table 4.7: Solids and moisture analyses.

	Run 1	Run 2	Average	St. Error
Constituent	Wt.%	Wt.%	Wt.%	%
Solids	35.46	34.86	35.16	0.30
Moisture	64.54	65.14	64.34	0.30

4.4.3 PSD Analysis

Table 4.8 shows the data acquired for the number and volume particle size distribution measurements for the MFT sample. The information in the table quantifies the size of the particles below which 10% of the sample lies (Dx 10), the size at which 50% of the sample is larger and 50% is smaller (Dx 50), and the size below which 90% of the sample lies (Dx 90). The full volume and number distributions can be seen in Figure 4.24.

Table 4.8: Mean PSD volume and number sizes.

PSD	Dx 10 (μm)	Dx 50 (μm)	Dx 90 (μm)
Mean (Volume)	2.295	9.860	35.100
Mean (Number)	0.452	0.616	1.400

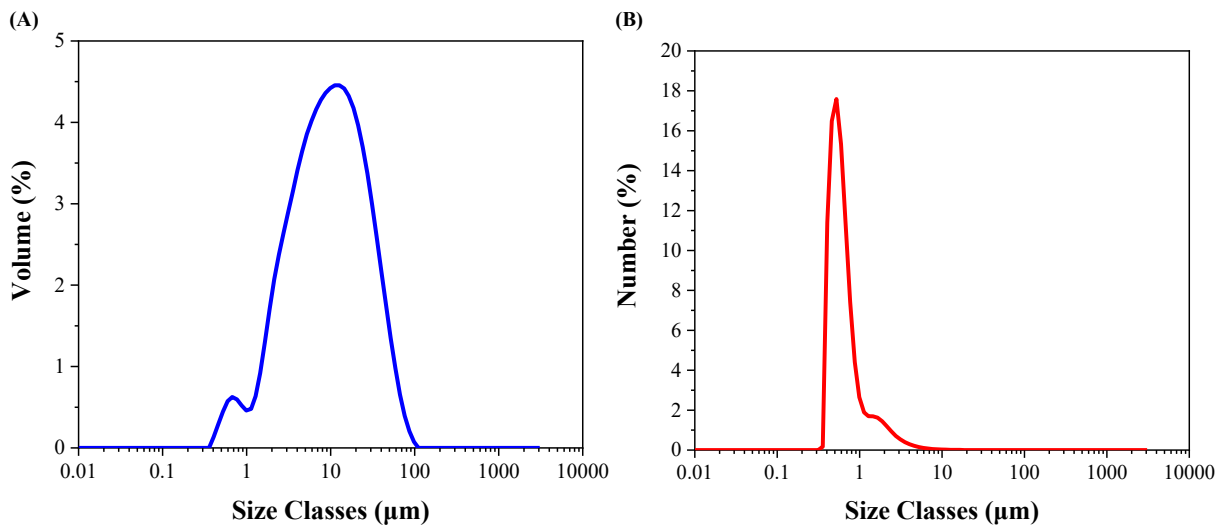


Figure 4.24: MFT volume (A) and number (B) particle size distributions.

4.4.4 AAS Analysis

The results for the concentrations of sodium, potassium, magnesium, and calcium ions in the undiluted MFT sample, as measured through atomic absorption spectrophotometry, are presented in Table 4.9. These results were recorded as the ion concentrations can influence the flocculant performance during MFT flocculation [21], [25].

Table 4.9: Major ion concentrations in an undiluted MFT sample.

Major Ion	Concentration (ppm)
Na ⁺	752.0
K ⁺	11.7
Mg ²⁺	8.8
Ca ²⁺	17.2

4.5 Effect of Graft Length, Graft Density, and Flocculant Dosage on MFT Flocculation

4.5.1 CCD Flocculation and Dewatering Results

The results of the central composite statistical design of experiments quantifying the effect of graft length ($[M]/[I]$), graft density ($[B]/[I]$), and flocculant dosage on MFT flocculation and dewatering are summarized in Table 4.10. The calculated standard error of the mean is also reported for the responses, except for ISR. The significant independent variable effects, both linear (L) and quadratic (Q), and their two-factor interactions were determined using the CCD. Based on the analysis of variance (ANOVA) performed for each dependent variable, Table 4.11 shows the statistically significant predictors. As MFT and its treatment are quite complex, a 90% confidence level was used ($p < 0.10$) to determine the statistically significant effects. Empirical models for the response variables were then created considering only the statistically significant variables. The coefficients of determination (R^2) and adjusted determination (R^2_{adj}) for each model were used to confirm their reliability. Furthermore, residual plot analyses were performed to ensure the accuracy of the models, including normal probability plots to confirm normally distributed data and predicted versus observed values plots to assess how accurate the models were at accounting for variations. The full ANOVA results for each dependent variable and further residual analyses are presented in Appendix B. With the confirmation of reliability, the produced models may be used to predict results within the range of values used in the study. Predictive response contour plots were then created using the regression models and analyzed.

Table 4.10: Summary of the CCD flocculation and dewatering results.

Run (AP-g-H-PMA)	ISR (cm/h)	CST 0h (s)	CST 24h (s)	Turbidity (NTU)	Solids content (wt.%)
HGP1-2k	8.9	55.6 ± 0.7	164.7 ± 5.5	46.0 ± 0.4	18.9 ± 0.2
HGP1-2k *	8.1	52.3 ± 0.9	145.7 ± 1.3	45.3 ± 0.4	18.3 ± 0.1
HGP1-6k	59.2	20.0 ± 0.1	35.4 ± 1.9	179.3 ± 0.7	18.3 ± 0.1
HGP1-6k *	54.6	20.1 ± 0.1	38.7 ± 1.6	171.3 ± 0.9	19.1 ± 0.2
HGP2-2k	8.9	57.5 ± 0.8	155.8 ± 2.3	46.3 ± 0.5	19.9 ± 0.6
HGP2-2k *	8.2	57.6 ± 1.8	148.9 ± 1.6	52.1 ± 0.4	19.1 ± 0.2
HGP2-6k	69.3	16.3 ± 1.4	28.2 ± 0.8	185.0 ± 1.5	17.8 ± 0.4
HGP2-6k *	68.8	16.0 ± 0.6	33.0 ± 1.6	198.3 ± 0.3	19.8 ± 0.4
HGP3-2k	9.9	50.9 ± 1.1	132.6 ± 5.1	45.3 ± 0.1	19.4 ± 1.4
HGP3-2k *	9.3	47.6 ± 0.9	128.5 ± 2.0	36.8 ± 0.7	19.1 ± 0.3
HGP3-6k	79.8	16.2 ± 0.4	27.2 ± 1.2	158.0 ± 0.0	18.3 ± 0.1
HGP3-6k *	71.7	14.6 ± 0.8	23.1 ± 0.2	164.0 ± 0.6	18.3 ± 0.3
HGP4-2k	12.9	45.1 ± 0.9	113.0 ± 1.9	66.3 ± 0.1	19.0 ± 0.0
HGP4-2k *	11.7	46.3 ± 0.3	112.6 ± 2.1	52.5 ± 0.1	19.1 ± 0.1
HGP4-6k	155.0	12.8 ± 0.1	12.8 ± 0.8	251.3 ± 0.3	17.4 ± 0.1
HGP4-6k *	158.8	12.5 ± 0.2	12.3 ± 0.2	261.3 ± 1.7	17.7 ± 0.2
HGP5-4k	34.1	27.3 ± 0.7	58.7 ± 1.5	159.0 ± 1.5	18.6 ± 0.0
HGP5-4k *	34.0	30.4 ± 0.5	62.3 ± 0.9	172.3 ± 0.3	18.2 ± 0.2
HGP6-4k	25.0	24.0 ± 0.6	65.8 ± 1.2	115.3 ± 0.3	18.6 ± 0.1
HGP6-4k *	28.3	23.2 ± 0.5	63.3 ± 2.1	127.7 ± 0.3	19.3 ± 0.5
HGP7-4k	16.1	29.6 ± 0.7	90.5 ± 3.4	104.0 ± 1.0	19.0 ± 0.3
HGP7-4k *	17.2	30.8 ± 0.1	85.9 ± 3.3	112.3 ± 0.3	18.1 ± 0.1
HGP8-4k	31.4	27.8 ± 0.5	75.4 ± 1.6	150.3 ± 0.9	19.0 ± 0.2
HGP8-4k *	30.1	27.3 ± 0.4	79.0 ± 2.0	153.0 ± 1.5	19.4 ± 0.1
HGP9-0.6k	0.1	178.7 ± 6.5	209.3 ± 2.3	11.4 ± 0.3	12.2 ± 0.0
HGP9-0.6k *	0.2	183.2 ± 9.5	204.6 ± 3.3	10.0 ± 0.7	12.6 ± 0.1
HGP9-7k	76.1	15.2 ± 0.2	26.7 ± 0.2	288.3 ± 2.8	19.1 ± 0.1
HGP9-7k *	61.4	14.1 ± 0.3	24.3 ± 0.3	278.3 ± 0.9	18.0 ± 0.0
HGP9-4k	22.8	27.2 ± 0.3	89.2 ± 3.0	104.0 ± 1.2	18.2 ± 0.2
HGP9-4k *	21.4	27.5 ± 0.8	82.4 ± 0.7	119.0 ± 0.6	18.9 ± 0.0
HGP10-4k	22.0	31.2 ± 0.5	78.6 ± 2.6	137.3 ± 1.3	18.7 ± 0.1
HGP10-4k *	21.1	33.6 ± 0.3	96.0 ± 1.7	162.7 ± 0.3	19.3 ± 0.1
HGP11-4k	23.9	26.5 ± 0.9	71.9 ± 3.7	152.7 ± 1.8	19.9 ± 0.5
HGP11-4k *	25.7	27.1 ± 0.2	70.5 ± 1.7	167.7 ± 0.9	19.1 ± 0.1

* Replicate run

Table 4.11: Overview of the significant factors for each response.

Predictors	ISR	CST 0h	CST 24h	Turbidity	Solids Content
X_1 : [M] (L)	✓	✓	✓	✓	✗
[M] (Q)	✗	✗	✗	✓	✗
X_2 : [B] (L)	✓	✓	✓	✗	✗
[B] (Q)	✓	✓	✓	✗	✗
X_3 : Polymer dosage (L)	✓	✓	✓	✓	✓
Polymer dosage (Q)	✗	✓	✓	✗	✓
1L by 2L	✓	✗	✗	✓	✗
1L by 3L	✓	✓	✗	✓	✗
2L by 3L	✓	✓	✓	✗	✗

Significant ✓, Not significant ✗

4.5.2 Initial Settling Rate (ISR)

The initial settling rate data were transformed by taking the square root of the results to obtain a high correlation for the data and normally distributed residuals. From the ANOVA, it was found that all the variables were significant, except the quadratic monomer concentration and flocculant dosage effects. Table 4.12 shows the final empirical model according to the coded factors considering only statistically significant coefficients ($p < 0.10$) and the corresponding R^2 and R^2_{adj} values. Figure 4.25 shows that the model adequately meets the regression assumptions as the residuals are normally distributed and the randomly scattered observed points fall close to the predicted 45° line.

Table 4.12: ISR model equation.

Model	$Y = 5.12 + 0.55X_1 + 0.37X_2 + 0.44X_2^2 + 2.77X_3 + 0.43X_1X_2 + 0.52X_1X_3 + 0.58X_2X_3$
Coefficient of determination	$R^2 = 0.904$
Adjusted coefficient of determination	$R_{adj}^2 = 0.878$

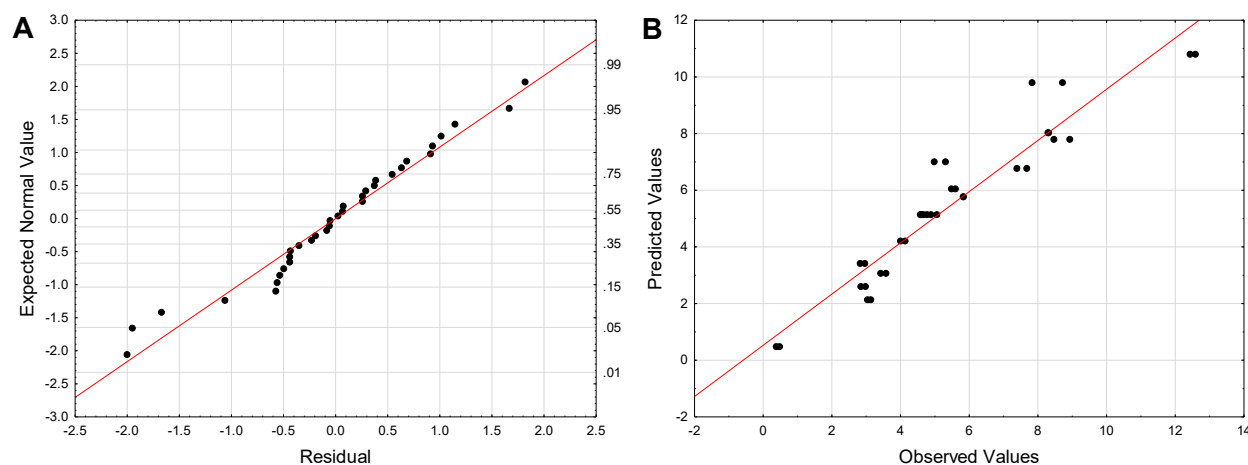


Figure 4.25: A) Normal probability plot, and B) Predicted versus observed values for the ISR model.

The predictive response surfaces for the square root of the ISR ($\sqrt{\text{ISR}}$) based on the regression model are shown in Figure 4.26. All the plots were created with the fixed variable at its centre point (0). The desirable areas where faster settling occurs are the red regions, as they are associated with high $\sqrt{\text{ISR}}$ values. Figure 4.26A shows the $\sqrt{\text{ISR}}$ as a function of amylopectin concentration (graft density) and methyl acrylate concentration (graft length). The flocculant performed best (high ISR) when both concentrations were high (upper right quadrant). Figure 4.26B and Figure 4.26C show the response as a function of dosage and methyl acrylate concentration, and dosage and amylopectin concentration, respectively. In both plots, higher dosages (≥ 4 kppm) at higher monomer or backbone concentrations resulted in faster settling. At the lower dosages, the differences in polymer structure appeared to make little difference in the

resulting ISR. The most likely underlying flocculation mechanisms for this polymer are salt linkages and the bridging mechanism, though some electrostatic interactions may occur. This occurs mainly due to the salt bridges formed from using positively charged calcium ions between the negatively charged MFT clay particles and the negatively charged grafted chains; however, the neutral amylopectin may also undergo bridging. As well, even though the overall charge of the clays are negative, some electrostatic attraction may occur between the polymer and local patches of cationic charge on the mineral surfaces [29].

Combining these findings, the optimal settling conditions occurred when the graft copolymer flocculants had long grafted chains (high $[M]$) with a low grafting density (high $[B]$) and were used at higher dosages. This agrees with previous natural graft copolymer studies as it has been noted that fewer but longer chains resulted in better flocculation [71]. Longer chains result in polymers that can extend farther into the solution and attach to more clay particles. In turn, larger and heavier flocs are formed, which settle faster under gravity [130]. Furthermore, longer chains allow the flocculant to form stronger bridges, as longer segments can have several points of contact amongst the clay particles [25]. Interestingly, with longer graft chains a lower grafting density was better than a higher grafting density. Despite having more graft chains available, it is hypothesized that the negative charges on the grafts may interfere and repel each other if positioned too close together on the backbone. Some electrostatic repulsion between the polymer segments is beneficial to bridging, as the chains have a more extended conformation [131]. However, if the chains are positioned too closely, they may not be able to extend away from each other. Instead, the straightening and rigidity of the chains may reduce their approachability to the contaminants and reduce the flocculation ability [116]. Moreover, this reduced performance could be due to the ratio of synthetic chains to natural backbone. Generally, increasing the amount of backbone ultimately increases the settling rate, particularly as the grafted chain length increases. As the synthetic chains are more susceptible to shear breakage, flocs formed with these flocculants may have been disrupted more than those with a higher backbone content. It should be noted that for shorter chains, the polymers were likely more compact and not able to extend very far into the solution. As such, less bridging and contaminant entrapment could occur due to their limited approachability, consequently creating smaller flocs which settled more slowly. In addition, all graft copolymers had poor performance at low dosages, particularly the lowest dosage tested (0.636 kppm), likely due to there being insufficient polymer to initiate floc formation. In the

empirical model in Table 4.12, the coefficient with the largest value is associated with the linear dosage effect, thus showing that the results are largely dependent on the dosage used.

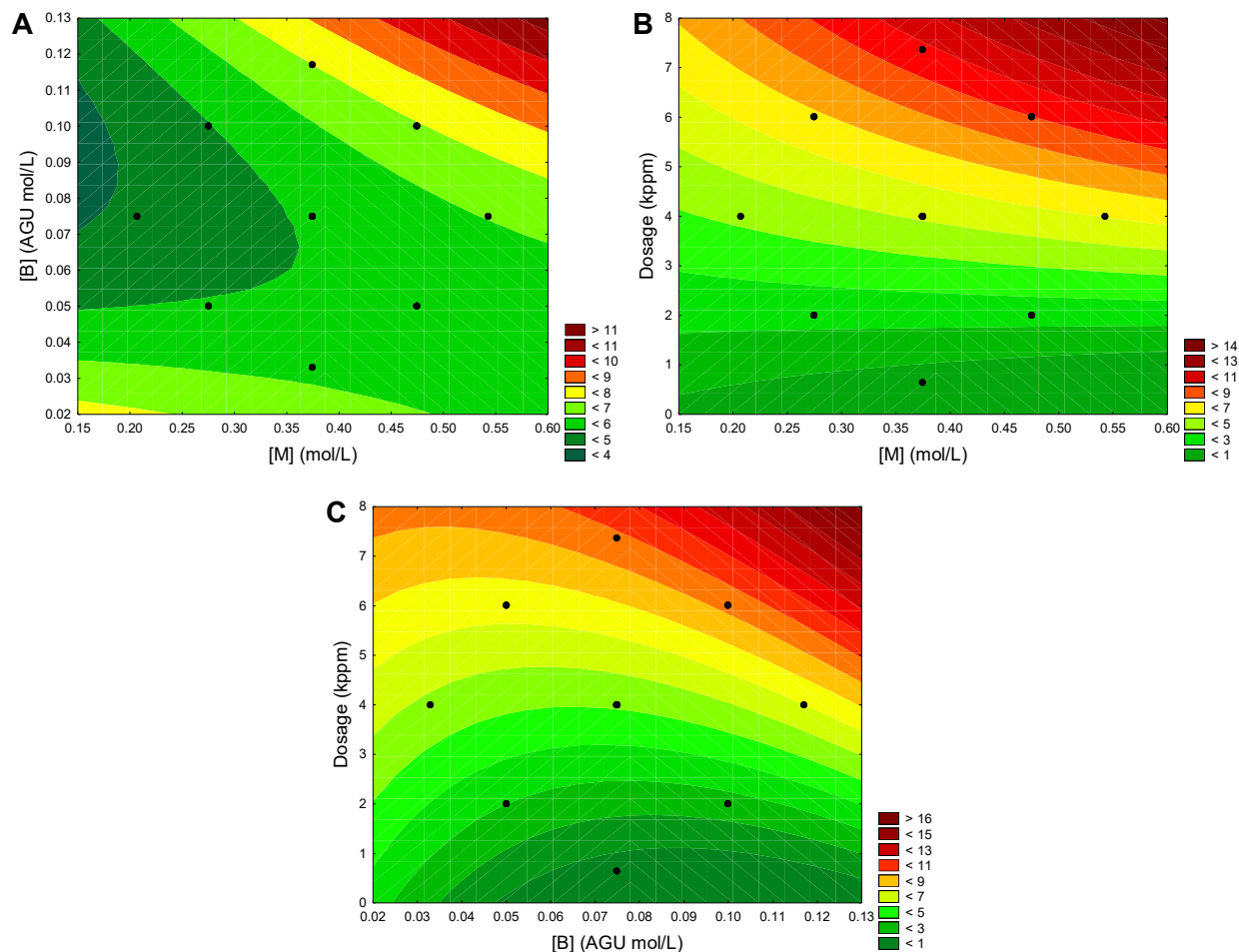


Figure 4.26: Response surfaces for \sqrt{ISR} .

4.5.3 Initial CST

Like the ISR, the initial CST (CST 0h) data were transformed by taking the reciprocal of the results to attain normally distributed residuals and a correlation with better prediction capability. Furthermore, the ANOVA showed that all variables were significant, except the effects for the quadratic monomer concentration and the interaction between methyl acrylate and amylopectin. Table 4.13 shows the final empirical model according to the coded factors, including

only statistically significant coefficients, as well as the R^2 and R^2_{adj} values. Figure 4.27 also confirms that a correlation exists between the variables and the responses.

Table 4.13: Initial CST model equation.

Model	$Y = (3.59 \times 10^{-2}) + (2.36 \times 10^{-3})X_1 + (3.78 \times 10^{-3})X_2 + (2.09 \times 10^{-3})X_2^2 + (2.08 \times 10^{-2})X_3 + (1.50 \times 10^{-3})X_3^2 + (3.25 \times 10^{-3})X_1X_3 + (3.28 \times 10^{-3})X_2X_3$
Coefficient of determination	$R^2 = 0.965$
Adjusted coefficient of determination	$R^2_{adj} = 0.956$

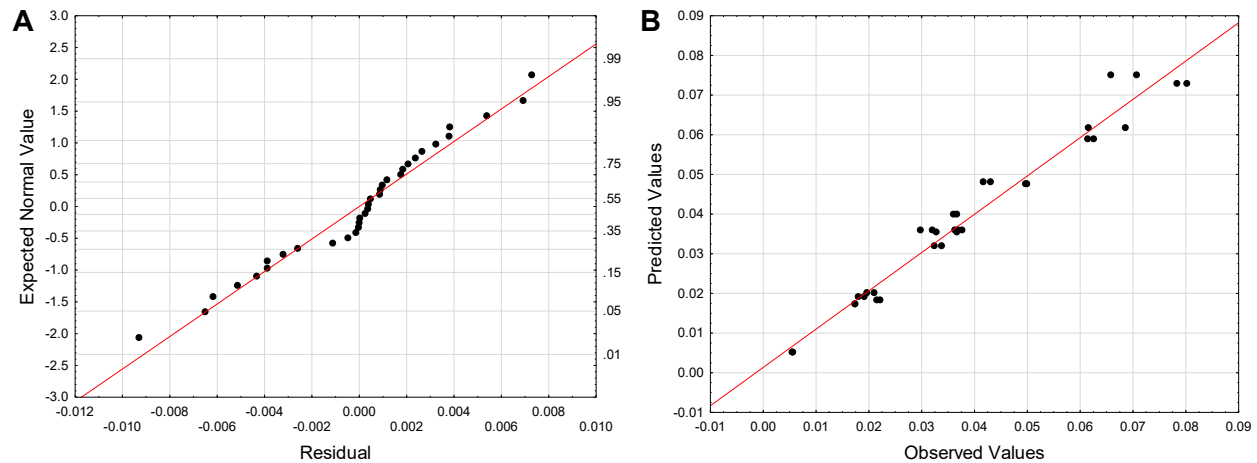


Figure 4.27: A) Normal probability plot, and B) Predicted versus observed values for the initial CST model.

The predictive contour plots for the reciprocal of the initial CST, $(\text{CST } 0\text{h})^{-1}$, based on the model are shown in Figure 4.28. All plots were formed with the fixed variable at its centre point (0). For the CST values, shorter times mean faster floc dewaterability. In the plots, high values of $(\text{CST } 0\text{h})^{-1}$ represent desirable dewaterability and are noted by the red areas. Figure 4.28A shows how $(\text{CST } 0\text{h})^{-1}$ depends on the amylopectin (graft density) and methyl acrylate (graft length) concentrations. The best dewaterability was attained at both high backbone and high monomer

concentrations (upper right quadrant). This again relates to graft copolymer flocculants with a lower number of long grafted chains. Long chains likely allowed the polymers to trap more clay particles, producing larger and denser flocs. As denser flocs inherently retain less water, the dewatering times were ultimately lower than for the flocculants with short chains [25]. An explanation as to why the higher grafting densities, particularly for the flocculants with longer chains, resulted in reduced performance may be related to the rigidity and repulsive nature due to the proximity of chains which, in turn, hinder the flocculation process. Even though the low grafting density was advantageous for the range tested in this study, there may be a limit outside this range where too much space between the grafts could hinder the performance.

Figure 4.28B and Figure 4.28C show surface responses as a function of flocculant dosage and monomer concentration, and flocculant dosage and backbone concentration, respectively. These figures also show that the best performance occurred in the upper right quadrant. For any given concentration of amylopectin or methyl acrylate, higher dosages improved initial CST times. As more graft copolymer is available for bridging at higher dosages, larger flocs can, therefore, be formed. When these flocs are formed, large pores exist between them that allow water to pass through easily, ultimately dewatering the mixture faster. Additionally, based on the empirical model found in Table 4.13, the initial CST was significantly dependant on the dosage as the linear dosage effect had the largest coefficient value.

Notably, the predictive surface plots for the initial CST followed almost identical trends to those for the ISR. This was expected as the settling is also generally related to how large the flocs are and how fast they can release water.

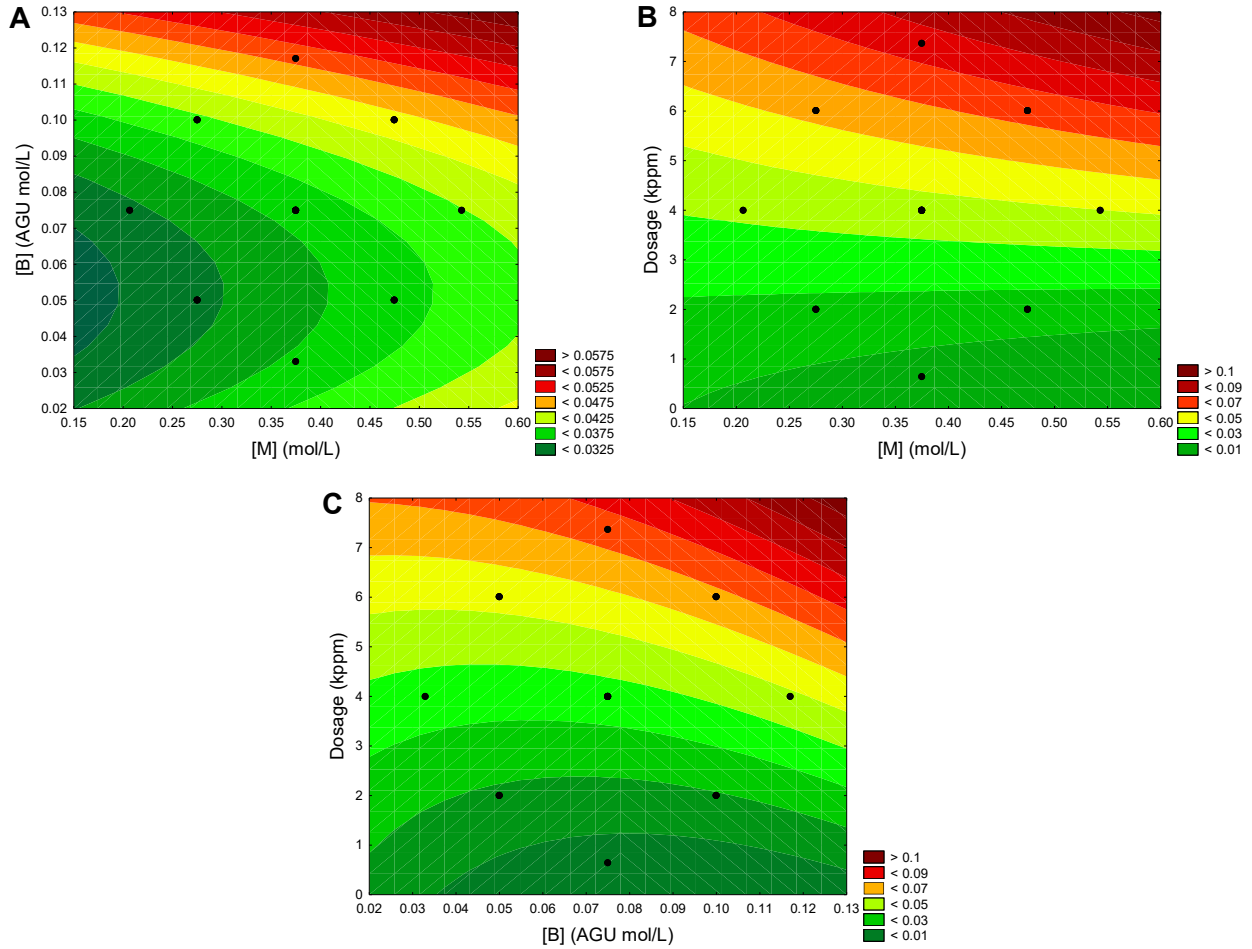


Figure 4.28: Response surfaces for $(\text{CST } 0\text{h})^{-1}$.

4.5.4 Sediment CST

Like the ISR and initial CST, the ANOVA results for the sediment CST after 24 hours (CST 24h) showed that all variables were significant, except for the quadratic monomer concentration, the interaction between monomer and backbone concentrations, and the interaction between monomer concentration and flocculant dosage. Table 4.14 shows the final empirical model according to the coded factors containing only statistically significant coefficients, as well as the values of R^2 and R^2_{adj} . Figure 4.29 further indicates a normal distribution and generally follows the assumptions of the regression analysis.

Table 4.14: Sediment CST model equation.

Model	$Y = 80.81 - 4.26X_1 - 6.40X_2 - 7.68X_2^2 - 54.97X_3 + 11.31X_3^2 + 4.28X_2X_3$
Coefficient of determination	$R^2 = 0.976$
Adjusted coefficient of determination	$R_{adj}^2 = 0.970$

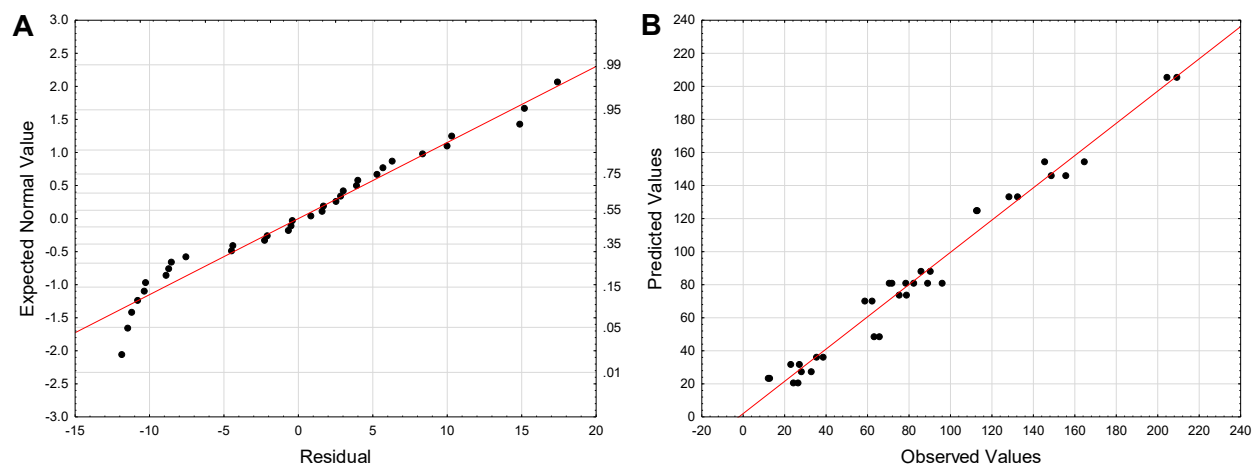


Figure 4.29: A) Normal probability plot, and B) Predicted versus observed values for the sediment CST model.

The predictive response contour plots for the sediment CST based on the empirical model are shown in Figure 4.30. All the surfaces were developed with the fixed variable at its centre point (0). As this response variable was not transformed, the low values, which correlate to better performance, are indicated by the green areas. Figure 4.30A shows CST 24h as a function of amylopectin concentration (graft density) and methyl acrylate concentration (graft length). The best results were observed in the upper portion of the plot with a slight emphasis on the right half. After 24 hours of settling, the flocs appeared to maintain their structure and dewaterability, as this result mirrors the ISR and initial CST trends. This finding reiterates that the best performing graft copolymers had longer and more spaced out grafted chains. Although the effect of monomer concentration (graft length) on the sediment CST is not substantial, it is clear from the negative

coefficient in the equation and the trend in the contour plot that increasing the graft length lowers the CST. Looking at the plot and the empirical model, the backbone appears to have a greater effect on lowering the sediment CST than the monomer. Compared to the coefficient for the linear monomer effect, the coefficients for the linear and quadratic backbone effects are more negative. Thus, increasing the amount of backbone generally decreases the response to a much greater degree.

Figure 4.30B and Figure 4.30C show the response as a function of dosage and monomer concentration, and dosage and backbone concentration, respectively. In both cases, increasing the dosage had a great impact on decreasing the resulting sediment CST. This is reflected through the large negative linear coefficient term in the model equation. As noted for the initial CST, it appears that higher dosages allow for more bridging, larger flocs, and more porous sediments. Furthermore, according to the ISR, initial CST, and sediment CST results, the graft copolymers did not appear to show signs of overdosing in the range of dosages tested (0.636–7.364 kppm).

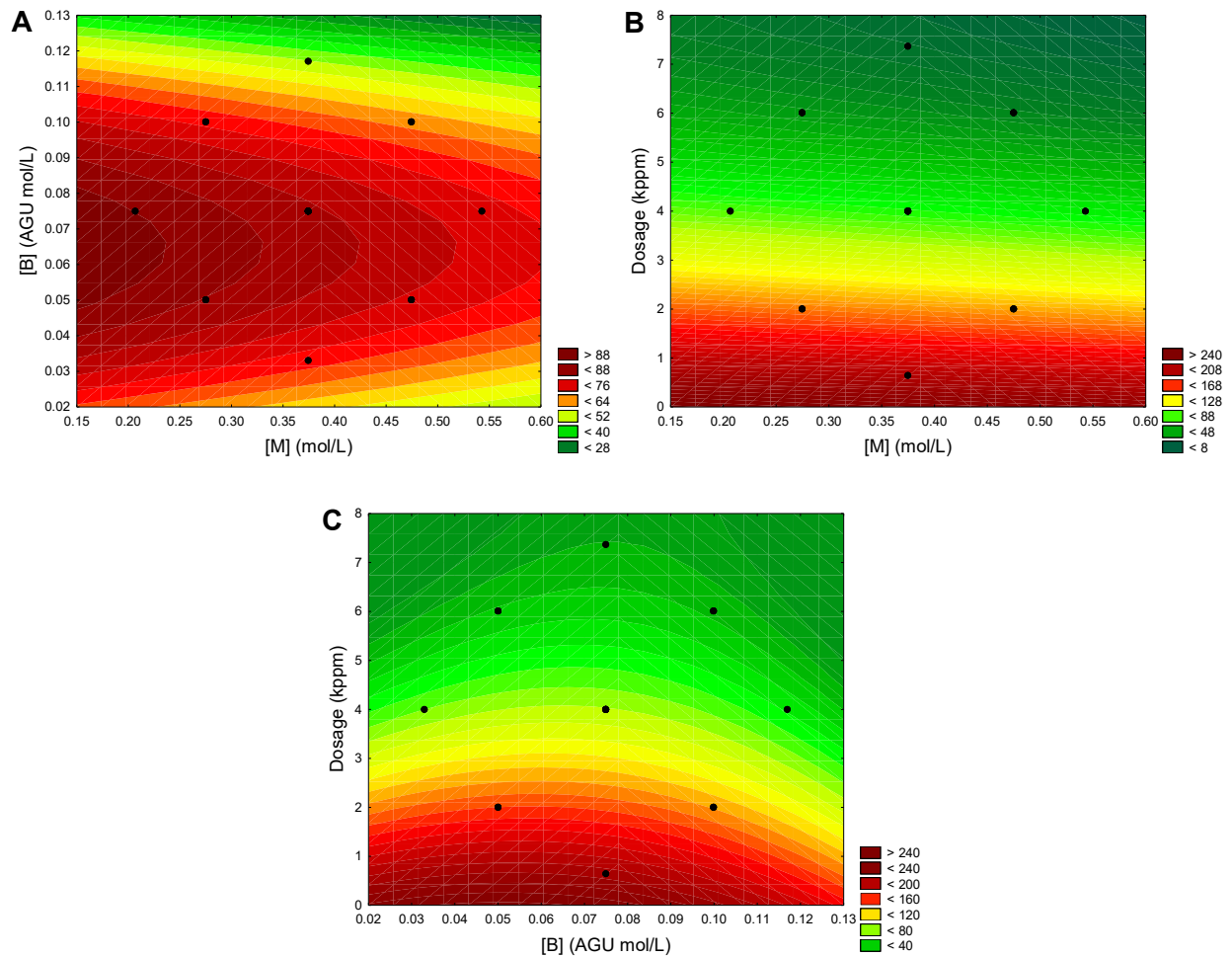


Figure 4.30: Response surfaces for CST 24h.

4.5.5 Supernatant Turbidity

The ANOVA results for the supernatant turbidity showed that the linear and quadratic backbone concentration effects were not significant. Similarly, the quadratic dosage effect and the interaction effect of the dosage and backbone concentration were also not statistically significant. Table 4.15 shows the final empirical model according to the coded factors comprising of statistically significant coefficients only and the corresponding R^2 and R^2_{adj} values. Figure 4.31 shows that the model is quite accurate as the residuals are normally distributed and there is a strong correlation between the predictions and actual results.

Table 4.15: Turbidity model equation.

Model	$Y = 137.27 + 15.15X_1 - 6.69X_1^2 + 76.70X_3 + 11.73X_1X_2 + 11.21X_1X_3$
Coefficient of determination	$R^2 = 0.942$
Adjusted coefficient of determination	$R_{adj}^2 = 0.931$

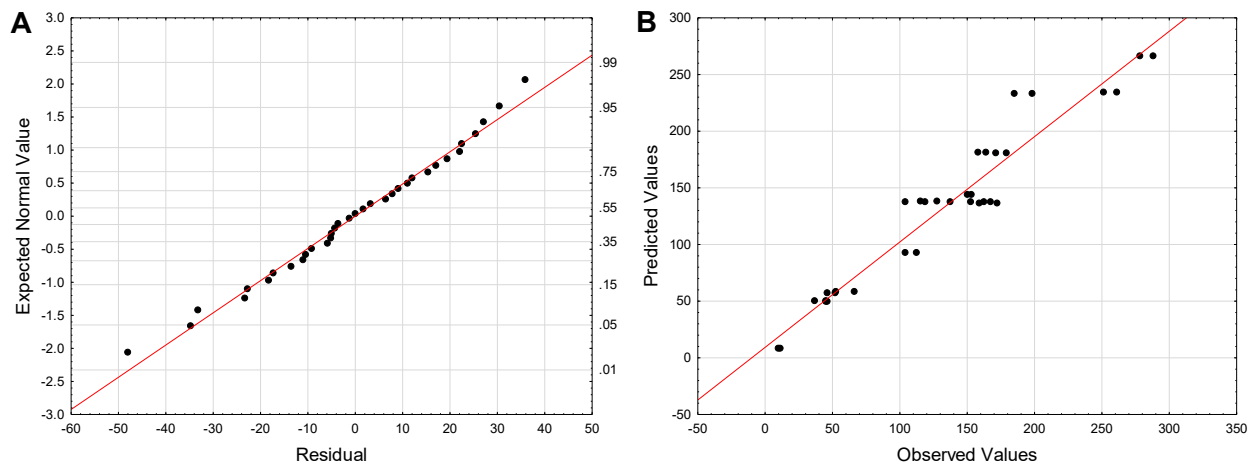


Figure 4.31: A) Normal probability plot, and B) Predicted versus observed values for the Turbidity model.

The predictive surface plots for the turbidity based on the regression model are shown in Figure 4.32. The surfaces were developed with the fixed variable at its centre point (0). As clearer released water results in low turbidity values, the green areas in the plots display desired responses. Figure 4.32A shows turbidity as a function of amylopectin concentration (graft density) and methyl acrylate concentration (graft length). The main variable affecting the supernatant turbidity is undoubtedly the methyl acrylate concentration, although according to the model equation there is also a statistically significant interaction between the monomer and backbone concentration variables. At the 4 kppm dosage, the turbidity decreased almost linearly as the graft length was increased. It may be speculated that as the graft lengths increase and more negative charges are present, the longer negatively-charged chains may interfere with each other, hindering their adsorption ability onto the smaller suspended particles and resulting in less fines capture.

Figure 4.32B and Figure 4.32C show the surface response as a function of dosage and monomer concentration, and dosage and backbone concentration, respectively. The figures show that lower dosages resulted in better performance concerning turbidity, particularly for the flocculants with shorter grafted chains. For the graft copolymers tested in this study, it seems that their performance at high dosages regarding settling (ISR) and dewatering (initial and sediment CST) yielded good results, however, they also produced more turbid supernatants. This contrasting result may be explained by the size of the flocs formed. As the larger flocs formed at higher dosages are heavier and settle much quicker, the polymers may not have adequate time to capture all the fine particles [25]. Furthermore, it is possible that the interaction of the negatively charged grafted chains, particularly for the flocculants with longer grafts, is amplified at higher dosages, thus worsening its ability to trap fines.

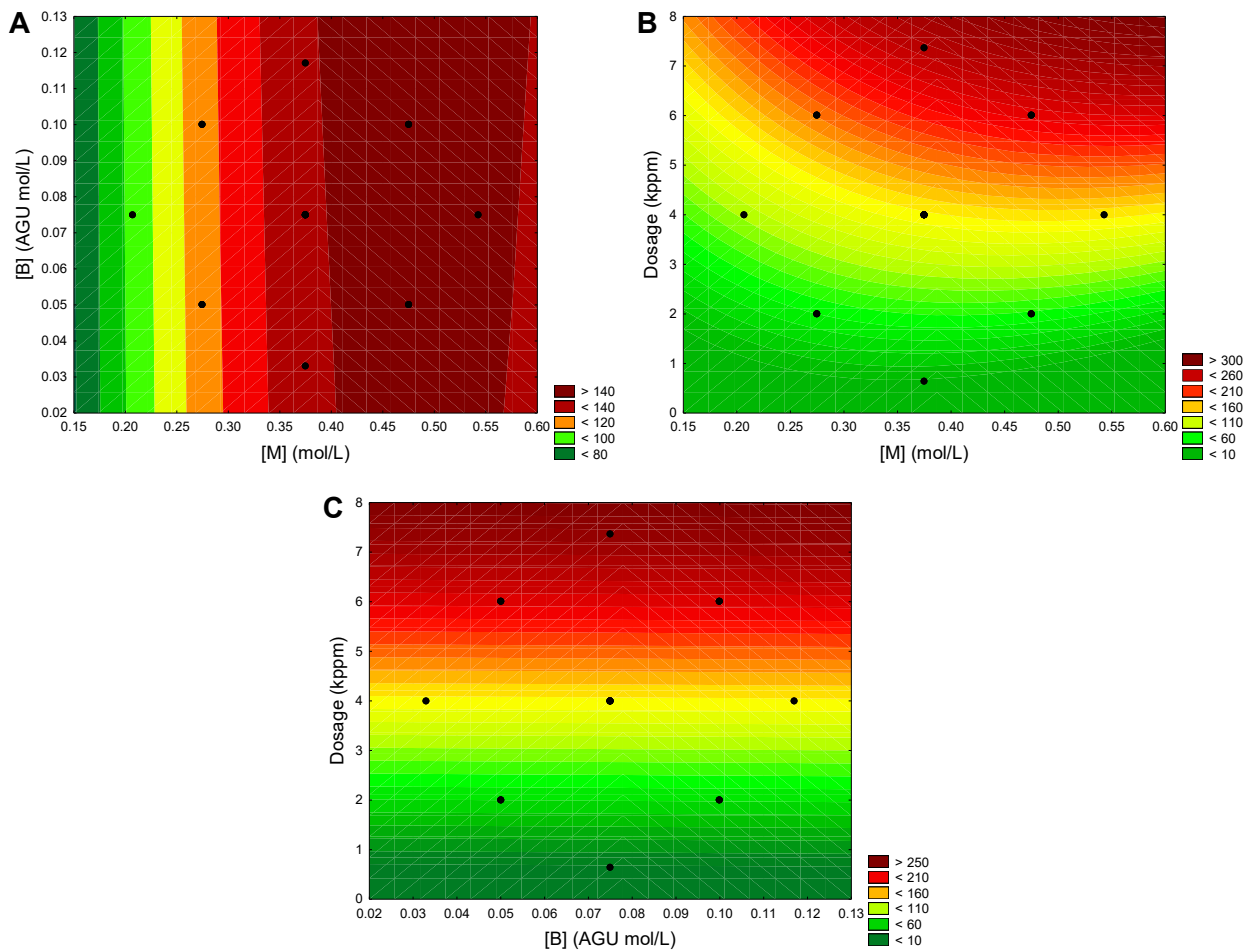


Figure 4.32: Response surfaces for Turbidity.

4.5.6 Solids Content

The ANOVA results for the solids content indicated that the only significant effects were the linear and quadratic dosage effects. Despite this, no statistically significant model could be created as the residual analysis did not meet the regression assumptions and the R^2 and R^2_{adj} values were very low, 0.424 and 0.387, respectively. The inability to create a significant model was likely due to the small range of results and large variations in the replicates. As all the tested flocculants in this CCD caused the MFT to settle to the same approximate level in the cylinders, it makes sense that their solids contents did not differ significantly.

4.6 Comparison Testing

4.6.1 Benchtop Flocculation Comparison Tests

The flocculation and dewatering results of the benchtop comparison tests are presented in Figure 4.33. Figure 4.33A shows the initial settling rate (ISR) results, Figure 4.33B and Figure 4.33C display the initial (0 h) and sediment (24 h) capillary suction times (CST), respectively, Figure 4.33D presents the supernatant turbidities, and Figure 4.33E shows the solids content comparison. The full dosage series results can be found in Appendix C.

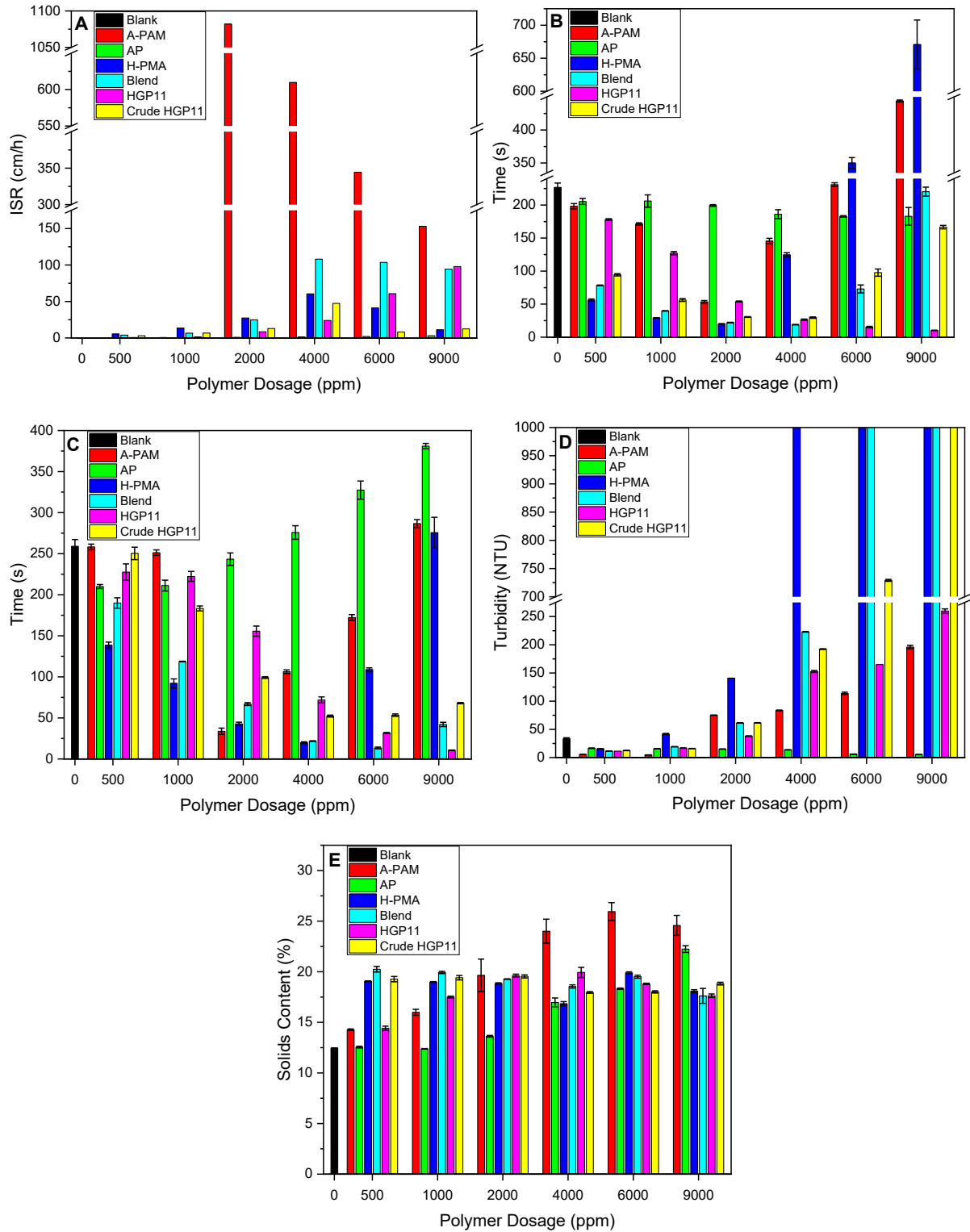


Figure 4.33: A) ISR comparison, B) Initial CST comparison, C) Sediment CST comparison, D) Turbidity comparison and E) Solids content comparison.

In Figure 4.33A, the 0 ppm dosage shows that in the first hour, settling essentially did not happen for the calcium blank test. Comparing this to the other dosages, adding the polymer flocculants clearly increased MFT settling. However, the entire AP series showed very little settling in the first hour, resulting in very low ISRs that are practically indistinguishable in the figure. As AP has a lower molecular weight than the other polymers, it was expected that the flocs formed would be significantly smaller and slower to settle. At the lower dosages, the ISRs were very low for all the tested polymers. At 2000 ppm, the A-PAM reached its optimum ISR value of 1082 cm/h and settled the fastest when compared to the other polymers. As the molecular weight of A-PAM was significantly higher than the others, it made sense that it reached its optimum ISR at a lower dosage. However, increasing the A-PAM dosage further had a negative impact on ISR, likely due to overdosing. Overdosing is a significant problem in the industry as staying within a narrow optimal dosage window may not be practicable. Even though the other polymers did not settle as fast as A-PAM, their settling rates were still acceptable. The optimal dosage for H-PMA, the blend, and crude HGP11 all occurred at approximately 4000 ppm and their optimal ISRs were 60, 108, and 47 cm/h, respectively. Interestingly, the blend had the highest ISR of this group likely due to interactions and bridging with AP improving floc formation. At higher dosages, these polymers also seemed to overdose, but the blend experienced this to a lesser degree. In the range tested, the ISR for HGP11 continued to increase reaching a maximum value of 98 cm/h at 9000 ppm. Despite the fact that higher dosages were required for faster settling, no overdosing was apparent. Notably, previous studies have observed that the homopolymers formed in the grafting reaction have lower molecular weights than the grafted chains [97]. This may be an explanation as to why crude HGP11 did not perform as well as the purified HGP11. Furthermore, as HGP11 is chemically grafted, it may have a higher shear resistance when compared to H-PMA, the blend, and crude HGP11. This can be examined in a future work with focused beam reflectance measurements to monitor the changes in floc size when exposed to shear. Overall, the optimum ISR achieved by HGP11 is consistent with the optimum of the blend and exceeds the optimums for the H-PMA and AP homopolymers. Even though it did not settle as fast as A-PAM, HGP11 did not show signs of overdosing within the range tested.

In Figure 4.33B, the initial CST at 0 ppm for the calcium blank solution is approximately 227 s. This slow initial dewatering parallels the ISR as calcium alone is only able to coagulate the particles in MFT creating micro flocs. The coagulation likely resulted in tightly packed sediments

with small pores that scarcely allowed water to be released. Adding the polymer flocculants improved dewatering as the initial CSTs noticeably decreased with their addition. The use of the neutral AP slightly improved the CST, particularly at higher dosages, but the optimum value achieved was still rather high (~ 183 s) and not acceptable in industry. More acceptable values were reached by the other flocculants tested. H-PMA, the blend, and crude HGP11 follow relatively similar trends, reaching their optimums in the middle of the dosage range tested (20, 19, and 30 s, respectively). These polymers performed significantly better than the others at the lowest dosages; however, they showed signs of overdosing past their optimum values. The H-PMA homopolymer experienced this the most, as dosages over 4000 ppm resulted in higher CST values than the calcium blank test. This may be a result of electrosteric repulsion and re-stabilization of the suspension caused by an excess of negative charge or an excess of polymer leading to insufficient particle surface for attachment. A-PAM seemingly also faced this problem, as the CST substantially increased (53 s at 2000 ppm to 444 s at 9000 ppm) at dosages higher than its optimum. A-PAM formed very large and gel-like flocs and as such, the effect of overdosing and water retention due to hydrogen bonding may have caused reduced dewatering [53]. The CST behaviour of HGP11 mirrors its ISR performance, reaching an optimum value of about 10 s at 9000 ppm, with no signs of overdosing. Interestingly, for almost every case tested, the initial CSTs for HGP11 were noticeably better than for the commercial A-PAM. Furthermore, the optimum initial CST achieved by HGP11 outperformed the optimums for the other polymers tested.

The sediment CST results presented in Figure 4.33C show the same general trends as for the initial CSTs. The biggest difference between Figure 4.33B and Figure 4.33C occurs for AP. Although the trend for the initial CST for AP is quite steady, with a minor improvement at higher dosages, the CST trend is opposite for the sediments after 24 hours. This may be due to greater compaction of the flocs formed by AP at higher dosages, as AP did not flocculate or settle effectively at dosages lower than 4000 ppm. Above 4000 ppm, AP was able to form very small flocs, which after 24 hours of settling likely resulted in densely packed sediments with narrow channels for water to pass through. As the sediments at higher dosages also retained less water, confirmed by the increase in solids content (Figure 4.33E), the dewatering ability was ultimately lowered. Comparing the other polymers, the optimum value reached for A-PAM was about 34 s at 2000 ppm, while the optimal values for H-PMA, the blend, and crude HGP11 shifted to slightly higher dosages. The optimum values reached for H-PMA and crude HGP11 were 43 and 52 s,

respectively at 4000 ppm, while the blend achieved a time of about 13 s at 6000 ppm. Once again, the optimum for HGP11 performed the best of all the optimums obtained by the polymers, with an approximate time of 11 s at 9000 ppm.

Based on the turbidities in Figure 4.33D, AP generally outperformed the other flocculants as the resulting supernatant fluid was very clear for the entire dosage range tested (< 20 NTU). This was expected as the tiny flocs formed by AP settle very slowly, allowing more time for the polymer to adsorb onto the fines in the suspension. Unlike AP, the other flocculants reached their optimums at the lower dosages and showed trends of increasing turbidity as the dosage was increased. This increasing trend was expected as larger flocs settle faster and generally are unable to capture all the fine particles. As transparent supernatants are desirable, turbidity values greater than 1000 NTU were not included in the figure (refer to Appendix C for comprehensive results). This increase is most severe for H-PMA as the turbidity jumped to over 1000 NTU at dosages higher than 2000 ppm. The drastic increase was also probably due to overdosing and re-stabilization. This sizeable turbidity increase was also observed for the blend and crude HGP11. The turbidities for HGP11 and A-PAM increased to a much lesser degree at the higher dosages. However, it was observed for A-PAM that a noticeable amount of polymer remained in the supernatant at dosages above 2000 ppm making the substance viscous and likely unusable as recycled water for industrial applications.

In Figure 4.33E, the solids content of the sediments after 24 hours generally show that flocculant addition is required to create compact sediments with higher solids contents. In the figure, the calcium blank test only increased the original suspension solids content from 10% to 12.5%. Apart from AP, which did not appear to have an effect until about 4000 ppm, the addition of the other polymers increased the solids content at all dosages. At the lowest dosages (500 and 1000 ppm), the solids contents for HGP11 were slightly lower than for H-PMA, the blend, and crude HGP11, but as the dosage increased, the solids contents achieved by these polymers were all quite consistent and nearly double that of the original suspension. This made sense as in the cylinders they all settled to about the same level. A-PAM achieved the highest solids content of all the polymers, approximately 26%, at 6000 ppm. Nevertheless, as the CST provides complementary evidence on the ease of dewatering, the results showed that though less water may be retained in these sediments, it is much more difficult to remove the trapped water than for the

other polymers [53]. As the CST results for HGP11 showed better dewaterability, a centrifugation or filtration step may improve upon the solids content results for this flocculant.

5. Conclusions and Future Work

Although amylopectin graft copolymers have been studied previously, their use to flocculate oil sands mature fine tailings has rarely been reported. In particular, the use of amylopectin-*graft*-hydrolyzed-poly(methyl acrylate) on MFT has not been published and was, therefore, the focus of this work.

A central composite design of experiments was used to synthesize and test different grades of AP-*g*-H-PMA as flocculants for MFT samples diluted to 10 wt.% solids. Before hydrolysis, a purification step was necessary to remove the unwanted PMA homopolymers formed during the reaction and to calculate various grafting parameters. To determine if the grafting reaction was successful, FTIR, NMR, TGA, and HiM techniques were used on the purified products. The final hydrolyzed flocculants were also analyzed with the FTIR and FFF.

In the FTIR and ^{13}C NMR results, the AP-*g*-PMA showed characteristics of both AP and PMA, but no differentiating peaks could be used to distinguish the AP-*g*-PMA from the AP-PMA blend. On the other hand, the ^1H NMR and TGA results showed some notable differences for AP-*g*-PMA when compared to the blend and the homopolymers, suggesting the grafting reaction was successful. The HiM results further supported this as the morphology of AP-*g*-PMA significantly differed from AP, PMA, and the AP-PMA blend. The FFF showed increased molecular weights compared to AP and the hydrolysis was also deemed successful, as the FTIR revealed carboxylate peaks were present.

The CCD showed that in the specific range tested, all the independent variables including, the graft length ($[M]/[I]$), graft density ($[B]/[I]$), and flocculant dosage, were statistically significant and influenced the flocculation metrics. Regarding settling and dewatering (ISR, initial CST, and sediment CST), the AP-*g*-H-PMAs with longer chains and lower grafting densities had superior performance, especially at high dosages, though a slight trade-off was observed for the turbidity. The comparison tests showed the polymer flocculants more efficiently settled and dewatered the MFT suspension than calcium alone. Although AP itself did not perform well, AP-*g*-H-PMA had enhanced flocculation ability, and at its optimum dosage generally performed better than its constituting homopolymers (AP and H-PMA). At its optimum dosage, it outperformed a

commercial anionic polyacrylamide (A-PAM) for many of the flocculation metrics and unlike A-PAM, it generally did not experience the negative effects of overdosing in the dosage range tested.

The AP-g-H-PMAs appeared to be susceptible to some retrogradation after being left in solution for some time, likely due to solubility issues with AP. This made molecular weight measurements difficult as AP never fully dissolved in water and retrograded over time. In future studies, a different natural backbone polymer with better solubility could be used such as hydroxypropyl methylcellulose (HPMC).

Although AP-g-H-PMA as a natural graft copolymer flocculant showed some promising results, future work can be done to improve its performance. A possible way to better control the molecular weight, graft length, grafting density, and improve the grafting efficiency may be by creating a macro-initiator by functionalizing the AP backbone and then grafting through an atom transfer radical polymerization (ATRP). Not only is ATRP more controllable than a free radical polymerization, but homopolymer formation is essentially eliminated, thus removing the need for a purification step. Furthermore, as a complete hydrolysis was performed for this study, the charge density was not optimized. Future studies should work towards a controllable partial hydrolysis to evaluate the effect of charge density on the flocculation performance as some hydrophobic moieties may improve the dewaterability and trap more of the bitumen and organic matter in the MFT. Additional future work may also include synthesizing and comparing AP grafted with cationic monomers, such as (vinylbenzyl)trimethylammonium chloride (VB), to eliminate the need for calcium ion addition. Finally, the optimized flocculant should be tested on undiluted MFT, on a larger scale, and over a longer time period to evaluate long-term dewatering.

References

- [1] C. J. Cleveland and C. Morris, “Oil Sands Economic contributions,” 2016.
- [2] N. R. Canada, “Oil Resources,” 2016. [Online]. Available: <https://www.nrcan.gc.ca/energy/oil-sands/18085>. [Accessed: 01-Oct-2019].
- [3] “Energy resources: facts and stats - Open Government,” 2017. [Online]. Available: <https://open.alberta.ca/dataset/energy-resources-facts-and-stats>. [Accessed: 01-Oct-2019].
- [4] J. H. Masliyah, Z. Xu, and J. A. Czarnecki, “Chapter 1: Introduction to the Athabasca Oil Sands,” in *Handbook on Theory and Practice of Bitumen Recovery from Athabasca Oil Sands. Volume 1: Theoretical Basis*, Kingsley Knowledge Publishing, 2011, pp. 1–39.
- [5] M. Humphries, “North American oil sands: History of development, prospects for the future,” in *Canada: Background and U.S. Relations*, Nova Science Publishers, Inc., 2010, pp. 163–186.
- [6] “Surface Mining Techniques used in the Oil Sands.” [Online]. Available: <https://www.oilsandsmagazine.com/technical/mining/surface-mining>. [Accessed: 01-Oct-2019].
- [7] “Oil Sands 101: Process Overview.” [Online]. Available: <https://www.oilsandsmagazine.com/technical/oilsands-101>. [Accessed: 01-Oct-2019].
- [8] T. Hirsch, “Treasure in the sand: An overview of Alberta’s oil sands resources,” Canada West Foundation, Calgary, AB, 2005.
- [9] “In-Situ Bitumen Extraction.” [Online]. Available: <https://www.oilsandsmagazine.com/technical/in-situ>. [Accessed: 01-Oct-2019].
- [10] “Canada’s Oil Sands.” Canadian Association of Petroleum Producers, pp. 1–31, 2018.
- [11] “Oil Sands Geology & the Properties of Bitumen,” 2016. [Online]. Available: <https://www.oilsandsmagazine.com/technical/properties>. [Accessed: 01-Oct-2019].
- [12] E. W. Allen, “Process water treatment in Canada’s oil sands industry: I. Target pollutants and treatment objectives,” *J. Environ. Eng. Sci.*, vol. 7, no. 2, pp. 123–138, 2008.
- [13] Q. Lu, B. Yan, L. Xie, J. Huang, Y. Liu, and H. Zeng, “A two-step flocculation process on oil sands tailings treatment using oppositely charged polymer flocculants,” *Sci. Total Environ.*, vol. 565, pp. 369–375, Sep. 2016.
- [14] J. Masliyah, Z. J. Zhou, Z. Xu, J. Czarnecki, and H. Hamza, “Understanding Water-Based Bitumen Extraction from Athabasca Oil Sands,” *Can. J. Chem. Eng.*, vol. 82, no. 4, pp. 628–654, May 2008.
- [15] Petroleum Technology Alliance Canada (PTAC), “Needs Assessment for Partial and Field

- Upgrading,” 2015.
- [16] T. R. B. and N. R. Council, *TRB Special Report 311: Effects of Diluted Bitumen on Crude Oil Transmission Pipelines*. Washington, D.C.: National Academies Press, 2013.
- [17] M. R. Gray, “Density and Phase Behaviour,” in *Upgrading Oilsands Bitumen and Heavy Oil*, Edmonton, CA: University of Alberta Press, 2015, pp. 1–11.
- [18] B. Keesom and J. Gieseman, “Bitumen Partial Upgrading 2018 Whitepaper AM0401A,” 2018.
- [19] “Water Usage.” [Online]. Available: <https://www.oilsandsmagazine.com/technical/environment/water-usage>. [Accessed: 01-Oct-2019].
- [20] C. J. Cleveland and C. Morris, “Oil Sands A strategic resource for Canada, North America and the global market,” 2015.
- [21] L. Botha and J. B. P. Soares, “The Influence of Tailings Composition on Flocculation,” *Can. J. Chem. Eng.*, vol. 93, no. 9, pp. 1514–1523, Sep. 2015.
- [22] A. Alamgir, D. Harbottle, J. Masliyah, and Z. Xu, “Al-PAM assisted filtration system for abatement of mature fine tailings,” *Chem. Eng. Sci.*, vol. 80, pp. 91–99, 2012.
- [23] J. Soares and F. Motta, “Using Polymer Reaction Engineering Principles to Help the Environment: The Case of the Canadian Oil Sands Tailings,” *J. Braz. Chem. Soc.*, 2018.
- [24] N. Beier, W. Wilson, A. Dunmola, and D. Segó, “Impact of flocculation-based dewatering on the shear strength of oil sands fine tailings,” *Can. Geotech. J.*, vol. 50, no. 9, pp. 1001–1007, 2013.
- [25] R. Hripko, V. Vajihinejad, F. LopesMotta, and J. B. P. Soares, “Enhanced Flocculation of Oil Sands Mature Fine Tailings Using Hydrophobically Modified Polyacrylamide Copolymers,” *Glob. Challenges*, vol. 2, no. 3, pp. 170013-n/a, 2018.
- [26] C. E. Willis, V. L. St. Louis, J. L. Kirk, K. A. St. Pierre, and C. Dodge, “Tailings ponds of the Athabasca Oil Sands Region, Alberta, Canada, are likely not significant sources of total mercury and methylmercury to nearby ground and surface waters,” *Sci. Total Environ.*, vol. 647, pp. 1604–1610, 2019.
- [27] AER, “Directive 085: Fluid Tailings Management for Oil Sands Mining Projects.” pp. 1–13, 2017.
- [28] BGC Engineering Inc., “Oil Sands Tailings Technology Review,” *Oil Sands Res. Inf. Netw.*, vol. OSRIN Repo, no. July, p. OSRIN Report No. TR-1. 136 pp., 2010.
- [29] D. R. L. Vedoy and J. B. P. Soares, “Water-soluble polymers for oil sands tailing treatment: A Review,” *Can. J. Chem. Eng.*, vol. 93, no. 5, pp. 888–904, May 2015.

- [30] M. D. MacKinnon, J. G. Matthews, W. H. Shaw, and R. G. Cuddy, “Water Quality Issues Associated With Composite Tailings (CT) Technology for Managing Oil Sands Tailings,” *Int. J. Surf. Mining, Reclam. Environ.*, vol. 15, no. 4, pp. 235–256, 2001.
- [31] J. G. Matthews, W. H. Shaw, M. D. MacKinnon, and R. G. Cuddy, “Development of Composite Tailings Technology at Syncrude,” *Int. J. Surf. Mining, Reclam. Environ.*, vol. 16, no. 1, pp. 24–39, 2002.
- [32] J. H. Masliyah, J. Czarnecki, and Z. Xu, “Chapter 8: Colloidal Science in Tailings Management,” in *Handbook on Theory and Practice of Bitumen Recovery from Athabasca Oil Sands. Volume 1: Theoretical Basis*, Kingsley Knowledge Publishing, 2011, pp. 391–448.
- [33] H. Kaminsky, T. Etsell, D. G. Ivey, and O. Omotoso, “Fundamental Particle Size of Clay Minerals in Athabasca Oil Sands Tailings,” *Clay Sci.*, vol. 12, no. Supplement2, pp. 217–222, 2006.
- [34] H. A. W. Kaminsky, T. H. Etsell, D. G. Ivey, and O. Omotoso, “Distribution of clay minerals in the process streams produced by the extraction of bitumen from Athabasca oil sands,” *Can. J. Chem. Eng.*, vol. 87, no. 1, pp. 85–93, 2009.
- [35] J. H. Masliyah, J. Czarnecki, and Z. Xu, “Chapter 4: Physical and Chemical Properties of Oil Sands,” in *Handbook on Theory and Practice of Bitumen Recovery from Athabasca Oil Sands: Theoretical Basis, vol. 1.*, no. 4, Kingsley Knowledge Publishing, 2011, pp. 173–256.
- [36] R. Hogg, “Flocculation and Dewatering of Fine-Particle Suspensions,” in *Coagulation and flocculation*, 2. ed., vol. 126, H. Stechemesser and B. Dobias, Eds. Boca Raton [u.a.]: CRC Press, Taylor & Francis Group, 2005, pp. 805–849.
- [37] S. Park and M.-K. Seo, “Intermolecular Force,” in *Interface science and composites*, vol. 18, S. Park and M.-K. Seo, Eds. Amsterdam: Academic Press, 2011, pp. 1–57.
- [38] L. L. Schramm, “Suspensions: Basic Principles,” in *Suspensions: Fundamentals and Applications in the Petroleum Industry*, L. L. Schramm, Ed. Washington, D.C.: American Chemical Society, 1996, pp. 3–44.
- [39] J. Masliyah, J. Czarnecki, and Z. Xu, “Chapter 2: Basic Scientific Background,” in *Handbook on Theory and Practice of Bitumen Recovery from Athabasca Oil Sands*, Kingsley Knowledge Publishing, 2011, pp. 51–125.
- [40] J. Long, H. Li, Z. Xu, and J. H. Masliyah, “Role of colloidal interactions in oil sand tailings treatment,” *American Institute of Chemical Engineers. AIChE Journal*, vol. 52, no. 1. American Institute of Chemical Engineers, New York, pp. 371–383, 2006.
- [41] F. L. Leite, C. C. Bueno, A. L. Da Róz, E. C. Ziemath, and O. N. Oliveira, “Theoretical Models for Surface Forces and Adhesion and Their Measurement Using Atomic Force Microscopy,” *Int. J. Mol. Sci.*, vol. 13, no. 10, pp. 12773–12856, 2012.

- [42] J. N. Israelachvili, "Electrostatic Forces between Surfaces in Liquids," in *Intermolecular and Surface Forces*, 3rd ed., US: Elsevier, 2011, pp. 291–340.
- [43] J. Bratby, "Colloids and interfaces," in *Coagulation and Flocculation in Water and Wastewater Treatment*, 3rd ed., London: IWA Publishing, 2016, pp. 11–32.
- [44] J. H. Masliyah and S. Bhattacharjee, "Electric Double Layer," in *Electrokinetic and colloid transport phenomena*, Hoboken, NJ, USA: John Wiley & Sons, Inc., 2005, pp. 105–178.
- [45] J. H. Masliyah and S. Bhattacharjee, "London-Van Der Waals Forces and the DLVO Theory," in *Electrokinetic and Colloid Transport Phenomena*, John Wiley & Sons, Inc., 2005, pp. 391–425.
- [46] S. Islam and J. Q. Shang, "Coagulation enhanced electrokinetic settling of mature fine oil sands tailings," *Int. J. Min. Sci. Technol.*, Apr. 2018.
- [47] C. Wang, D. Harbottle, Q. Liu, and Z. Xu, "Current state of fine mineral tailings treatment: A critical review on theory and practice," *Miner. Eng.*, vol. 58, pp. 113–131, Apr. 2014.
- [48] M. Scholz, "Coagulation and flocculation," in *Wetland Systems to Control Urban Runoff*, 1st ed., NL: Elsevier, 2006, pp. 43–50.
- [49] R. Hogg, "Flocculation and dewatering," *Int. J. Miner. Process.*, vol. 58, no. 1, pp. 223–236, 2000.
- [50] P. Pourrezaei *et al.*, "The Impact of Metallic Coagulants on the Removal of Organic Compounds from Oil Sands Process-Affected Water," *Environ. Sci. Technol.*, vol. 45, no. 19, pp. 8452–8459, 2011.
- [51] G. M. Moody, "Polymeric Flocculants," in *Handbook of Industrial Water Soluble Polymers*, 1st ed., P. A. Willams, Ed. John Wiley and Sons, 2007, pp. 134–173.
- [52] B. Bolto and J. Gregory, "Organic polyelectrolytes in water treatment," *Water Res.*, vol. 41, no. 11, pp. 2301–2324, 2007.
- [53] L. Botha, S. Davey, B. Nguyen, A. K. Swarnakar, E. Rivard, and J. B. P. Soares, "Flocculation of oil sands tailings by hyperbranched functionalized polyethylenes (HBfPE)," *Miner. Eng.*, vol. 108, pp. 71–82, Jul. 2017.
- [54] C. S. Lee, J. Robinson, and M. F. Chong, "A review on application of flocculants in wastewater treatment," *Process Saf. Environ. Prot.*, vol. 92, no. 6, pp. 489–508, 2014.
- [55] J. Bratby, "Treatment with polymers," in *Coagulation and Flocculation in Water and Wastewater Treatment*, 3rd ed., London: Iwa Publishing, 2016, pp. 247–291.
- [56] J. Gregory and S. Barany, "Adsorption and flocculation by polymers and polymer mixtures," *Adv. Colloid Interface Sci.*, vol. 169, no. 1, pp. 1–12, 2011.

- [57] J. Addai-Mensah and C. A. Prestidge, "Structure formation in dispersed systems," in *Coagulation and Flocculation*, 2nd ed., B. Dobias and H. Stechemesser, Eds. CRC Press, Taylor & Francis Group, 2005, pp. 135–216.
- [58] G. Sen, A. Sharon, and S. Pal, "Grafted Polysaccharides: Smart Materials of the Future, Their Synthesis and Applications," in *Biopolymers: Biomedical and Environmental Applications*, S. Kalia and L. Avérous, Eds. Hoboken, N.J.: John Wiley and Sons, 2011, pp. 99–127.
- [59] R. Singh, B. Nayak, D. Biswal, T. Tripathy, and K. Banik, "Biobased polymeric flocculants for industrial effluent treatment," *Mater. Res. Innov.*, vol. 7, no. 5, pp. 331–340, Oct. 2003.
- [60] A. K. Sarkar, N. R. Mandre, A. B. Panda, and S. Pal, "Amylopectin grafted with poly (acrylic acid): development and application of a high performance flocculant," *Carbohydr. Polym.*, vol. 95, no. 2, p. 753, 2013.
- [61] B. R. Nayak and R. P. Singh, "Synthesis and characterization of grafted hydroxypropyl guar gum by ceric ion induced initiation," *Eur. Polym. J.*, vol. 37, no. 8, pp. 1655–1666, 2001.
- [62] Y. Zhang and S. Xu, "Effects of amylose/amylopectin starch on starch-based superabsorbent polymers prepared by γ -radiation," *Starch - Stärke*, vol. 69, no. 1–2, p. 1500294, Jan. 2017.
- [63] R. P. Singh *et al.*, "Biodegradable drag reducing agents and flocculants based on polysaccharides: Materials and applications," *Polym. Eng. Sci.*, vol. 40, no. 1, pp. 46–60, Jan. 2000.
- [64] D. R. Biswal and R. P. Singh, "Characterisation of carboxymethyl cellulose and polyacrylamide graft copolymer," *Carbohydr. Polym.*, vol. 57, no. 4, pp. 379–387, 2004.
- [65] S. Pal, R. Das, and S. Ghorai, "Hydroxypropyl Methyl Cellulose Grafted with Poly(Acrylamide) Application as Novel Polymeric Material as Flocculant as well as Absorbent," in *Cellulose-Based Graft Copolymers: Structure and Chemistry*, V. K. Thakur, Ed. Boca Raton, Fla: CRC Press, Taylor & Francis Group, 2015, pp. 301–334.
- [66] N. A. Oladoja, "Headway on natural polymeric coagulants in water and wastewater treatment operations," *J. Water Process Eng.*, vol. 6, pp. 174–192, Jun. 2015.
- [67] V. H. Dao, N. R. Cameron, and K. Saito, "Synthesis, properties and performance of organic polymers employed in flocculation applications," *Polym. Chem*, vol. 7, no. 1, pp. 11–25, 2015.
- [68] V. D. Athawale and S. C. Rathi, "Graft polymerization: starch as a model substrate," *J. Macromol. Sci. - Polym. Rev.*, vol. 39, no. 3, pp. 445–480, 1999.
- [69] M. Tizzotti, A. Charlot, E. Fleury, M. Stenzel, and J. Bernard, "Modification of Polysaccharides Through Controlled/Living Radical Polymerization Grafting-Towards the Generation of High Performance Hybrids," *Macromol. Rapid Commun.*, vol. 31, no. 20, pp.

1751–1772, 2010.

- [70] S. Kalia, M. W. Sabaa, and S. Kango, “Polymer Grafting: A Versatile Means to Modify the Polysaccharides,” in *Polysaccharide Based Graft Copolymers*, S. Kalia and M. W. Sabaa, Eds. Berlin, Heidelberg: Springer Berlin Heidelberg, 2013, pp. 1–14.
- [71] S. K. Rath and R. P. Singh, “Flocculation characteristics of grafted and ungrafted starch, amylose, and amylopectin,” *J. Appl. Polym. Sci.*, vol. 66, no. 9, pp. 1721–1729, 1997.
- [72] R. P. Singh, “Advanced Turbulent Drag Reducing and Flocculating Materials Based on Polysaccharides,” in *Polymers and Other Advanced Materials*, P. N. Prasad, J. E. Mark, and T. J. Fai, Eds. Boston, MA: Springer, Boston, MA, 1995, pp. 227–249.
- [73] S. Pal, S. A. Ali, G. Sen, and R. P. Singh, “Modification and Applications of Guar Gum in the Field of Green Chemistry,” in *Green Chemistry for Environmental Remediation*, Hoboken, NJ, USA: John Wiley & Sons, Inc., 2012, pp. 729–761.
- [74] S. Mishra, G. Sen, K. Dey, and G. Rani, “Synthesis and Applications of Grafted Carboxymethyl Cellulose: A Review,” in *Cellulose-Based Graft Copolymers*, V. K. Thakur, Ed. Boca Raton: CRC Press, 2015, pp. 475–496.
- [75] W. Brostow, S. Pal, and R. P. Singh, “A model of flocculation,” *Mater. Lett.*, vol. 61, no. 22, pp. 4381–4384, 2007.
- [76] A. N. Jyothi and A. J. F. Carvalho, “Starch-g-Copolymers: Synthesis, Properties and Applications,” in *Polysaccharide Based Graft Copolymers*, S. Kalia and M. W. Sabaa, Eds. Berlin, Heidelberg: Springer Berlin Heidelberg, 2013, pp. 59–109.
- [77] M. Worzakowska and M. Grochowicz, “Effect of some parameters on the synthesis and the physico-chemical properties of new amphiphilic starch-g-copolymers,” *Carbohydr. Polym.*, vol. 130, pp. 344–352, 2015.
- [78] O. Olatunji, “Classification of Natural Polymers,” in *Natural Polymers: Industry Techniques and Applications*, 1st ed. 20., O. Olatunji, Ed. Cham: Springer, 2015, pp. 1–17.
- [79] D. Kalita and A. N. Netravali, “Thermoset Resin Based Fiber Reinforced Biocomposites,” in *Textile Finishing: Recent Developments and Future Trends*, K. L. Mittal and T. Bahners, Eds. Hoboken, NJ, USA: Wiley Blackwell, 2017, pp. 425–484.
- [80] S. K. Rath and R. P. Singh, “Grafted amylopectin: applications in flocculation,” *Colloids Surfaces A Physicochem. Eng. Asp.*, vol. 139, no. 2, pp. 129–135, 1998.
- [81] N. Karmakar, B. Sastry, and R. Singh, “Flocculation of chromite ore fines suspension using polysaccharide based graft copolymers,” *Bull. Mater. Sci.*, vol. 25, no. 6, pp. 477–478, Nov. 2002.
- [82] R. P. Singh, S. Pal, V. K. Rana, and S. Ghorai, “Amphoteric amylopectin: A novel polymeric flocculant,” *Carbohydr. Polym.*, vol. 91, no. 1, pp. 294–299, 2013.

- [83] H. Kolya and T. Tripathy, "Grafted polysaccharides based on acrylamide and N,N-dimethylacrylamide: Preparation and investigation of their flocculation performances," *J. Appl. Polym. Sci.*, vol. 127, no. 4, pp. 2786–2795, 2013.
- [84] H. Kolya and T. Tripathy, "Biodegradable flocculants based on polyacrylamide and poly(N,N-dimethylacrylamide) grafted amylopectin," *Int. J. Biol. Macromol.*, vol. 70, pp. 26–36, Sep. 2014.
- [85] A. K. Sarkar, A. Pal, S. Ghorai, N. R. Mandre, and S. Pal, "Efficient removal of malachite green dye using biodegradable graft copolymer derived from amylopectin and poly(acrylic acid)," *Carbohydr. Polym.*, vol. 111, pp. 108–115, 2014.
- [86] S. Pal and A. Pal, "Synthesis and characterizing a novel polymeric flocculant based on amylopectin-graft-polyacrylamide-graft-polyacrylic acid [(AP-g-PAM)-g-PAA]," *Polym. Bull.*, vol. 69, no. 5, pp. 545–560, Sep. 2012.
- [87] P. Adhikary and S. Krishnamoorthi, "Synthesis, characterization, and application of amylopectin-graft-poly(AM-co-AMPS)," *J. Appl. Polym. Sci.*, vol. 126, no. S1, pp. E31–E318, 2012.
- [88] K. Kumar, P. Adhikary, N. C. Karmakar, S. Gupta, R. P. Singh, and S. Krishnamoorthi, "Synthesis, characterization and application of novel cationic and amphoteric flocculants based on amylopectin," *Carbohydr. Polym.*, vol. 127, pp. 275–281, 2015.
- [89] D. Sasmal, R. P. Singh, and T. Tripathy, "Synthesis and flocculation characteristics of a novel biodegradable flocculating agent amylopectin-g-poly(acrylamide-co-N-methylacrylamide)," *Colloids Surfaces A Physicochem. Eng. Asp.*, vol. 482, pp. 575–584, 2015.
- [90] D. Sasmal, H. Kolya, and T. Tripathy, "Amylopectin-g-poly(methylacrylate-co-sodium acrylate): An efficient Cd(II) binder," *Int. J. Biol. Macromol.*, vol. 91, pp. 934–945, Oct. 2016.
- [91] F. L. Motta, S. R. Stoyanov, and J. B. P. Soares, "Development and application of an amylopectin-graft-poly(methyl acrylate) solidifier for rapid and efficient containment and recovery of heavy oil spills in aqueous environments," *Chemosphere*, vol. 236, p. 124352, Dec. 2019.
- [92] B. Bazoubandi, "Synthesis and Characterization of Amylopectin-grafted Polyacrylamide (AP-g-PAM) Flocculants for Dewatering of Oil Sands Mature Fine Tailings (MFT)," University of Alberta Libraries, 2018.
- [93] L. Pennetta de Oliveira, "Chitosan-Based Flocculants for Mature Fine Tailings Treatment," University of Alberta Libraries, 2018.
- [94] L. Pennetta de Oliveira, S. P. Gumfekar, F. Lopes Motta, and J. B. P. Soares, "Dewatering of Oil Sands Tailings with Novel Chitosan-Based Flocculants," *Energy & Fuels*, vol. 32, no. 4, pp. 5271–5278, 2018.

- [95] S. Wang *et al.*, “Synthesis and characterization of starch-poly(methyl acrylate) graft copolymers using horseradish peroxidase,” *Carbohydr. Polym.*, vol. 136, pp. 1010–1016, 2016.
- [96] L. Wang and Y. Xu, “Preparation and characterization of graft copolymerization of ethyl acrylate onto hydroxypropyl methylcellulose in aqueous medium,” *Cellulose*, vol. 13, no. 2, pp. 191–200, Apr. 2006.
- [97] L. Wang, W. Dong, and Y. Xu, “Synthesis and characterization of hydroxypropyl methylcellulose and ethyl acrylate graft copolymers,” *Carbohydr. Polym.*, vol. 68, no. 4, pp. 626–636, 2007.
- [98] S. Das, D. Sasmal, S. Pal, H. Kolya, A. Pandey, and T. Tripathy, “Starch based biodegradable graft copolymer for the preparation of silver nanoparticles,” *Int. J. Biol. Macromol.*, vol. 81, pp. 83–90, Nov. 2015.
- [99] B. Zhang and Y. Zhou, “Synthesis and characterization of graft copolymers of ethyl acrylate/acrylamide mixtures onto starch,” *Polym. Compos.*, vol. 29, no. 5, pp. 506–510, May 2008.
- [100] S. Mishra, S. Sinha, K. P. Dey, and G. Sen, “Synthesis, characterization and applications of polymethylmethacrylate grafted psyllium as flocculant,” *Carbohydr. Polym.*, vol. 99, pp. 462–468, 2014.
- [101] G. E. P. Box and K. B. Wilson, “On the Experimental Attainment of Optimum Conditions,” *J. R. Stat. Soc. Ser. B*, vol. 13, no. 1, pp. 1–38, Jan. 1951.
- [102] M. A. Bezerra, R. E. Santelli, E. P. Oliveira, L. S. Villar, and L. A. Escaleira, “Response surface methodology (RSM) as a tool for optimization in analytical chemistry,” *Talanta*, vol. 76, no. 5, pp. 965–977, Sep. 2008.
- [103] D. C. Montgomery, “Response Surface Methods and Designs,” in *Design and Analysis of Experiments*, 8th ed., John Wiley & Sons, Inc., 2013, pp. 478–553.
- [104] F. L. Motta, R. Gaikwad, L. Botha, and J. B. P. Soares, “Quantifying the effect of polyacrylamide dosage, Na⁺ and Ca²⁺ concentrations, and clay particle size on the flocculation of mature fine tailings with robust statistical methods,” *Chemosphere*, vol. 208, pp. 263–272, Oct. 2018.
- [105] R. J. Parod, “Methyl Acrylate,” in *Encyclopedia of Toxicology: Third Edition*, Elsevier, 2014, pp. 264–266.
- [106] N. C. for B. Information, “3,6-Anhydro-D-glucose,” *PubChem Database*. [Online]. Available: <https://pubchem.ncbi.nlm.nih.gov/compound/16069993>. [Accessed: 08-Oct-2019].
- [107] M. A. Mohamed, J. Jaafar, A. F. Ismail, M. H. D. Othman, and M. A. Rahman, “Fourier Transform Infrared (FTIR) Spectroscopy,” in *Membrane Characterization*, N. Hilal, A. F.

- Ismail, T. Matsuura, and D. Oatley-Radcliffe, Eds. Elsevier, 2017, pp. 3–29.
- [108] L. G. Reis *et al.*, “Using acrylamide/propylene oxide copolymers to dewater and densify mature fine tailings,” *Miner. Eng.*, vol. 95, pp. 29–39, Sep. 2016.
- [109] O. Sawalha and M. Scholz, “Assessment of Capillary Suction Time (CST) Test Methodologies,” *Environ. Technol.*, vol. 28, no. 12, pp. 1377–1386, 2007.
- [110] L. Smoczyński *et al.*, “Study of Sludge Particles Formed during Coagulation of Synthetic and Municipal Wastewater for Increasing the Sludge Dewatering Efficiency,” *Water*, vol. 11, no. 1, p. 101, 2019.
- [111] J. Meimoun *et al.*, “Modification of starch by graft copolymerization,” *Starch - Stärke*, vol. 70, no. 1–2, p. 1600351, Jan. 2018.
- [112] P. K. Pandey, J. Banerjee, K. Taunk, and K. Behari, “Graft copolymerization of acrylic acid onto xanthum gum using a potassium monopersulfate/Fe²⁺ redox pair,” *J. Appl. Polym. Sci.*, vol. 89, no. 5, pp. 1341–1346, 2003.
- [113] A. A. Berlin and V. N. Kislenko, “Kinetics and mechanism of radical graft polymerization of monomers onto polysaccharides,” *Prog. Polym. Sci.*, vol. 17, no. 5, pp. 765–825, 1992.
- [114] L. Wang and Y. Xu, “Effect of dimethylaminoethyl methacrylate on the graft copolymerization of ethyl acrylate onto hydroxypropyl methylcellulose in aqueous medium,” *Cellulose*, vol. 13, no. 6, pp. 713–724, Dec. 2006.
- [115] A. A. Ragheb, I. Abdel-Thalouth, and S. Tawfik, “Gelatinization of Starch in Aqueous Alkaline Solutions,” *Starch - Stärke*, vol. 47, no. 9, pp. 338–345, 1995.
- [116] T. Tripathy and R. P. Singh, “High performance flocculating agent based on partially hydrolysed sodium alginate–g–polyacrylamide,” *Eur. Polym. J.*, vol. 36, no. 7, pp. 1471–1476, 2000.
- [117] L. N. Lai, A. A. Karim, M. H. Norziah, and C. C. Seow, “Effects of Na₂CO₃ and NaOH on Pasting Properties of Selected Native Cereal Starches,” *J. Food Sci.*, vol. 69, no. 4, pp. FCT24–FCT256, May 2004.
- [118] M. I. Khalil, S. Farag, and S. A. El Fattach, “Poly(acrylamide)-starch graft copolymer,” *J. Appl. Polym. Sci.*, vol. 57, no. 3, pp. 335–342, 1995.
- [119] P. Lanthong, R. Nuisin, and S. Kiatkamjornwong, “Graft copolymerization, characterization, and degradation of cassava starch- g-acrylamide/itaconic acid superabsorbents,” *Carbohydr. Polym.*, vol. 66, no. 2, pp. 229–245, 2006.
- [120] Z. Zhang, P. Chen, S. Chen, X. Du, Z. Xue, and B. Yang, “Effects of amylose content on property and microstructure of starch-graft-sodium acrylate copolymers,” *Carbohydr. Polym.*, vol. 102, pp. 453–459, 2014.

- [121] L. Xia, G. Wenyuan, J. Qianqian, H. Luqi, and L. Changxiao, "Study on the morphology, crystalline structure, and thermal properties of *Fritillaria ussuriensis* Maxim. starch acetates with different degrees of substitution," *Starch - Stärke*, vol. 63, no. 1, pp. 24–31, Jan. 2011.
- [122] H. Chi *et al.*, "Effect of acetylation on the properties of corn starch," *Food Chem.*, vol. 106, no. 3, pp. 923–928, 2008.
- [123] Q.-J. Peng and A. S. Perlin, "Observations on N.M.R. spectra of starches in dimethyl sulfoxide, iodine-complexing, and solvation in water-di-methyl sulfoxide," *Carbohydr. Res.*, vol. 160, pp. 57–72, 1987.
- [124] J. Liu, X. Wang, R. Bai, N. Zhang, J. Kan, and C. Jin, "Synthesis, characterization, and antioxidant activity of caffeic-acid-grafted corn starch," *Starch - Stärke*, vol. 70, no. 1–2, p. 1700141, Jan. 2018.
- [125] M. J. Tizzotti, M. C. Sweedman, D. Tang, C. Schaefer, and R. G. Gilbert, "New ¹H NMR procedure for the characterization of native and modified food-grade starches," *J. Agric. Food Chem.*, vol. 59, no. 13, pp. 6913–6919, 2011.
- [126] Q. Zhang, K. Xu, and P. Wang, "Study on structure and molecular dynamics of starch/poly(sodium acrylate)-grafted superabsorbent by ¹³C solid state NMR," *Fibers Polym.*, vol. 9, no. 3, pp. 271–275, Jun. 2008.
- [127] W. Zou *et al.*, "Effects of amylose/amylopectin ratio on starch-based superabsorbent polymers," *Carbohydr. Polym.*, vol. 87, no. 2, pp. 1583–1588, 2012.
- [128] N. Çankaya, "Synthesis of graft copolymers onto starch and its semiconducting properties," *Results Phys.*, vol. 6, pp. 538–542, 2016.
- [129] M. Elomaa *et al.*, "Determination of the degree of substitution of acetylated starch by hydrolysis, ¹H NMR and TGA/IR," *Carbohydr. Polym.*, vol. 57, no. 3, pp. 261–267, 2004.
- [130] V. Vajihinejad, R. Guillermo, and J. B. P. Soares, "Dewatering Oil Sands Mature Fine Tailings (MFTs) with Poly(acrylamide-co-diallyldimethylammonium chloride): Effect of Average Molecular Weight and Copolymer Composition," *Ind. Eng. Chem. Res.*, vol. 56, no. 5, pp. 1256–1266, 2017.
- [131] V. Vajihinejad, S. P. Gumfekar, B. Bazoubandi, Z. Rostami Najafabadi, and J. B. P. Soares, "Water Soluble Polymer Flocculants: Synthesis, Characterization, and Performance Assessment," *Macromol. Mater. Eng.*, vol. 304, no. 2, p. 1800526, Feb. 2019.

Appendix A. Purification Study

An analysis of the Soxhlet filtrate over time for AP-g-PMA (GP9) was first performed to determine the time required to fully extract the homopolymer. The filtrate was replaced on a 24-hour basis and analyzed with the FTIR (Figure A1), to determine the point where no more PMA could be washed out.

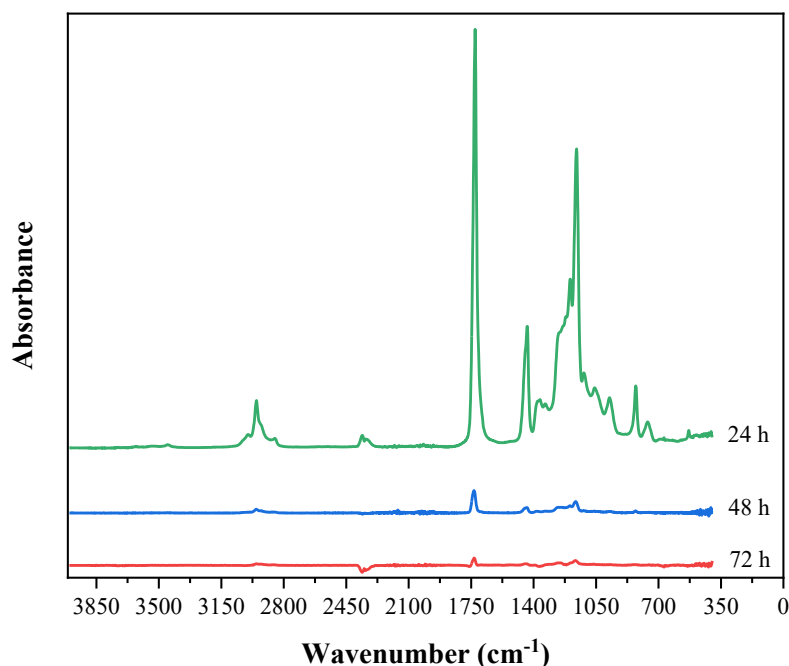


Figure A1: FTIR spectra of poly(methyl acrylate) (PMA) in the Soxhlet extraction filtrate at various time intervals.

In Figure A2, excess methanol was used to precipitate the PMA in the filtrate. The graft copolymer was determined to be pure when the solution was clear after adding methanol. The concentration of PMA in the acetone filtrate was then measured and used to determine the percentage of homopolymer washed away after each day. Table A1 shows the percentage of homopolymer washed away for each time period.

After 72 hours, the PMA absorbance peaks essentially disappeared, and the methanol solution appeared completely clear, suggesting that no more homopolymer was present. The CCD polymers produced were thus washed in the Soxhlet apparatus for 72 hours to ensure purity.



Figure A2: Precipitated filtrate poly(methyl acrylate) (PMA) at various time intervals (left 24 hours, centre 48 hours, right 72 hours).

Table A1: Percentage of total poly(methyl acrylate) (PMA) homopolymer washed away over time.

Filtrate	24 h	48 h	72 h
Homopolymer (%)	92	7	1

To examine the effectiveness of extraction with acetone, a controlled experiment was carried out with a blend of AP and PMA (1:1 by weight) following the same procedure as the graft copolymers and compared with GP11. The polymer was then dried and analyzed under the FTIR.

It was observed that the Soxhlet extraction did not work effectively for the AP-PMA blend as the thimble pores clogged within the first 24 hours. A physical mixing purification was then performed on the sample remaining in the Soxhlet thimble. The polymer was stirred at 600 rpm in excess acetone for 24 hours and the thick solution was then centrifuged at 4200 rpm for 30 minutes to separate the insoluble portion from the acetone soluble PMA. The insoluble portion was then dried and analyzed, and the same procedure was followed for GP11. The comparison of the FTIR spectra can be seen in Figure A3.

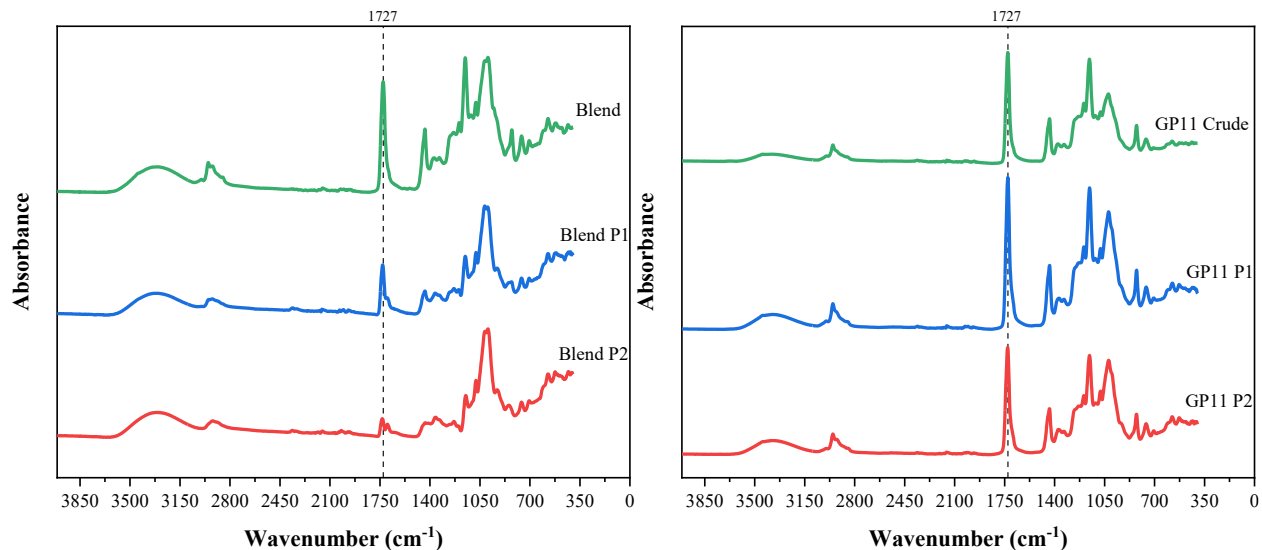


Figure A3: Amylopectin and poly(methyl acrylate) (AP-PMA) blend (left), and amylopectin-g-poly(methyl acrylate) (AP-g-PMA) (sample GP11) (right), before and after Soxhlet purification (P1) followed by mixing purification (P2).

The study provided strong evidence that grafting did occur as the AP-PMA blend clogged the pores of the Soxhlet thimble within the first 24 hours, unlike GP11, possibly due to the AP-PMA blend and the graft copolymer having different microstructures. As well, the PMA absorbance peaks in the graft copolymer hardly decreased with each subsequent wash, unlike the blend where they essentially disappeared.

Appendix B. CCD ANOVA and Residual Plots

Table B1: ANOVA for the ISR model.

Factor	SS ^{a)}	df ^{b)}	MS ^{c)}	F ^{d)}	p ^{e)}	Significant
$X_1 (L)$	8.205	1	8.205	8.418	0.008	✓
$X_1 (Q)$	2.052	1	2.052	2.105	0.160	✗
$X_2 (L)$	3.683	1	3.683	3.779	0.064	✓
$X_2 (Q)$	6.660	1	6.660	6.832	0.015	✓
$X_3 (L)$	209.667	1	209.667	215.089	0.000	✓
$X_3 (Q)$	0.441	1	0.441	0.452	0.508	✗
X_1X_2	2.988	1	2.988	3.065	0.093	✓
X_1X_3	4.323	1	4.323	4.435	0.046	✓
X_2X_3	5.306	1	5.306	5.443	0.028	✓
Error	23.395	24	0.975			
Total SS	264.795	33				

a) Sum of squares, b) Degrees of freedom, c) Mean square, d) F value, e) p-value

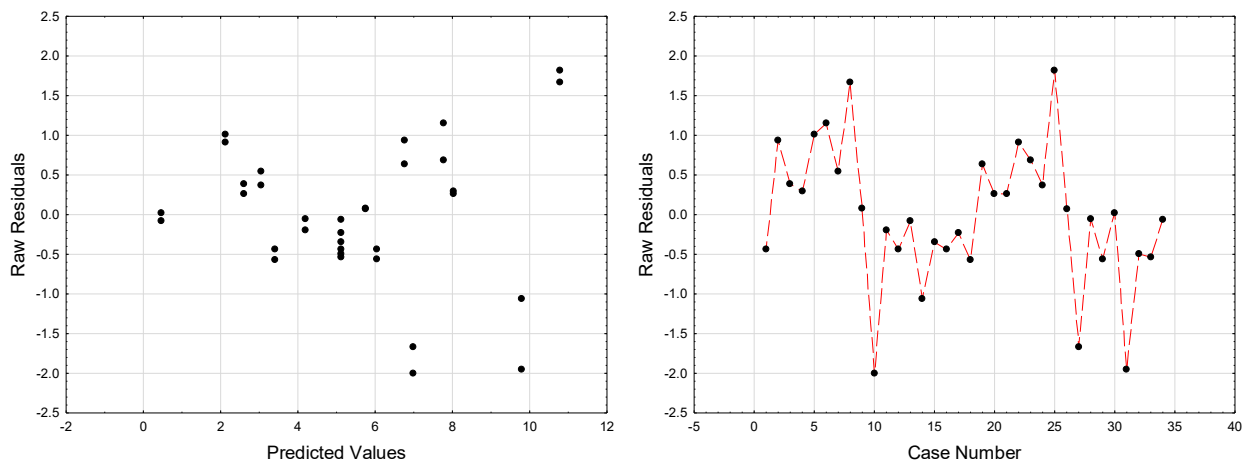


Figure B1: Residuals versus predicted values for the ISR model (left), Run sequence plot for the ISR model (right).

Table B2: ANOVA for the initial CST model.

Factor	SS ^{a)}	df ^{b)}	MS ^{c)}	F ^{d)}	p ^{e)}	Significant
$X_1 (L)$	1.520E-4	1	1.520E-4	8.494	0.008	✓
$X_1 (Q)$	2.400E-5	1	2.400E-5	1.366	0.254	✗
$X_2 (L)$	3.900E-4	1	3.900E-4	21.877	0.000	✓
$X_2 (Q)$	1.290E-4	1	1.290E-4	7.211	0.013	✓
$X_3 (L)$	1.178E-2	1	1.178E-2	660.673	0.000	✓
$X_3 (Q)$	7.300E-5	1	7.300E-5	4.104	0.054	✓
X_1X_2	5.000E-6	1	5.000E-6	0.307	0.585	✗
X_1X_3	1.690E-4	1	1.690E-4	9.462	0.005	✓
X_2X_3	1.720E-4	1	1.720E-4	9.627	0.005	✓
Error	4.280E-4	24	1.800E-5			
Total SS	1.326E-2	33				

a) Sum of squares, b) Degrees of freedom, c) Mean square, d) F value, e) p-value

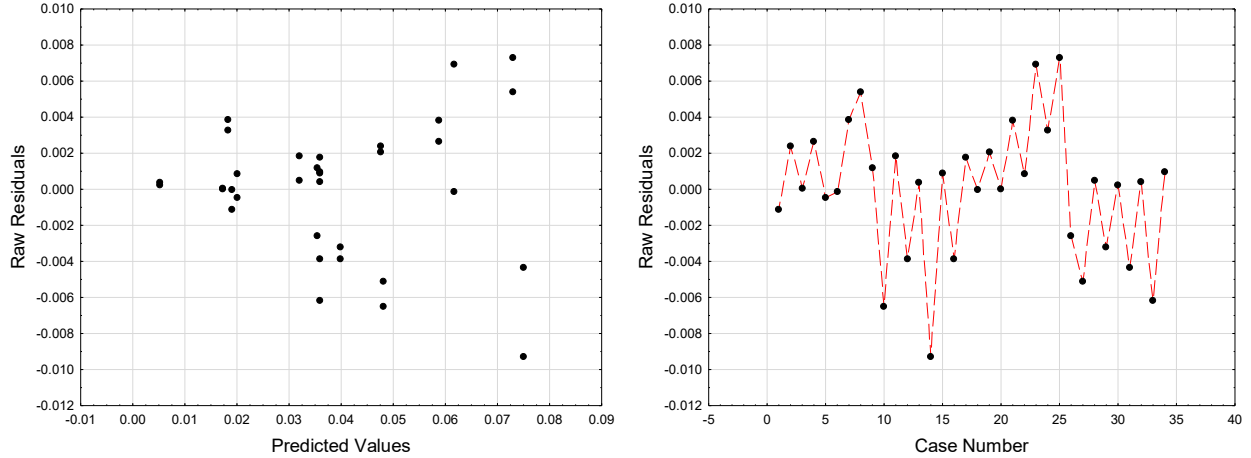


Figure B2: Residuals versus predicted values for the CST 0h model (left), Run sequence plot for the CST 0h model (right).

Table B3: ANOVA for the sediment CST model.

Factor	SS ^{a)}	df ^{b)}	MS ^{c)}	F ^{d)}	p ^{e)}	Significant
$X_1 (L)$	495.310	1	495.310	5.585	0.027	✓
$X_1 (Q)$	13.150	1	13.150	0.148	0.704	✗
$X_2 (L)$	1117.580	1	1117.580	12.601	0.002	✓
$X_2 (Q)$	1406.450	1	1406.450	15.859	0.001	✓
$X_3 (L)$	82539.890	1	82539.890	930.686	0.000	✓
$X_3 (Q)$	2775.310	1	2775.310	31.293	0.000	✓
X_1X_2	110.950	1	110.950	1.251	0.274	✗
X_1X_3	0.560	1	0.560	0.006	0.937	✗
X_2X_3	292.410	1	292.410	3.297	0.082	✓
Error	2128.490	24	88.690			
Total SS	92599.130	33				

a) Sum of squares, b) Degrees of freedom, c) Mean square, d) F value, e) p-value

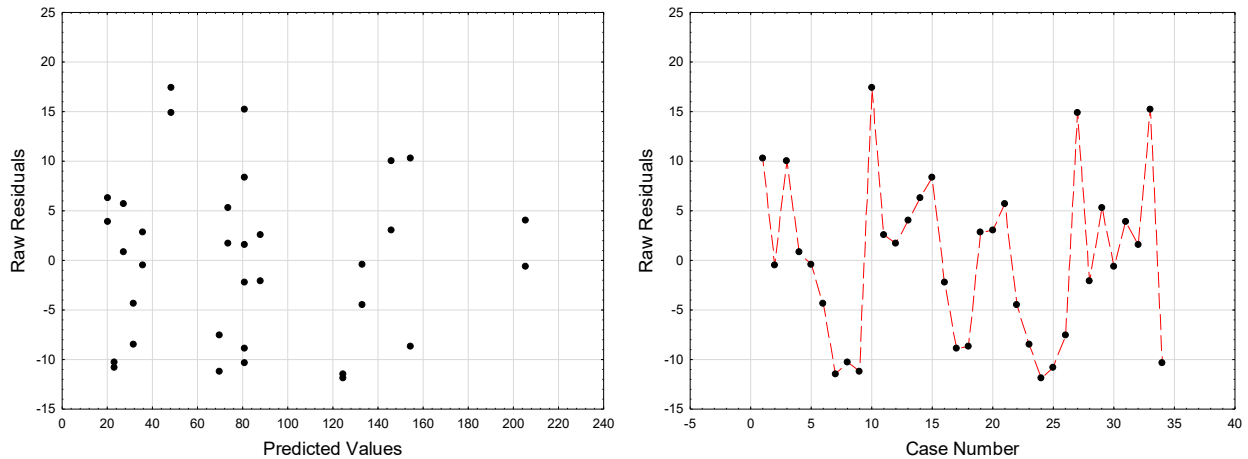


Figure B3: Residuals versus predicted values for the CST 24h model (left), Run sequence plot for the CST 24h model (right).

Table B4: ANOVA for the turbidity model.

Factor	SS ^{a)}	df ^{b)}	MS ^{c)}	F ^{d)}	p ^{e)}	Significant
$X_1 (L)$	6262.200	1	6262.200	15.126	0.001	✓
$X_1 (Q)$	1338.400	1	1338.400	3.233	0.085	✓
$X_2 (L)$	49.000	1	49.000	0.118	0.734	✗
$X_2 (Q)$	185.700	1	185.700	0.449	0.509	✗
$X_3 (L)$	160715.600	1	160715.600	388.204	0.000	✓
$X_3 (Q)$	61.000	1	61.000	0.147	0.704	✗
X_1X_2	2200.400	1	2200.400	5.315	0.030	✓
X_1X_3	2012.300	1	2012.300	4.861	0.037	✓
X_2X_3	500.600	1	500.600	1.209	0.282	✗
Error	9936.000	24	414.000			
Total SS	183038.600	33				

a) Sum of squares, b) Degrees of freedom, c) Mean square, d) F value, e) p-value

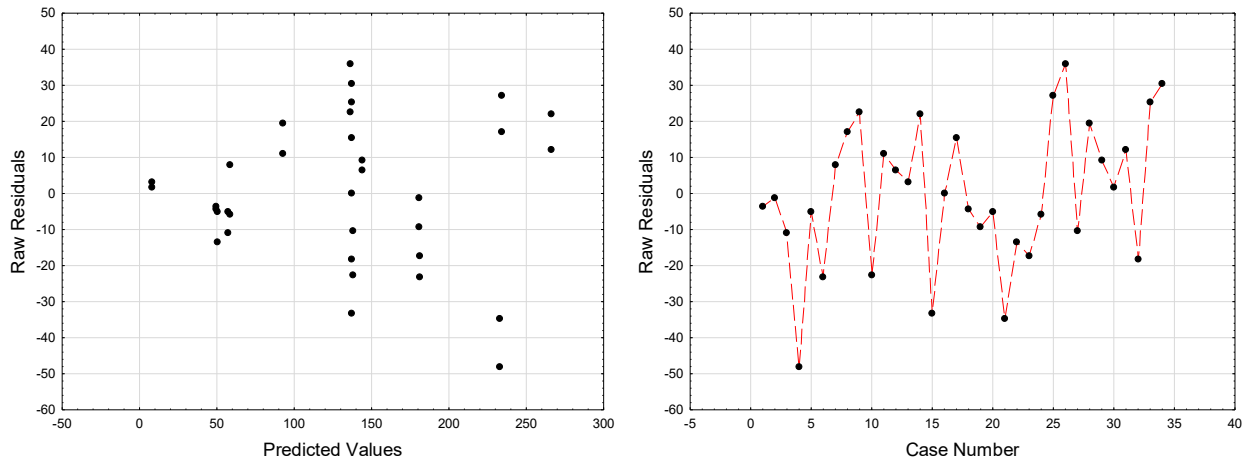


Figure B4: Residuals versus predicted values for the turbidity model (left), Run sequence plot for the turbidity model (right).

Table B5: ANOVA for the solids content model.

Factor	SS^{a)}	df^{b)}	MS^{c)}	F^{d)}	p^{e)}	Significant
<i>X₁ (L)</i>	0.251	1	0.251	0.126	0.726	✗
<i>X₁ (Q)</i>	0.885	1	0.885	0.445	0.511	✗
<i>X₂ (L)</i>	0.038	1	0.038	0.019	0.891	✗
<i>X₂ (Q)</i>	0.361	1	0.361	0.182	0.674	✗
<i>X₃ (L)</i>	7.684	1	7.684	3.861	0.061	✓
<i>X₃ (Q)</i>	22.551	1	22.551	11.331	0.003	✓
<i>X₁X₂</i>	0.937	1	0.937	0.471	0.499	✗
<i>X₁X₃</i>	0.428	1	0.428	0.215	0.647	✗
<i>X₂X₃</i>	0.899	1	0.899	0.452	0.508	✗
Error	47.765	24	1.990			
Total SS	89.045	33				

a) Sum of squares, b) Degrees of freedom, c) Mean square, d) F value, e) p-value

Appendix C. Comparison Flocculation Results

Table C1: Flocculation results for the comparison tests.

Polymer	Dosage (ppm)	ISR (cm/h)	CST 0h (s)	Error*	CST 24h (s)	Error*	Turbidity (NTU)	Error*	Solids content (wt.%)	Error*
A-PAM	500	0.3	198.3	4.0	258.2	3.4	5.4	0.1	14.3	0.1
	1000	0.7	171.4	1.8	251.3	3.4	4.8	0.1	16.0	0.3
	2000	1082.0	53.5	1.9	33.8	3.8	75.2	0.1	19.7	1.6
	4000	609.6	145.5	4.1	106.3	2.2	83.6	0.6	24.0	1.2
	6000	344.4	231.0	2.7	172.3	3.5	113.7	2.3	25.9	0.9
	9000	153.1	444.0	1.4	286.6	4.9	196.0	3.1	24.6	1.0
AP	500	0.1	205.5	4.5	210.0	2.4	16.6	0.5	12.6	0.1
	1000	0.4	206.1	9.4	211.2	6.6	15.8	0.3	12.4	0.0
	2000	0.9	199.4	1.2	243.3	7.6	15.1	0.4	13.6	0.1
	4000	1.5	186.1	6.8	275.8	8.2	13.7	0.2	17.0	0.4
	6000	2.1	182.8	1.2	327.5	11.0	6.1	0.1	18.3	0.1
	9000	3.0	182.9	13.5	381.0	3.3	5.3	0.2	22.2	0.3
H-PMA	500	5.5	56.2	1.6	138.5	3.8	15.5	0.1	19.1	0.0
	1000	13.7	29.2	0.2	92.2	5.3	41.8	1.0	19.0	0.0
	2000	27.4	20.0	0.5	42.7	2.1	141.0	0.0	18.8	0.1
	4000	60.5	124.7	3.1	19.8	1.1	1588.3	3.8	16.8	0.2
	6000	41.2	350.0	8.2	108.9	2.1	> 9999	0.0	19.9	0.1
	9000	11.3	670.7	37.2	275.7	18.7	> 9999	0.0	18.1	0.1
Blend	500	3.9	78.5	0.4	190.0	6.3	11.4	0.1	20.2	0.3
	1000	6.6	39.7	0.3	118.7	0.3	19.3	0.1	19.9	0.1
	2000	24.8	22.2	0.3	66.9	1.7	61.3	0.3	19.3	0.0
	4000	108.0	18.9	0.4	21.8	0.4	223.0	0.6	18.6	0.2
	6000	103.7	73	6.0	13.4	1.1	1122.0	1.5	19.5	0.1
	9000	94.5	220.3	6.8	42.1	2.6	1814.3	2.3	17.6	0.7
HGP11	500	0.6	178.1	1.2	227.6	10.0	11.4	0.0	14.4	0.2
	1000	1.6	127.1	2.4	222.3	6.0	16.8	0.3	17.5	0.1
	2000	8.5	54.0	0.6	155.6	6.2	37.9	0.6	19.6	0.1
	4000	23.9	26.5	0.9	71.9	3.7	152.7	1.8	19.9	0.5
	6000	60.7	15.4	1.0	31.7	0.6	165.0	0.0	18.8	0.1
	9000	97.9	10.2	0.3	10.5	0.3	260.0	3.6	17.6	0.2
Crude HGP11	500	3.0	94.4	1.7	250.3	7.6	12.5	0.3	19.3	0.3
	1000	6.8	56.2	2.1	183.3	3.0	16.0	0.1	19.4	0.2
	2000	13.0	30.5	0.5	99.2	1.0	61.4	0.4	19.5	0.2
	4000	47.4	29.6	1.0	52.2	1.2	192.3	0.7	17.9	0.1
	6000	8.1	97.7	5.5	53.4	1.4	729.0	1.7	18.0	0.1
	9000	12.4	166.6	2.6	68.0	0.7	2132.7	6.4	18.8	0.1
Calcium Blank	1500 (Ca ²⁺)	0.1	226.8	6.5	259.1	8.1	33.5	1.6	12.5	0.0

*Standard error of the mean



Figure C1: A-PAM flocculation series (dosage increases from left to right).



Figure C2: AP flocculation series (dosage increases from left to right).



Figure C3: H-PMA flocculation series (dosage increases from left to right).

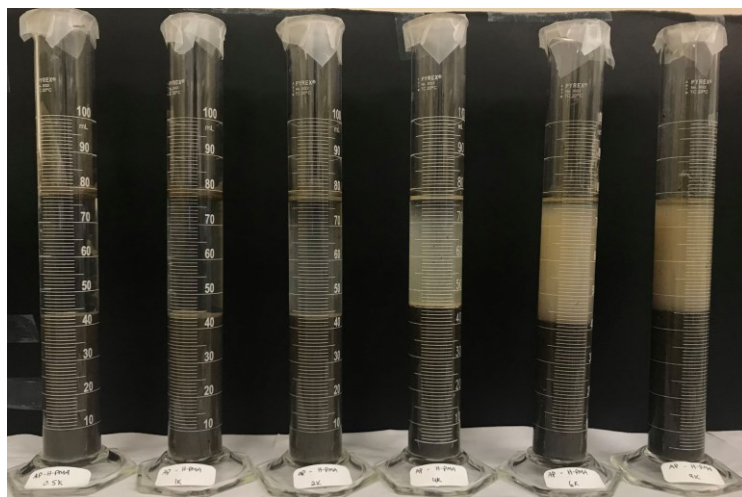


Figure C4: Blend flocculation series (dosage increases from left to right).



Figure C5: HGP11 flocculation series (dosage increases from left to right).

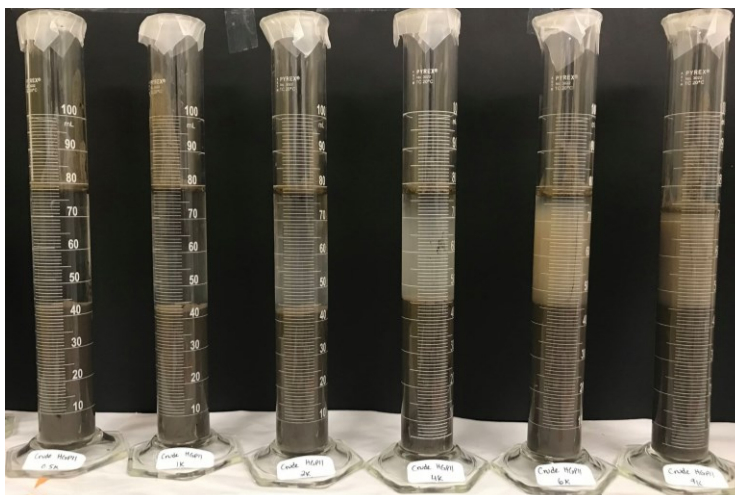


Figure C6: Crude HGP11 flocculation series (dosage increases from left to right).



Figure C7: Calcium blank.